Laboratory Spectroscopy of Fluorinated Molecules for Atmospheric Physics

by

Paul Joseph Godin

A thesis submitted in conformity with the requirements
for the degree of Doctor of Philosophy
Graduate Department of Physics
University of Toronto

Abstract

Laboratory Spectroscopy of Fluorinated Molecules for Atmospheric Physics

Paul Joseph Godin
Doctor of Philosophy
Graduate Department of Physics
University of Toronto
2017

Temperature-dependent absorption cross-sections are presented for five fluorinated molecules considered to be greenhouse gases due to being radiatively active in the mid-infrared. The molecules studied are perfluorotributylamine (PFTBA), 2,2,3,3,3-pentafluoropropanol (PFPO), 1,1,1,3,3,3-hexafluoro-2-propanol (HFIP), perfluorodecalin (PFDC), and 2H,3H-perfluoropentane (HFC-43-10mee). HFIP is a fluorinated liquid commonly used as a specialty solvent for some polar polymers and in organic synthesis. PFTBA, PFPO, and HFC-43-10mee are commonly used in electronic and industrial applications. PFDC is capable of dissolving large quantities of gases, making it useful for a variety of medical applications.

Experimental absorption cross-sections were derived from Fourier transform infrared spectra recorded from 530 to 3400 cm^{-1} with a resolution of 0.1 cm^{-1} over a temperature range of 298 to 360 K. These results were compared to theoretical density functional theory (DFT) calculations and previously published experimental measurements made at room temperature.

Theoretical DFT calculations were performed using the B3LYP method and a minimum basis set of 6-311+G(d,p). The calculations have determined the optimized geometrical configuration, infrared intensities, and wavenumbers of the harmonic frequencies for different ground-state configurations due to the presence of internal rotors. As the population of each configuration changes with temperature, changes in the experimental spectra were used to make accurate band assignments. From these band assignments, the DFT spectra were calibrated to match the experimental spectra, increasing the accuracy

of the DFT prediction outside of the experimental range.

Using the adjusted DFT-calculated spectra, the wavenumber range was extended beyond the experimental range to calculate radiative efficiencies and global warming potentials. When using only the experimental range, the new values agreed with previously published values. However, when the range was extended using the DFT spectra, the radiative efficiency and global warming potential were increased, suggesting that the current values are underestimating the climate impacts of these species.

Additionally, work done on building a multipass White cell is presented. This new system can be used in the future to resolve weak lines to extract line parameters needed for atmospheric trace gas retrievals.

None of this could have been done without the support of my family and friends who helped get me where I am today. For that, I thank them all.

Acknowledgements

Thanks to Dr. Kimberly Strong for letting me be a part of her research group and for providing guidance, Dr. Karine Le Bris for providing codes for analysis and access to Compute Canada, Dr. Stephanie Conway for teaching me how to use the lab equipment, Dr. Li-Hong Xu for fruitful discussions about DFT, Jerry Zhai for assistance with assembling the White cell, and to Alex Cabaj for aiding in making experimental measurements.

This work was supported by the Natural Sciences and Engineering Research Council of Canada. Computational facilities were provided by ACEnet (funded by the Canada Foundation for Innovation, the Atlantic Canada Opportunities Agency, and the provinces of Newfoundland and Labrador, Nova Scotia, and New Brunswick).

Contents

List of Tables

List of Figures

Chapter 1

Introduction

1.1 Motivation

1.1.1 Radiative Forcing

Efforts to curb the human impact on climate often focus on reducing emissions of harmful chemicals into the atmosphere; this requires a quantifiable measure of what is considered harmful. One example of a harmful effect is the depletion of the stratospheric ozone layer by catalytic chemical reactions resulting from emissions of chlorine/bromine-containing chemicals. A second harmful effect of emissions into the atmosphere is their impact on the radiation budget by trapping outgoing radiation and thus heating the planet. The radiation budget of the atmosphere is composed of various energy fluxes as shown in Figure 1.1. Different emissions into the atmosphere can affect the radiation budget, with the global temperature adjusting to restore equilibrium between outgoing and incoming radiation.

Radiative forcing (RF) is a measure of how much a species (or other forcing agent) can alter the radiation budget of the atmosphere and is measured in units of Wm^{-2}. In this work, RF is defined for a change in radiation at the tropopause, which has been shown to correlate with surface temperatures [2]. Compounds containing C-F bonds, such as fluorinated alcohols, absorb strongly in an optically thin region of the atmosphere known as the atmospheric window (750-1250 cm^{-1} or 8-14 μm), which in turn results in positive RF. The atmospheric absorption spectrum is shown in Figure 1.2 and the atmospheric window can be seen. Quantifying a change in the radiation budget due to an emission is useful for policy makers when it comes to deciding on possible restrictions on those emissions. In order to combat stratospheric ozone depletion and to protect the ozone layer, the Montreal Protocol was signed to restrict the emission of chlorofluorocarbons

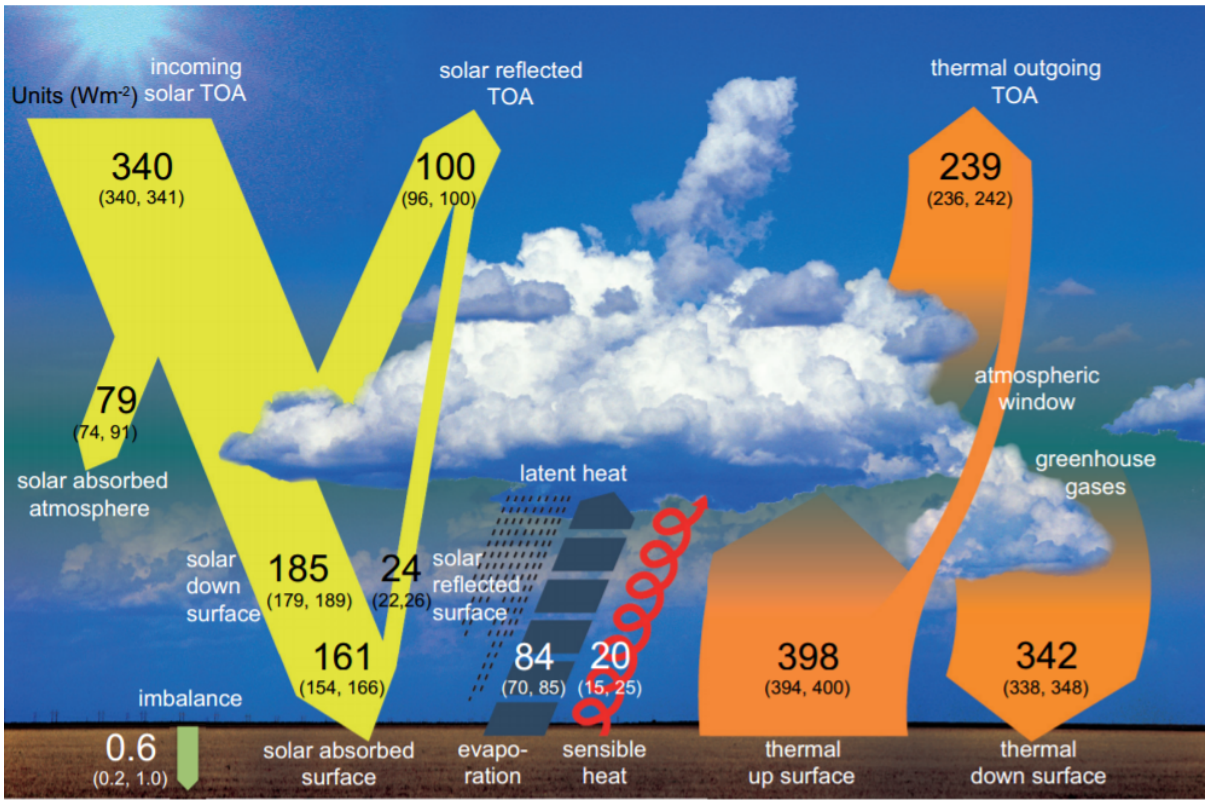

Figure 1.1: Global mean energy budget under present-day climate conditions. Numbers state magnitudes of the individual energy fluxes, adjusted within their uncertainty ranges to close the energy budgets. Numbers in parentheses attached to the energy fluxes cover the range of values in line with observational constraints. Image taken from the Intergovernmental Panel on Climate Change (IPCC) Fifth Assesment Report (AR5) [6].

(CFCs) and later hydrochlorofluorocarbons (HCFCs), compounds involved in chemical reactions that destroy ozone. Similarly, the Kyoto Protocol was signed to reduce emissions of greenhouse gases to combat global warming.

While there exist doubts about the effectiveness of the Kyoto Protocol [1], the Montreal Protocol and its subsequent amendments have been hailed as a success, resulting in the phaseout of CFCs and HCFCs, which is expected to gradually lead to recovery of the ozone layer. Coincidentally, the Montreal Protocol is also considered an effective climate change agreement, as CFCs and HCFCs banned by the Montreal Protocol are also strong greenhouse gases. Hydrofluorocarbons (HFCs) and perfluorocarbons (PFCs) are different classes of chemicals used as replacements for CFCs and HCFCs. Figure 1.3 shows the RF from different chemical groups. While CFCs have the largest RF of halocarbons in the atmosphere, followed by HCFCs, their replacements are still significant greenhouse gases; despite their low mixing ratios, halocarbons contribute a significant amount to

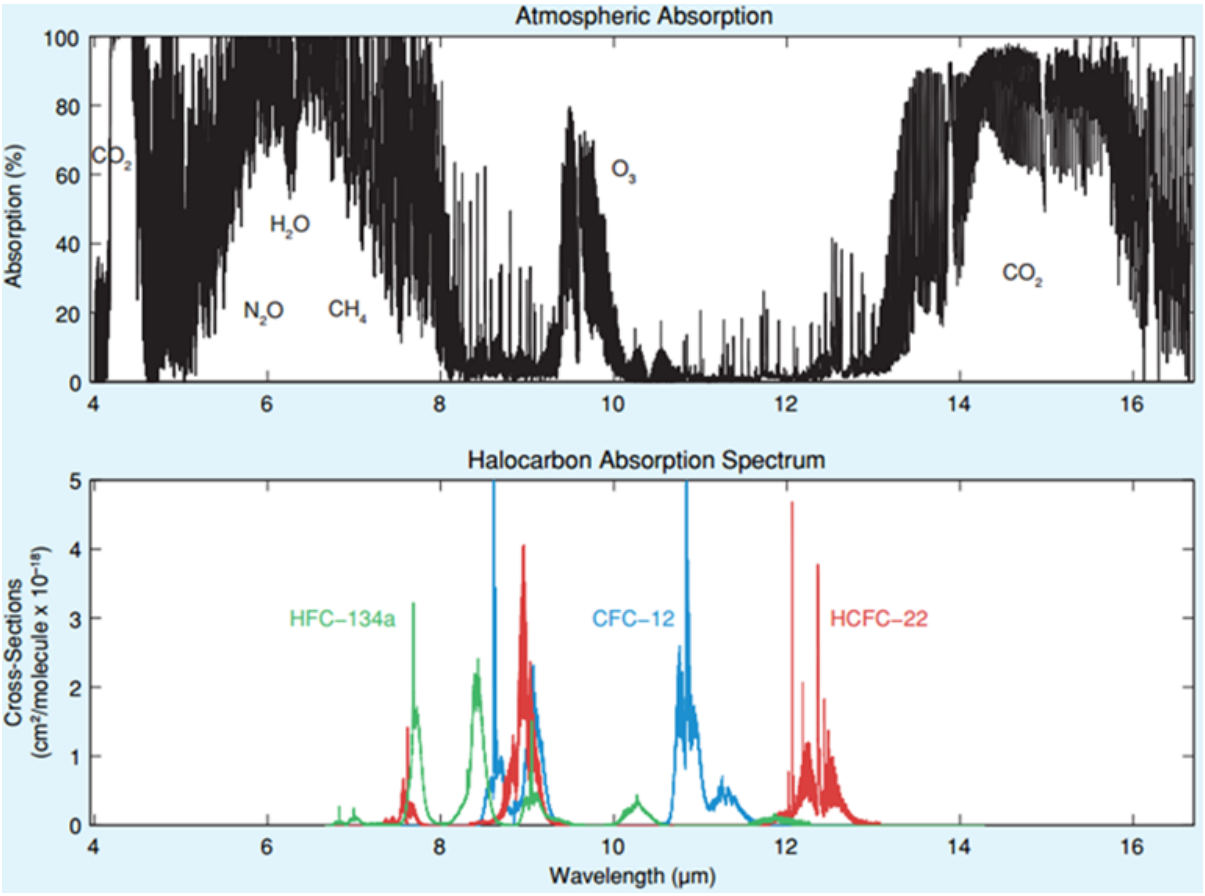

Figure 1.2: The top panel shows the atmospheric absorption of infrared radiation. The bottom panel shows the spectra of select halocarbons, highlighting that halocarbon absorption typically lies in between the opaque regions of the atmosphere. Image taken from [2].

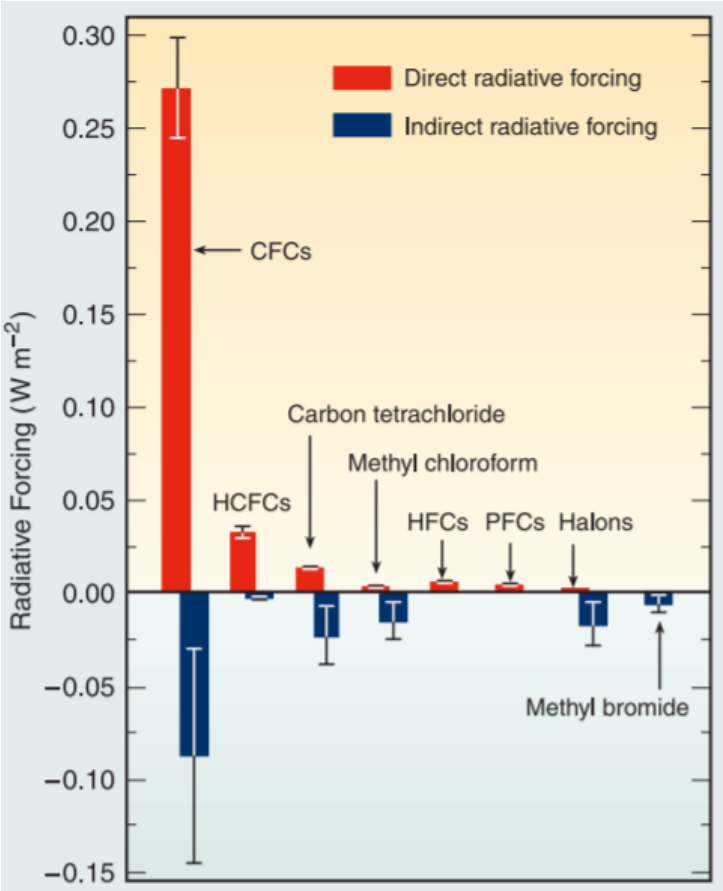

Figure 1.3: Radiative forcing of different chemical families. Direct RF is due to absorption and emission of radiation, whereas indirect RF is due to chemical interactions that influence other gases. Error bars represent 2σ uncertainty. Image taken from [2].

radiative forcing in the atmosphere [5]. Ozone-depleting substances (CFCs and HCFCs) make up 10% of the RF due to greenhouse gases, while PFCs and HFCs comprise 0.2% and 1.0% respectively [2]. The loss of ozone in the stratosphere results in a cooling effect, as absorption of solar ultraviolet radiation by ozone warms the stratosphere. Since ozone-depleting substances (ODSs) are the cause of this ozone loss, the subsequent cooling is considered an indirect effect of ODSs. The net radiative effect of ODSs is still one of increased warming, as shown in Figure 1.3. Recently the Montreal Protocol was amended to include compounds that do not contribute directly to ozone depletion, but have a large impact on the atmospheric radiation budget [3], such as HFCs.

The importance of policies on emissions can also be shown by looking at possible future scenarios. The IPCC's Special Report on Emissions Scenarios (SRES) defines several possible scenarios for future emissions of greenhouse gases [4]. The A1B scenario is for a future of rapid economic growth, global population peaking mid-century, and

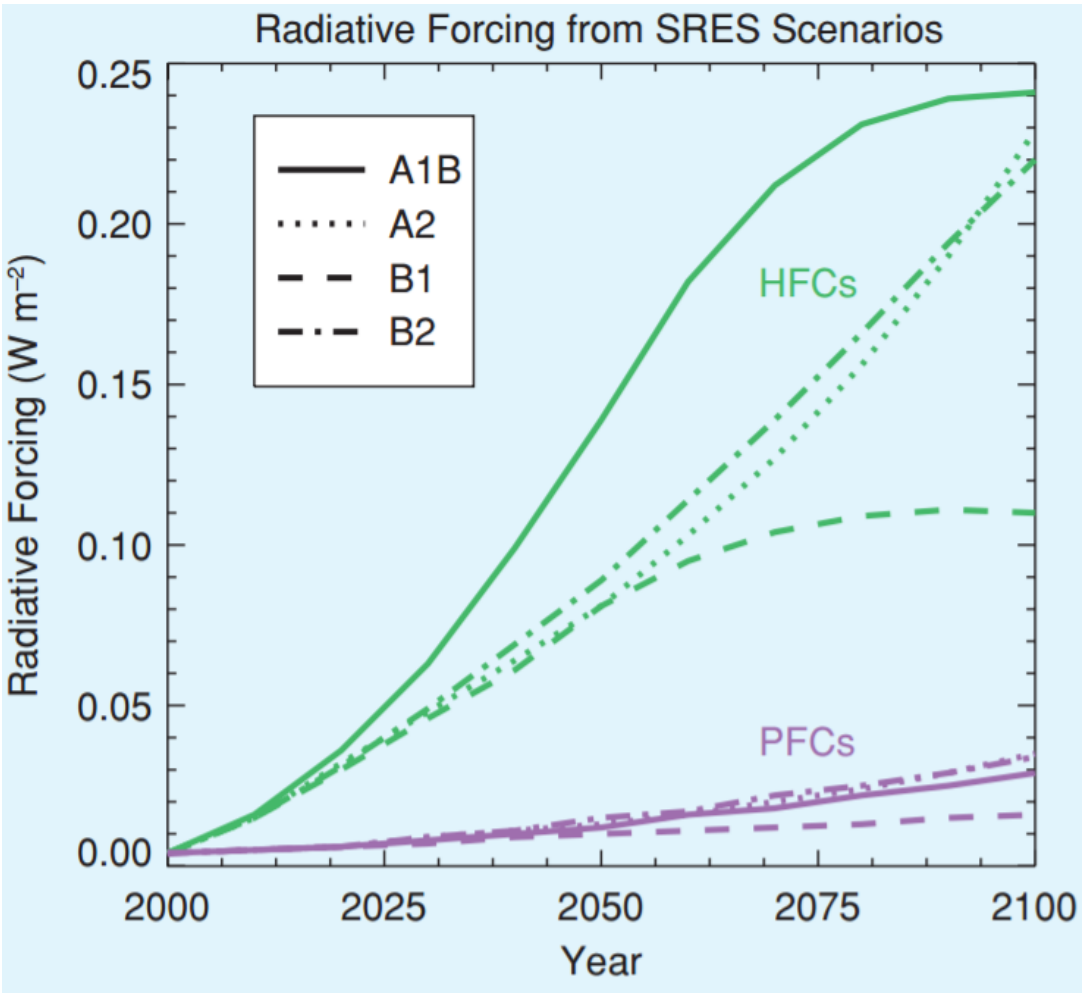

Figure 1.4: Projected RF from HFCs and PFCs based on the A1B, A2, B1 and B2 SRES scenarios. Image taken from [2].

rapid technological development where energy sources are balanced between fossil fuels and other sources. The A2 scenario is similar to A1B, but with slower growth, and a continually increasing global population. The B1 scenario has the same population growth as A1B, but with a focus on global sustainability. The B2 scenario is has a population growth similar to A2, and focuses on local sustainability. Figure 1.4 shows how RF from halocarbons is expected to increase under the different SRES scenarios. Without global policies on emissions, RF contributions from halocarbons are expected to increase significantly. A breakdown of expected RF due to different halocarbons for the A1B scenario is shown in Figure 1.5, with total RF due to halocarbons peaking at $0.4\,\mathrm{Wm}^{-2}$.

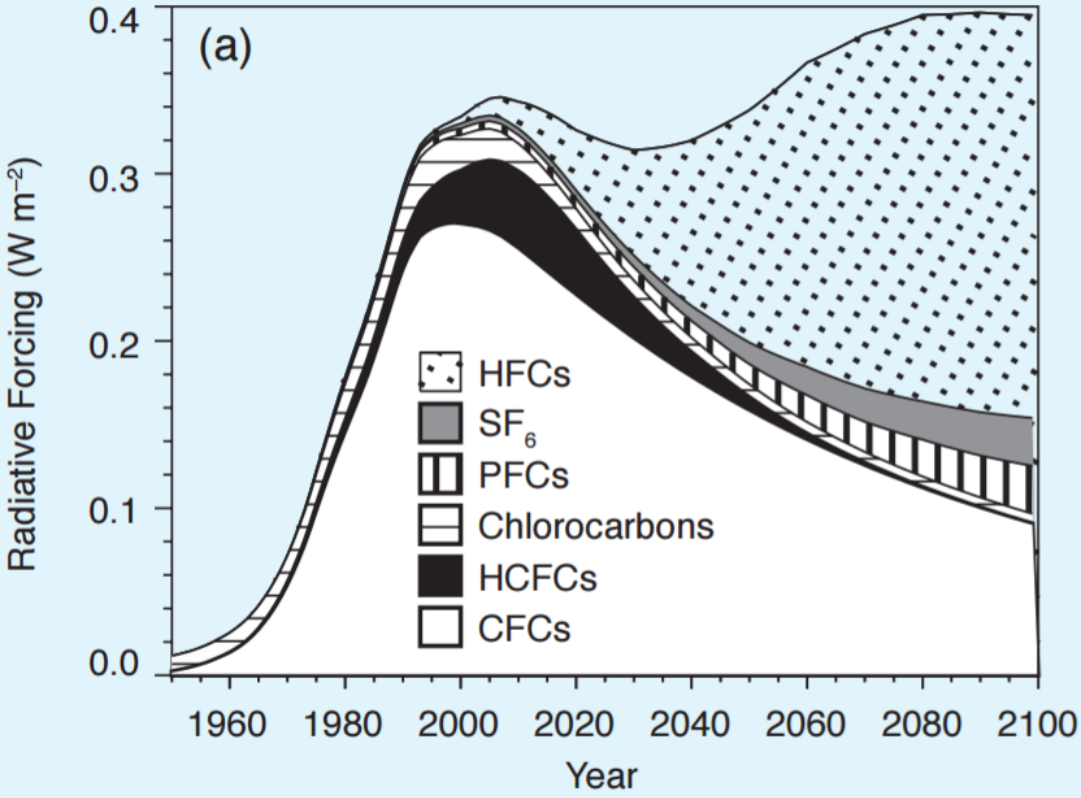

Figure 1.5: Projected RF for different types of gases in the A1B scenario. Image taken from [2].

1.1.2 Laboratory Spectroscopy for Climate Impact Metrics

A global warming potential (GWP) is a useful metric to define the radiative impact of a chemical on the atmosphere. A GWP quantifies the RF of a unit mass of a trace gas compared to an equal mass of carbon dioxide, while taking into account the lifetime of the species in the atmosphere. A GWP is defined over a time horizon, commonly taken to be 100 years. A full description of the GWP will be provided later in Section 2.6. At this point it is convenient to define another radiative quantity, the radiative efficiency (RE), which is RF per unit change in mixing ratio. RF is assumed to be linear with RE, which is valid for low mixing ratios of halocarbons. Thus, the RF of a trace gas can be calculated from its RE, which in turn can be calculated directly from its absorption cross-section which will be shown in Section 2.6. Figure 1.6 shows a selection of GWPs for molecules covered under both the Montreal and Kyoto Protocols.

Broadband absorption cross-sections can be measured in a laboratory, and used to derive RE and hence GWP. However, in practice, the wavenumber range of laboratory measurements can be limited, affecting the accuracy of estimated climate impacts. If experimental data are lacking, theoretically computed spectra, such as those from density functional theory (DFT) calculations can be used [7, 8, 9, 10]. DFT-calculated spectra have the advantage of extending over a larger spectral range compared to experimental spectra. Unfortunately, theoretical calculations tend to have systematic offsets due to approximations to the electronic structure, and need to be scaled to match experimental values before they can be applied to GWP derivations. By combining both experimental and scaled DFT spectra, a composite spectrum can be produced that extends over a larger spectral range and can be used to make more accurate RE calculations. The above discussion can be summarized in the flowchart in Figure 1.7, which shows how an absorption cross-section can be used to calculate a GWP, along with the additional information required to do so.

A recent study calculated the RE and GWP of more than 200 atmospheric species [7]. While most of these were derived from experimental spectra, a significant fraction relied on theoretical calculations. One class of chemicals that was identified as needing improved experimental spectra was fluorinated alcohols. The use of fluorinated alcohols has the potential to increase, as they can be used as replacements for HFCs in electronic and industrial applications and tend to have smaller global GWPs than HFCs [7]. This thesis presents temperature-dependent absorption cross-section measurements, theoretical spectral calculations, and climate impact derivations for the following molecules: perfluorotributylamine (PFTBA), 2,2,3,3,3-pentafluoropropanol (PFPO), 1,1,1,3,3,3-hexafluoro-2-propanol (HFIP), perfluorodecalin (PFDC), and 2H,3H-perfluoropentane

Table SPM-1. GWPs of halocarbons commonly reported under the Montreal Protocol and the UNFCCC and its Kyoto Protocol and assessed in this report relative to CO_2, for a 100-year time horizon, together with their lifetimes and GWPs used for reporting under the UNFCCC. Gases shown in blue (darker shading) are covered under the Montreal Protocol and gases shown in yellow (lighter shading) are covered under the UNFCCC. [Tables 2.6 and 2.7]

Gas	GWP for direct radiative forcing[a]	GWP for indirect radiative forcing (Emission in 2005[b])	Lifetime (years)	UNFCCC Reporting GWP[c]
CFCs				
CFC-12	10,720 ± 3750	−1920 ± 1630	100	n.a.[d]
CFC-114	9880 ± 3460	Not available	300	n.a.[d]
CFC-115	7250 ± 2540	Not available	1700	n.a.[d]
CFC-113	6030 ± 2110	−2250 ± 1890	85	n.a.[d]
CFC-11	4680 ± 1640	−3420 ± 2710	45	n.a.[d]
HCFCs				
HCFC-142b	2270 ± 800	−337 ± 237	17.9	n.a.[d]
HCFC-22	1780 ± 620	−269 ± 183	12	n.a.[d]
HCFC-141b	713 ± 250	−631 ± 424	9.3	n.a.[d]
HCFC-124	599 ± 210	−114 ± 76	5.8	n.a.[d]
HCFC-225cb	586 ± 205	−148 ± 98	5.8	n.a.[d]
HCFC-225ca	120 ± 42	−91 ± 60	1.9	n.a.[d]
HCFC-123	76 ± 27	−82 ± 55	1.3	n.a.[d]
HFCs				
HFC-23	14,310 ± 5000	~0	270	11,700
HFC-143a	4400 ± 1540	~0	52	3800
HFC-125	3450 ± 1210	~0	29	2800
HFC-227ea	3140 ± 1100	~0	34.2	2900
HFC-43-10mee	1610 ± 560	~0	15.9	1300
HFC-134a	1410 ± 490	~0	14	1300
HFC-245fa	1020 ± 360	~0	7.6	–[e]
HFC-365mfc	782 ± 270	~0	8.6	–[e]
HFC-32	670 ± 240	~0	4.9	650
HFC-152a	122 ± 43	~0	1.4	140
PFCs				
C_2F_6	12,010 ± 4200	~0	10,000	9200
C_6F_{14}	9140 ± 3200	~0	3200	7400
CF_4	5820 ± 2040	~0	50,000	6500
Halons				
Halon-1301	7030 ± 2460	−32,900 ± 27,100	65	n.a.[d]
Halon-1211	1860 ± 650	−28,200 ± 19,600	16	n.a.[d]
Halon-2402	1620 ± 570	−43,100 ± 30,800	20	n.a.[d]
Other Halocarbons				
Carbon tetrachloride (CCl_4)	1380 ± 480	−3330 ± 2460	26	n.a.[d]
Methyl chloroform (CH_3CCl_3)	144 ± 50	−610 ± 407	5.0	n.a.[d]
Methyl bromide (CH_3Br)	5 ± 2	−1610 ± 1070	0.7	n.a.[d]

[a] Uncertainties in GWPs for direct positive radiative forcing are taken to be ±35% (2 standard deviations) (IPCC, 2001).
[b] Uncertainties in GWPs for indirect negative radiative forcing consider estimated uncertainty in the time of recovery of the ozone layer as well as uncertainty in the negative radiative forcing due to ozone depletion.
[c] The UNFCCC reporting guidelines use GWP values from the IPCC Second Assessment Report (see FCCC/SBSTA/2004/8, http://unfccc.int/resource/docs/2004/sbsta/08.pdf).
[d] ODSs are not covered under the UNFCCC.
[e] The IPCC Second Assessment Report does not contain GWP values for HFC-245fa and HFC-365mfc. However, the UNFCCC reporting guidelines contain provisions relating to the reporting of emissions from all greenhouse gases for which IPCC-assessed GWP values exist.

Figure 1.6: GWPs for a 100-year time horizon. Image taken from [2].

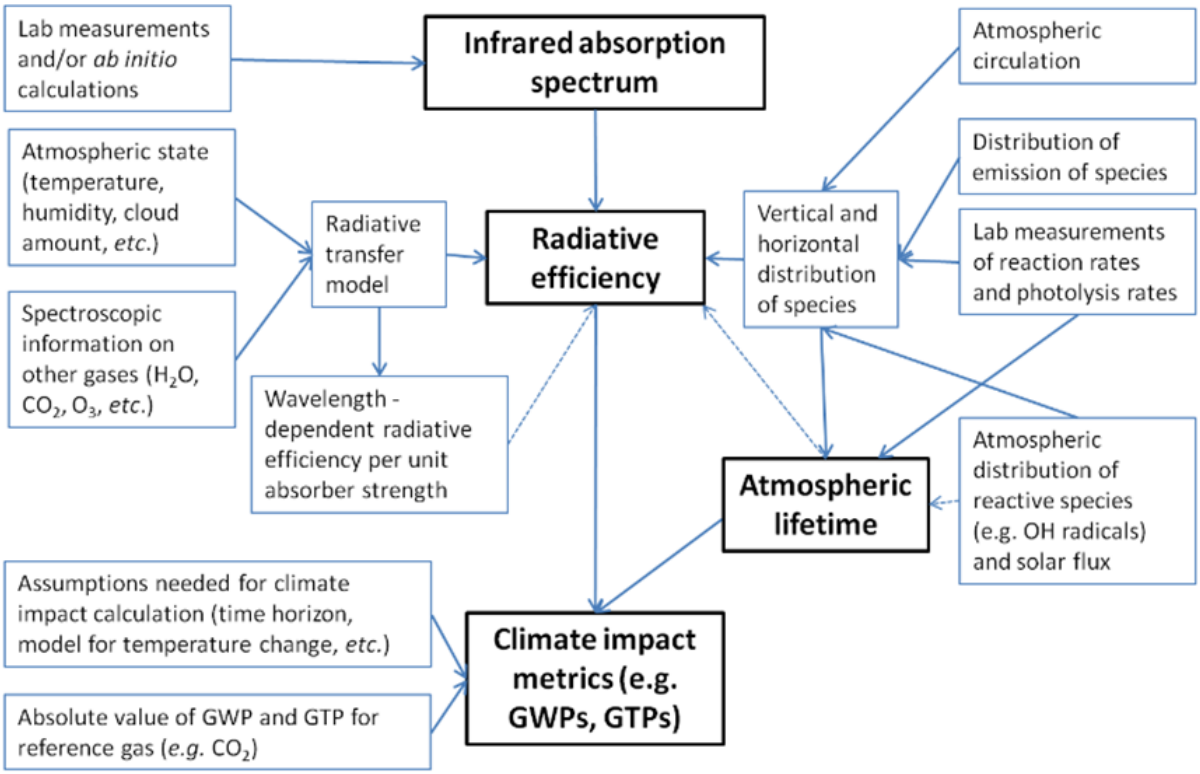

Figure 1.7: Flowchart summarizing GWP derivation from absorption cross-sections. Image taken from [7].

(HFC-43-10mee). These chemicals have been identified as having the potential for increased emissions in the future, yet most of them lack published abundances in the atmosphere. With the exception of HFC-43-10mee, none of the chemicals studied currently are covered under the Montreal or Kyoto Protocols.

PFTBA ($N(CF_2CF_2CF_2CF_3)_3$) is a fully-fluorinated liquid commonly used in electronic reliability and quality testing, such as environmental stress screening and vapor phase soldering processes, and heat transfer fluid for thermal shock testing. PFTBA belongs to the class of perfluoroalkyl amines, which are chemically stable liquids with no known sinks in the atmosphere, resulting in lifetimes of hundreds of years and well-mixed atmospheric distributions. PFTBA is considered a potential long-lived greenhouse gas (LLGHG). PFPO ($CF_3CF_2CH_2OH$) and HFIP ($CF_3CHOHCF_3$) are fluorinated alcohols. PFPO is commonly used to increase volatility of an analyte and to introduce fluorine atoms for better detection limits in gas chromatography applications. HFIP is a specialty solvent for some polar polymers and used in the production of anesthetics. PFDC ($C_{10}F_{18}$) is capable of dissolving large quantities of gases, making it useful for a variety of medical applications, such as liquid breathing. HFC-43-10mee ($CF_3CHFCHFCF_2CF_3$) is used as a cleaning solvent in electronics and has been proposed as a nonflammable solvent for the recovery of radioactive elements.

1.1.3 Laboratory Spectroscopy for Atmospheric Retrievals

Another application of spectroscopy in the atmosphere is for the retrieval of trace gas concentrations. Each atom or molecule has a unique spectral absorption pattern due to its internal energy level structure. These unique absorption spectra can be considered "fingerprints" that signal the presence of a given species. By measuring the interaction of radiation with the atmosphere, the composition of the atmosphere can be determined and changes can be tracked. Under controlled laboratory conditions, absorption parameters of key atmospheric species can be measured for use in atmospheric retrievals. Retrieving the concentration of a trace gas species requires not only reliable spectral parameters of the species of interest, but also those of any species with absorption lines in the same spectral region. In order to obtain accurate retrievals from atmospheric spectra, the uncertainty in laboratory measurements may need to be at sub 1% levels depending on the trace gas and the application. Additionally, interfering gases are causing problems with the residuals of retrievals using spectra from the Atmospheric Chemistry Experiment Fourier Transform Spectrometer (ACE-FTS). In particular, CO_2 lines in the 900-1000 cm^{-1} range are rendering retrievals of C_2H_4 difficult; water vapour lines limit the selection of microwin-

dows for several species, including HCOOH, HCN, and CFC-111 in the collective range of 800-1100 cm^{-1}; improvements in methane lines for the 1140-1280 cm^{-1} range are also needed for ACE retrieval improvements [11]. The HITRAN database has also started to include absorption cross-sections of larger halocarbons, such as the molecules studied in this work, for possible future use in atmospheric remote sensing.

Ultimately, there is a serious shortfall in experimental spectral parameters for a variety of atmospheric applications. A second part of this thesis project involved building a new multiple-pass White cell capable of resolving weak absorption lines. If the cross-section is small, then a long path length can allow for the detection of weak lines. Logistically, longer path lengths are limited by the amount of space physically available. The solution to this problem is to place mirrors at the ends of a cell to allow for multiple passes, in order to achieve a much longer path length; this concept of a multipass cell is known as a White cell, after its inventor [12]. This new system can be used in the future to determine line parameters of key atmospheric species.

1.2 Scientific Objectives

The scientific goals of this work are as follows:

1. **To determine the temperature dependence of absorption cross-sections**: Temperature can have an impact on absorption cross-sections. For the molecules studied, the temperature dependence of their spectra has not been measured and the results included in this thesis are the first known studies of their temperature dependence. Additionally, some of the new experimental spectra will be at a higher resolution and expanded spectral range compared to the previously published data.

2. **To perform DFT calculations and calibrate them against experimental spectra**: DFT-calculated spectra will be evaluated against the experimental spectra. This will allow for the adjustment of DFT band positions outside of the experimental range, increasing the accuracy of the theoretical spectra.

3. **To improve RE and GWP calculations of the species studied**: The RE and GWP values of the species studied are not calculated over the full spectral range of the atmospheric window. By combining our DFT and experimental spectra, we can achieve a more complete RE and GWP calculation and evaluate whether the current published values either underestimate or overestimate the climate impacts of the species studied.

4. **To construct and assemble a new cell for future use**: In order to extract spectral line parameters from weak absorption features, a new multi-pass White cell is being constructed. This new system will be able to accurately measure line parameters needed to improve atmospheric retrievals.

1.3 Previous Work

Currently, the only prior published spectrum of PFTBA was recorded at 296 K at 1.54-4.26 mTorr in a 760 Torr N_2 background at a resolution of 0.25 cm^{-1} using 32 co-added spectra [13]. This same paper also published the first detection of PFTBA in the atmosphere, having a volume mixing ratio (VMR) of 0.18±0.01 pptv. This work showed that PFTBA has the largest RE of any compound detected in the atmosphere, with an RE of 0.86 $Wm^{-2}ppbv^{-1}$. Furthermore, there are no requirements for the production and emission levels of PFTBA to be reported by industry, resulting in high uncertainty of its VMR trend and climate impacts.

Currently, the only published infrared (IR) spectra of PFPO were recorded at room temperature [14, 15, 16, 17] and at a resolution of 1 cm^{-1}; the study by Antiñolo *et al.* [16] was not pure vapour spectra, but was diluted with helium, which can have an impact on the broadening of the spectral lines. The majority of published IR spectra of HFIP were obtained using Raman absorption in CCl_4 solution [18, 19, 20, 21, 22]. There exist a few published vapour spectra of HFIP recorded at 296 K [14, 19, 21], but they do not report absorption cross-section intensities, choosing to focus on line positions and assignments instead. Prior publications of PFDC spectra were made at 296 K over a range of 600-1500 cm^{-1} and a resolution of 0.5 cm^{-1} [23]. The HFC-43-10mee RE value in the IPCC AR5 comes from an unpublished personal communication [7], which warrants further investigation. There also exist three N_2-broadened spectra at 278, 298, and 323 K over a spectral range of 500-6500 cm^{-1} at a resolution of 0.112 cm^{-1} from the Pacific Northwest National Laboratory (PNNL) [24].

In order to enable detection of weak lines, a multipass White cell was partly commissioned in 2007. The inner and outer cells, and transfer optic tanks have all been built. The inner cell has copper tubing around the outer surface that will carry coolant to provide temperature control. Additionally, the majority of the mirrors and the vacuum pumping systems were previously purchased. Most of these mirrors are several years old, so some of the coatings have degraded and the actual reflectivities are lower than expected. A Varian V-701 turbo pump was purchased for pumping down the inner cell. A Varian DS-602 rotary pump was also purchased and will be used as both the backing pump for

the turbo pump and to evacuate the outer cell.

1.4 Contributions

I was responsible for all of the measurements and analysis described in this thesis with the exception of the following contributions from my collaborators:

The Matlab codes used to calculate the zero-Torr limit absorption cross-sections in this work were provided to me by Dr. Karine Le Bris (St. Francis Xavier University). I made some minor modifications to the code to better account for globar fluctuations and propagate the uncertainties from pressure, temperature, and pathlength. Dr. Le Bris also was the lead on PFDC and HFC-43-10mee; she and her summer student, Jasmine DeZeeuw (St. Francis Xavier University), took the HFC-43-10mee and *trans*-PFDC measurements using my experimental apparatus.

Alex Cabaj (University of Toronto) assisted me with performing the PFTBA and PFPO absorption cross-section measurements. Dr. Stephanie Conway (University of Toronto) also assisted with the PFTBA measurements and trained me on how to operate the spectrometer.

Jerry Zhai (University of Toronto) assisted me with the assembly and testing of the D- and T-mirror mounts for the White cell. Additionally he also helped attach and test the thermocouples for the White cell.

Chapter 2

Theory

This chapter explains the theory behind the quantum mechanics of absorption spectra, Fourier transform spectroscopy, and the derivation of RE and GWP.

2.1 Beer-Lambert Law

The absorption of light by a medium at a given pressure and temperature (P, T) can be described by the well-known Beer-Lambert Law:

$$I(\tilde{\nu}) \;=\; I_o(\tilde{\nu})e^{-\chi(\tilde{\nu})} \tag{2.1}$$

where $\tilde{\nu}$ is wavenumber, $I(\tilde{\nu})$ is the intensity after passing through the gas sample (filled cell measurement) and $I_o(\tilde{\nu})$ is the incident intensity (empty cell measurement). $\chi(\tilde{\nu})$ is the optical depth, which for a homogeneous sample in a gas cell is given by:

$$\chi(\tilde{\nu}) \;=\; \rho L\sigma(\tilde{\nu}) \tag{2.2}$$

where ρ is the density, L is the cell length, and $\sigma(\tilde{\nu})$ is the absorption cross-section. The density can be expressed in terms of pressure and temperature as:

$$\rho \;=\; \frac{PT_o}{P_oT}N_L \tag{2.3}$$

where T_o and P_o are standard temperature and pressure (STP) respectively, and N_L is Loschmidt's constant. $\sigma(\tilde{\nu})$ can be found via a linear fit of optical depth versus pressure for a given temperature and wavenumber. All fits have a forced convergence of $\chi = 0$ for $P = 0$. The absorption cross-section depends on pressure, temperature, and the quantum mechanical nature of the absorber.

2.2 Quantum Mechanics

The majority of what follows in this section is taken from [25]. Consider first the time-independent Schrödinger equation for a diatomic molecule:

$$\mathcal{H}\Psi(Q_1, Q_2; q_1, q_2, ...) \;=\; E\Psi(Q_1, Q_2, ..; q_1, q_2, ...) \tag{2.4}$$

where Q_i represent the coordinates of the nuclei and q_i represent the coordinates of the electrons. The Hamiltonian of a molecule can be expressed (ignoring higher order effects) as:

$$\mathcal{H} \;=\; \mathcal{H}_{elc.} + \mathcal{H}_{vib.} + \mathcal{H}_{rot.} + \mathcal{H}_{trans.} \tag{2.5}$$

where $\mathcal{H}_{elc.}$ depends on the motion of the electrons relative to the nuclei, $\mathcal{H}_{vib.}$ depends on the motion of the nuclei relative to each other, $\mathcal{H}_{rot.}$ depends on the rotation of the entire system, and $\mathcal{H}_{trans.}$ depends on the translational energy of the entire system. $\mathcal{H}_{trans.}$ is important for collisional interactions between molecules, but is not the focus of this thesis. If we assume the nuclei are held fixed, then we can solve for $\mathcal{H}_{elc.}$ in an electronic basis:

$$\mathcal{H}_{elc.}\Phi_i(\mathbf{R}; q_1, q_2, ...) = E_i(R)\Phi_i(\mathbf{R}; q_1, q_2, ...) \tag{2.6}$$

where Φ_i are basis functions for each electronic state i, $E_i(R)$ are eigenvalues, and $\mathbf{R}$ is the internuclear position vector. The wavefunction can now be expressed as:

$$\Psi \;=\; \sum_i F_i(\mathbf{R})\Phi_i(\mathbf{R}; q_1, q_2, ...). \tag{2.7}$$

where $F_i(\mathbf{R})$ are wavefunctions representing the nuclear motions. Returning to the full Hamiltonian using this basis and switching to spherical polar coordinates, Equation 2.4 can now be expressed as:

$$\sum_i \left\langle \Phi_s \left| -\frac{\hbar^2}{2\mu}\frac{1}{R^2}\frac{\partial}{\partial R}\left(R^2\frac{\partial}{\partial R}\right) + \frac{\mathbf{N}^2}{2\mu R^2}\right| \Phi_i \right\rangle F_i(\mathbf{R}) + [E_s(R) - E]F_s(\mathbf{R}) = 0 \tag{2.8}$$

where $\mathbf{N}^2$ is the orbital angular momentum operator describing the relative motion of the nuclei and μ is the reduced mass. $\mathbf{N}^2$ is given in spherical polar coordinates as:

$$\mathbf{N}^2 = -\hbar^2\left[\frac{1}{sin(\theta)}\frac{\partial}{\partial\theta}\left(sin(\theta)\frac{\partial}{\partial\theta}\right) + \frac{1}{sin^2(\theta)}\frac{\partial^2}{\partial\phi^2}\right] \tag{2.9}$$

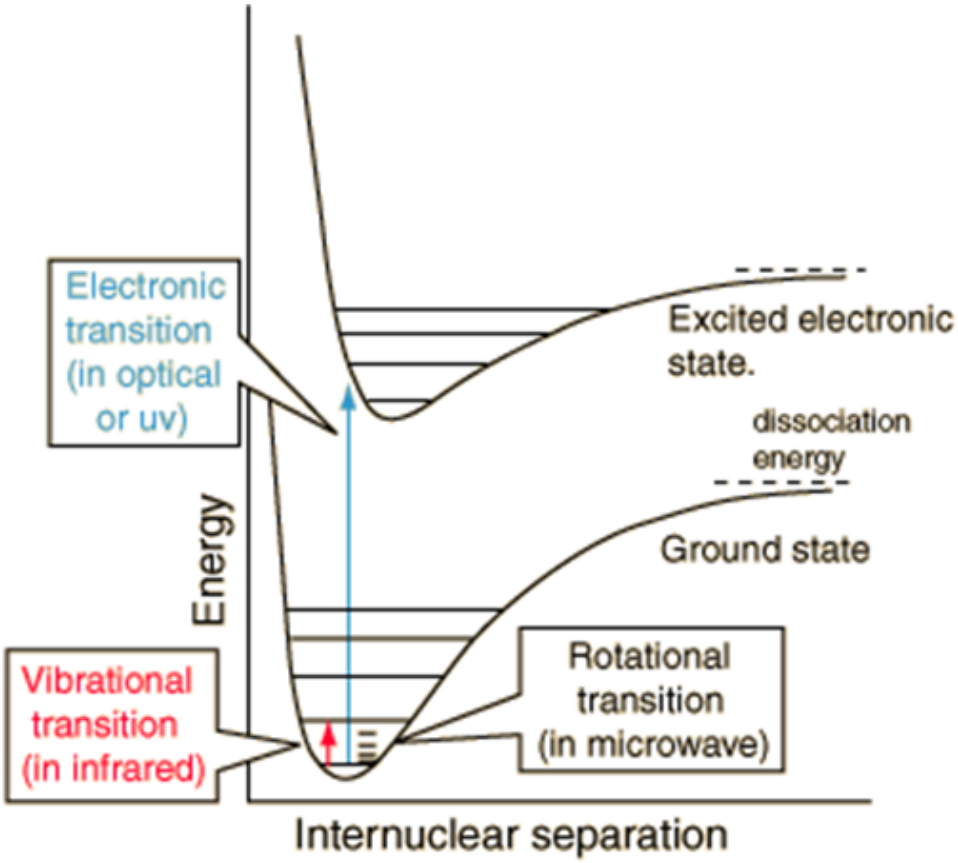

Figure 2.1: General form of the electronic energy of a bound diatomic molecule. Transitions between different electric states are shown along with transitions within an electric state corresponding to vibrations and rotations.

The Born-Oppenheimer approximation assumes that the motion of the electrons is much faster than that of the nuclei due to mass differences, such that the motion of the nuclei has no impact on the motion of the electrons, thus $\partial\Phi/\partial R$ can be neglected compared to $\partial F/\partial R$ and only the diagonal terms of the $\mathbf{N}^2$ operator remain [26]:

$$\left[-\frac{\hbar^2}{2\mu}\frac{1}{R^2}\frac{\partial}{\partial R}\left(R^2\frac{\partial}{\partial R}\right)+\frac{\langle\Phi_s|\mathbf{N}^2|\Phi_s\rangle}{2\mu R^2}+E_s(R)-E\right]F_s(\mathbf{R})=0 \tag{2.10}$$

$E_s(R)$ acts as a potential, allowing the nuclear wave equation to be solved at different internuclear distances. Figure 2.1 shows a typical energy diagram for a diatomic molecule as a function of internuclear distance. The rest of this section will focus on $\mathcal{H}_{vib.}$ and $\mathcal{H}_{rot.}$.

2.2.1 Vibrational Spectroscopy

For a non-linear molecule made up of N nuclei, there are $3N$-6 vibrational degrees of freedom, each one corresponding to a fundamental vibrational mode. Intramolecular vibrations can be approximated as harmonic oscillators about a potential energy minimum. The Hamiltonian of a harmonic oscillator is:

$$\mathcal{H}_{harm.} = -\frac{1\hbar^2}{2\mu}\frac{\partial^2}{\partial x^2} + \frac{1}{2}m\nu x^2 \tag{2.11}$$

where μ is the reduced mass, x is the coordinate of the motion and ν is the frequency of the vibration. From this Hamiltonian, the energy eigenstates are:

$$E_{harm.} = (v + \frac{1}{2})\nu \tag{2.12}$$

where v is the quantum number associated with this oscillator. $\mathcal{H}_{vib.}$ can be expressed as the sum of individual oscillators, one for each fundamental vibrational mode, leading to the vibrational energy of a molecule:

$$E_{harm.} = \sum_{i}^{3N-6}(v_i + \frac{1}{2})h\nu_i. \tag{2.13}$$

In IR absorption spectroscopy, only modes which can induce a change in the electric dipole moment of the molecule (such as a change in the symmetry of the molecule) are considered IR active. Furthermore, it is possible to have combination and overtone vibrations. Generally the amplitudes of these modes are significantly weaker than those of the fundamental modes.

2.2.2 Rotational Spectroscopy

To determine the rotational Hamiltonian, a rigid rotor in field-free space (potential energy, $V = 0$) is assumed. The kinetic energy of a rotation body ($T_{rot.}$) is:

$$T_{rot.} = \frac{1}{2}\sum_{i} I_i\Omega_i^2 \tag{2.14}$$

$$= \frac{1}{2}\sum_{i}\frac{L_i^2}{I_i} \tag{2.15}$$

where I are moments of inertia, Ω are the angular velocities, L is the angular momentum, and the sum is made over the different axes of rotation. This is simplified by choosing

the molecular frame for which the angular momentum operator is diagonal, instead of a fixed space frame where off-diagonal terms may still be present. As the potential energy is zero, the rotational Hamiltonian is:

$$\mathcal{H}_{rot.} = \frac{\hbar^2}{2}\left(\frac{\hat{\mathbf{L}}_a^2}{I_a} + \frac{\hat{\mathbf{L}}_b^2}{I_b} + \frac{\hat{\mathbf{L}}_c^2}{I_c}\right) \tag{2.16}$$

$$= A\hat{L}_a^2 + B\hat{L}_b^2 + C\hat{L}_c^2 \tag{2.17}$$

where A, B, and C are known as rotational constants and the quantum mechanical angular momentum operator has been substituted for classical angular momentum. The $\hat{L}_i$ do not commute with each other, but do commute with the total angular momentum operator, $\hat{L}^2$. Symmetry of the molecule has a significant impact on the structure of rotational spectra. For example, if the molecule is spherically symmetric, $A = B = C$, the rotational levels can be described using only the total angular momentum quantum number J:

$$E_{rot} = BJ(J+1). \tag{2.18}$$

If there is a plane of symmetry and two of the rotational constants are equal, Equation 2.17 can be expressed in terms of $\hat{L}^2$ and one of the two distinct $\hat{L}_i$. Now the rotational energy requires two quantum numbers: J as before and K, the projection onto an axis. If the molecule is an oblate symmetric top ($A = B > C$), the energy levels are:

$$E_{rot} = BJ(J+1) + (C-B)K^2. \tag{2.19}$$

If it is a prolate symmetric top ($A > B = C$), the energy levels are:

$$E_{rot} = BJ(J+1) + (A-B)K^2. \tag{2.20}$$

Unfortunately, if the molecule is asymmetric and none of the rotational constants are equal, there no longer exists a general solution for the energy and it has to be approximated numerically. J can still be assigned as before, but isn't sufficient to fully identify the state of the molecule. Knowledge of a molecule's symmetry is vital to understanding its rotational spectra.

The energy spacing of rotational lines is determined by the rotational constant. For a spherically symmetric molecule, the rotational lines are equally spaced, with spacing equal to twice the rotational constant. Thus the heavier a molecule (or the greater the

bond length), the smaller the rotational constant, and thus the closer the rotational lines are to each other. This general principle of rotational line spacing dependent on rotational constants applies to other molecular geometries as well. As the weight of a molecule increases, the spectral resolution of the experiment must also increase in order to still resolve individual rotational lines. When a molecule undergoes a transition from one vibrational level to another, this can be coupled with a transition in rotational state as well. If this happens, the selection rules require that ΔJ=-1, 0, or +1; these are known as the P, Q, and R branches respectively. Note that the Q branch only exists for polyatomic molecules or diatomic molecules with electronic angular momentum in the ground state, because $\Delta J = 0$ is allowed for transitions where the change in dipole moment is perpendicular to the molecular symmetry axis.

2.3 Lineshapes

The cross-section has a strong dependence on wavenumber as absorption only takes place if the frequency of the light matches an energy transition in the molecule. In practice, these transitions are not sharp peaks of infinitesimal width; they are broadened by a variety of processes. Thus a line requires more than just the centre absorption frequency to characterize it; it also requires additional information such as width, broadening coefficient, and line strength. The majority of what follows in this section is taken from [27]. The line strength (S) can be expressed as:

$$S = \int \sigma \cdot d\tilde{\nu} \tag{2.21}$$

where σ is the cross-section. There are many factors that determine lineshapes. The first of these processes is natural broadening due to the Heisenberg Uncertainty Principle, which results in all lines having a Lorentzian shape, where the width depends on the rates of spontaneous decay. For atmospheric purposes in the IR, natural broadening is negligible, so it will not be discussed further.

The next type of broadening is Doppler broadening. The frequency of light observed by an absorber is shifted based on the absorber's motion relative to the light source. As absorption depends on frequency, this relative motion shifts the frequency at which a transition is observed. For a Maxwell-Boltzmann distribution of velocities in a gas, the Doppler Effect results in a spectral line broadening, which is given as:

$$\sigma_D = \frac{S}{\alpha_D\sqrt{\pi}} exp(-\frac{(\tilde{\nu}-\tilde{\nu}_o)^2}{\alpha_D^2}) \tag{2.22}$$

where $\tilde{\nu}_o$ is the wavenumber of the transition, and α_D is the Doppler line width given by:

$$\alpha_D = \tilde{\nu}_o \sqrt{\frac{2k_b T}{mc^2}} \tag{2.23}$$

where k_b is the Boltzmann constant, T is temperature, m is mass of the absorber, and c is the speed of light. A Doppler-broadened line has no pressure dependence, but the width does have a temperature dependence.

A third type of broadening results in a Lorentz or pressure or collision broadened line. Collisions between molecules can result in distortion of the energy levels, which causes a broadening of the spectral lines. These collisions can either be self induced or from collisions with a background gas. As the pressure increases, the mean free path of a molecule is reduced, resulting in more collisions per unit time. The mathematical form of Lorentz broadening is:

$$\sigma_L = \frac{S}{\pi} \frac{\alpha_L}{(\tilde{\nu} - \tilde{\nu}_o)^2 + \alpha_L^2} \tag{2.24}$$

where α_L is the Lorentz line width (half-width at half maximum), which is given by:

$$\alpha_L = \alpha_o \left(\frac{P}{P_o}\right) \left(\frac{T_o}{T}\right)^{\frac{1}{2}} \tag{2.25}$$

where α_o is the half-width at STP. Lorentz broadening dominates in regimes where pressures are high, but collision time between molecules can be considered negligible.

In the event that neither Lorentz nor Doppler broadening dominates, a convolution of the two can be used to represent the lineshape. This is known as a Voigt lineshape given by:

$$\sigma_V = \frac{S}{\pi^{3/2}} \frac{\alpha_L}{\alpha_D} \int_{-\infty}^{\infty} \frac{1}{(\tilde{\nu} - \tilde{\nu}_o)^2 + \alpha_L^2} exp\left(-\frac{(\tilde{\nu} - \tilde{\nu}_o)^2}{\alpha_D^2}\right) d\tilde{\nu}. \tag{2.26}$$

The Voigt lineshape is useful for most atmospheric purposes, but it also has limitations. Problems arise when approximating the nature of collisions. If the collisions change the velocity of the molecule, then Dicke narrowing is seen. This is primarily observed in cases where the mean free path is shorter than the wavelength of a transition [28]. If a soft collision model is assumed, *i.e.* the collision has a negligible effect on the absorber motion, then a Galatry lineshape profile results [29]. Conversely if a hard collision is assumed, then a Nelkin-Ghantak profile (NGP) should be used [30]. This can be expanded by including speed-dependent effects to get a speed-dependent NGP (SDNGP). The current lineshape recommended by the high-resolution transmission molecular absorption

database (HITRAN) [31] is a partially correlated quadratic speed-dependent hard collision model known as the Hartmann-Tran profile (HTP) [32]. This lineshape depends on six different parameters and has the advantage that it returns simpler lineshapes by setting some of the parameters to zero; furthermore, it is not significantly more computationally expensive than the Voigt lineshape. Studies comparing increasingly complex lineshape models have found that differences of up to 4% can exist between the line parameters from different models [28, 33]. In order to achieve errors in line parameters smaller than 1%, it is important to know what effects dominate in the experiment, so that the correct model is used.

In addition to broadening effects, line mixing must sometimes be taken into account. The above discussion assumed that the lines were all independent with no overlap; however, this is often not the case. If two lines are closely spaced, there is significant overlap between them such that the lines cannot be described by the sum of separate line profiles. Line mixing can also lead to asymmetrical lineshapes, especially at low densities [34].

Additional temperature dependence of absorption cross-sections can be attributed to a change in energy state population distribution. As temperature increases, more high energy states become occupied (this can be calculated from a Maxwell-Boltzmann distribution). As more states are initially populated, more transitions can become accessible, thus changing the appearance of the spectrum. Furthermore, more complicated molecules usually have several stable conformations, each of which will have slightly different energy level spacing, which leads to different cross-sections. A measured cross-section is then a weighted average of the individual cross-sections of each conformation. Again, with increasing temperatures, the relative population of the different conformations changes, thus changing the weighting of the cross-sections. By examining changes in absorption spectra with temperature, absorption bands can be assigned to specific conformations as an increase (decrease) in absorption is correlated to an increase (decrease) in the population of the conformer.

Large molecules with high molecular weights have large moments of inertia, hence small rotational constants, which results in a high density of rotational-vibrational transitions. Inherently, it is difficult to obtain precise lineshapes for heavy molecules, as their infrared absorption spectra characteristically possess broad bands arising from the overlap of multiple individual spectral transitions, combination bands, and hot bands; making it difficult to resolve line-by-line transitions. For the molecules studied here, the high density of spectral lines and line overlaps are such that it is impossible to resolve individual lines; a resolution greater than $0.004\,\mathrm{cm}^{-1}$ would be needed to resolve all rotational lines. Furthermore, as will be explained in Section 2.6, only a resolution of $0.1\,\mathrm{cm}^{-1}$ is needed

to evaluate RE and GWP. In this case, instead of attempting to extract line parameters, it is more convenient to integrate the absorption cross-section and report the integrated band strength for a defined wavenumber region $\tilde{\nu}_1$ to $\tilde{\nu}_2$:

$$S = \int_{\tilde{\nu}_1}^{\tilde{\nu}_2} \sigma(\tilde{\nu}) d\tilde{\nu}. \tag{2.27}$$

Equation 2.27 is used to quantify the absorption cross-sections of the molecules described in Section 1.1.2, as they are heavy molecules with densely spaced lines; whereas for the retrieval studies described in Section 1.1.3, the Voigt lineshape is typically used, although more accurate lineshapes, such as the Hartmann-Tran profile, are gradually being introduced into retrieval algorithms.

2.4 Fourier Transform Spectroscopy

The main component of the Fourier transform spectrometer (FTS) used in this work is a Michelson interferometer. A Michelson interferometer works by splitting an input beam into two paths. Mirrors at the ends of the paths send the light back, where it recombines into the output beam. While the beam is split, one of the mirrors is moved to vary the path length. This sets up an interference pattern when the beam is recombined.

As a simple example, consider a monochromatic input beam. As the path difference changes, the intensity at the detector will vary sinusoidally as the beams constructively/destructively interfere. The interferometer has taken a single input frequency (e.g., a delta function) and transformed it into a sinusoid; therefore the interferometer has performed a Fourier transform on the signal. In practice, a Fourier transform of the signal recorded at the detector is used to get the original spectrum.

Assuming an ideal interferometer, the rigorous mathematics are as follows (taken from [35]): start with the intensity of a beam as a time-averaged product of the electric field as a function of position (r) and time (t):

$$I = \left\langle \bar{E}^*(\vec{r}, t) \cdot \bar{E}(\vec{r}, t) \right\rangle, \tag{2.28}$$

where the electric field can be expressed as:

$$\bar{E}(\vec{r}, t) = \int_{-\infty}^{\infty} \sqrt{B(\nu)} exp(2i\pi(t\nu + \vec{r} \cdot \vec{k}(\nu))) d\nu, \tag{2.29}$$

where ν is the frequency, $\vec{k}$ is the wavevector, and $\sqrt{B(\nu)}$ is the amplitude for a given frequency. The difference in path length can be expressed as a time delay in the signal

from the changing path. This will be denoted by τ. The outgoing electric field is a superposition of two components with a time delay between them. This leads to a new form of Equation 2.28:

$$I_{out} = \left\langle \left[\frac{\bar{E}(\vec{r},t)}{2} + \frac{\bar{E}(\vec{r},t+\tau)}{2} \right]^* \cdot \left[\frac{\bar{E}(\vec{r},t)}{2} + \frac{\bar{E}(\vec{r},t+\tau)}{2} \right] \right\rangle. \tag{2.30}$$

Substituting Equation 2.29 into Equation 2.30 and simplifying eventually leads to:

$$I_{out} \ = \frac{I_o}{2} + \int_{-\infty}^{\infty} \frac{B(\nu)}{2} cos(2\pi\nu\tau) d\nu. \tag{2.31}$$

By having the detector AC coupled, only the second term in Equation 2.31 is measured. Converting from time delay and frequency space to path difference (δ) and wavenumber ($\tilde{\nu}$) space and taking the Fourier transform of Equation 2.31 yields the ideal source spectrum:

$$B(\tilde{\nu}) \ = \int_{-\infty}^{\infty} I(\delta) exp(-i2\pi\tilde{\nu}\delta) d\delta. \tag{2.32}$$

In practice the finite path difference places a limited resolution on Equation 2.32. Say the optical path difference (OPD) varies from -L to L. The interferogram can be multiplied by a boxcar function equal to 1 between -L and L, and 0 elsewhere. This multiplication is equivalent to convolving the Fourier transform of the intensity with the Fourier transform of a boxcar function (the *sinc* function). This leads to a modification of Equation 2.32,resulting in an instrument lineshape for a monochromatic intensity:

$$B(\tilde{\nu}) \ = 2L sinc(2\pi(\tilde{\nu} - \tilde{\nu}_o)L). \tag{2.33}$$

Resolution can be defined as the distance between the first zeros of the *sinc* function, which in this case is $1/L$. Thus, $1/L$ is the distance at which two lines will be fully resolved, but lines will first appear to be resolved at the half-width half-maximum of the *sinc* function, which is $0.66/L$. This is known as the unapodized resolution criterion. Some definitions are based on a 20% dip between lines, which leads to a resolution criterion of $0.73/L$. A downside to the boxcar function is that it can produce large side lobes that can obscure weaker lines. A different function can be used for convolution that has smaller side lobes; this is known as apodization. While apodization allows for smaller side lobes, it comes at a cost of reduced resolution. A boxcar apodization is applied in this work.

2.5 Density Functional Theory

The field of computational chemistry seeks to use computers to approximate the solution to the Schrödinger equation for molecules, thus allowing for the prediction of molecular geometry, potential energy surfaces, vibrational modes, and light interactions. Computational methods are broken down into two main categories: *ab initio* and semi-empirical. *Ab initio* methods are based entirely on physical constants and quantum mechanics. In principle an *ab initio* calculation can give an exact result if there are no approximations to the Schrödinger equation of the system and computational time is not an issue. However, even for small molecules, solving the Schrödinger equation is incredibly computationally expensive, so approximations need to be made.

The simplest *ab inito* theory is Hartree-Fock theory (HF). In HF, the wave function of the system is approximated by a single Slater determinant. A Slater determinant is an expression for a wavefunction of a system (Ψ) made from wavefunctions of N individual particles (χ) that satisfies anti-symmetry requirements (*e.g.* Pauli exclusion principle), as shown in Equation 2.34:

$$\Psi(\mathbf{x}_1, \mathbf{x}_2, ..., \mathbf{x}_N) = \frac{1}{\sqrt{N!}} \begin{vmatrix} \chi_1(\mathbf{x}_1) & \chi_2(\mathbf{x}_1) & ... & \chi_N(\mathbf{x}_1) \\ \chi_1(\mathbf{x}_2) & \chi_2(\mathbf{x}_2) & ... & \chi_N(\mathbf{x}_2) \\ \vdots & \vdots & \ddots & \vdots \\ \chi_1(\mathbf{x}_N) & \chi_2(\mathbf{x}_N) & ... & \chi_N(\mathbf{x}_N) \end{vmatrix} \tag{2.34}$$

where $\mathbf{x}_i$ refers to the position of an individual particle. Each electron experiences a mean field generated by the other particles, with a stable state found through an iterative process.

The other class of computational methods are known as semi-empirical methods. These methods include empirical additions to the calculations that can greatly reduce the computational cost, but do not have a physical basis. One of the more popular semi-empirical methods is DFT. Instead of trying to solve a multi-electron wavefunction, DFT solves the energy of an electronic systems in terms of the electron probability density. Thus the energy is a function of the electron density, which is a function of position, *i.e.* energy is a functional of electron density [36]. Explicitly the energy, E, of an n-electron system is:

$$E[\rho] = -\frac{\hbar^2}{2m_e}\sum_{i=1}^{n}\int \psi_i^*(\mathbf{r}_1)\nabla_1^2\psi_i(\mathbf{r}_1)d\mathbf{r}_1 - \frac{e^2}{4\pi\epsilon_o}\sum_{I=1}^{N}\frac{Z_I}{r_{I1}}\rho(\mathbf{r}_1)d\mathbf{r}_1 + \frac{e^2}{8\pi\epsilon_o}\int\frac{\rho(\mathbf{r}_1)\rho(\mathbf{r}_2)}{r_{12}}d\mathbf{r}_1 d\mathbf{r}_2 + E_{xc}[\rho] \tag{2.35}$$

where ρ is the electron density, ψ are one-electron spatial orbitals, the second term is the sum of electron nuclei attractions over N nuclei with atomic number Z_I, and E_{XC} is the exchange-correlation energy of the system and is also a functional of ρ [37]. The exact analytical form of E_{XC} is unknown and is obtained using approximate expressions of empirically derived functional.

One of the most commonly used functionals is the B3LYP (Becke, 3-parameter, Lee-Yang-Parr) functional [37]. B3LYP is a hybrid functional that approximates the exchange-correlation energy of electrons in a multi-electron system. It is called a hybrid because a portion of it includes the exact-exchange energy from Hartree-Fock theory along with an empirical correlation. This is usually done as a linear combination of Hartree-Fock exact exchange functionals, with the weights of each term determined empirically.

The basis set used to form a wavefunction of a system is also important. Generally, the basis set is of atomic orbitals; usually *s, p*, and *d* orbitals approximated using Gaussian functions. Valence electrons are more heavily involved in bonding in molecules than the core electrons; as such, valence electrons are more important in DFT calculations and are often represented by more than one basis function; this is known as split-valence basis sets. The usual notation for split-valence basis sets is X-YZWg, where X is the number of primitive Gaussians for the core atomic orbital basis function; Y, Z, and W are the number of primitive Gaussians in the valence orbital basis functions.

Accuracy in theoretical spectra calculations depends on the complexity of the basis set of functionals used to describe the electron density. The basis set can be further augmented with diffuse and polarization functions. Polarization functions are the inclusion of atomic orbitals simulating *p, d*, and *f* orbitals. The notation G(3*df*, 3*pd*) indicates that polarization functions have been added for both light and heavy atoms. Diffuse functions are the addition of shallow Gaussians to better simulate the tail ends of the orbitals. The notation is + or ++ if they are added to heavy atoms or both heavy and light respectively. For simulating the spectra of halocarbons, DFT is found to better predict the locations of the vibrational bands compared to other computational methods [8, 9, 10]. For this reason, along with its reduced computational costs, DFT is used in this thesis, specifically the B3LYP functional with a minimum basis set of 6-311+G(*d,p*), as this was

the most complex basis set that was able to converge for all molecules investigated.

Theoretical DFT calculations were performed using *Gaussian* 03 [50] to predict the optimal molecular geometry and harmonic frequencies corresponding to the vibrational modes of the species studied. *Gaussian* 03 has a simple user interface where the molecules can be assembled and given a rough approximation of the geometry. From this initial user defined geometry, the program uses DFT to find the stable electronic configuration. From this electronic structure, force constants can be found to evaluate the strength of the normal vibrational modes.

The vibrational bands found by DFT represent the ground state transitions; therefore they do not include hot bands, combination bands, or overtone bands, which are found in experimental spectra, making if difficult to model temperature dependence of a DFT spectrum. What can be modeled is the temperature dependence of the ratio of different conformers using the energy of the conformers and a Maxwell-Boltzmann distribution. Since the spectrum observed is a weighted sum of the spectra of individual conformers, a partially-temperature dependent DFT spectrum can be found by changing the weighting of the individual DFT conformer spectra with temperature. This is what will be referred to as a temperature-dependent DFT spectrum in this work, one with changing weights on the spectra of individual conformers.

2.6 Radiative Efficiencies and Global Warming Potentials

To calculate the RE in this work, the method developed by Pinnock *et al.* [38], which allows for the calculation of RE directly from the absorption cross-sections, was used. Pinnock's method involves running a radiative transfer model to derive the wavelength-dependent RE for a weak absorber with the same cross-section at all wavelengths, resulting in the RE per unit cross-section per wavenumber, known as a Pinnock's curve. Multiplying a true cross-section by the Pinnock's curve, at each wavenumber and then integrating the product over the atmospheric window range yields the instantaneous RE. This method achieves less than 1% difference in RE for a variety of greenhouse gases compared to a full radiative transfer model calculation involving the target greenhouse gas [38]. The authors stress that this is a comment on the Pinnock's method's precision, not its accuracy.

The original Pinnock's curve was calculated based on the mean atmospheric instantaneous cloudy-sky RF in 1995 [38]. Hodnebrog *et al.* [7] calculated an updated curve in

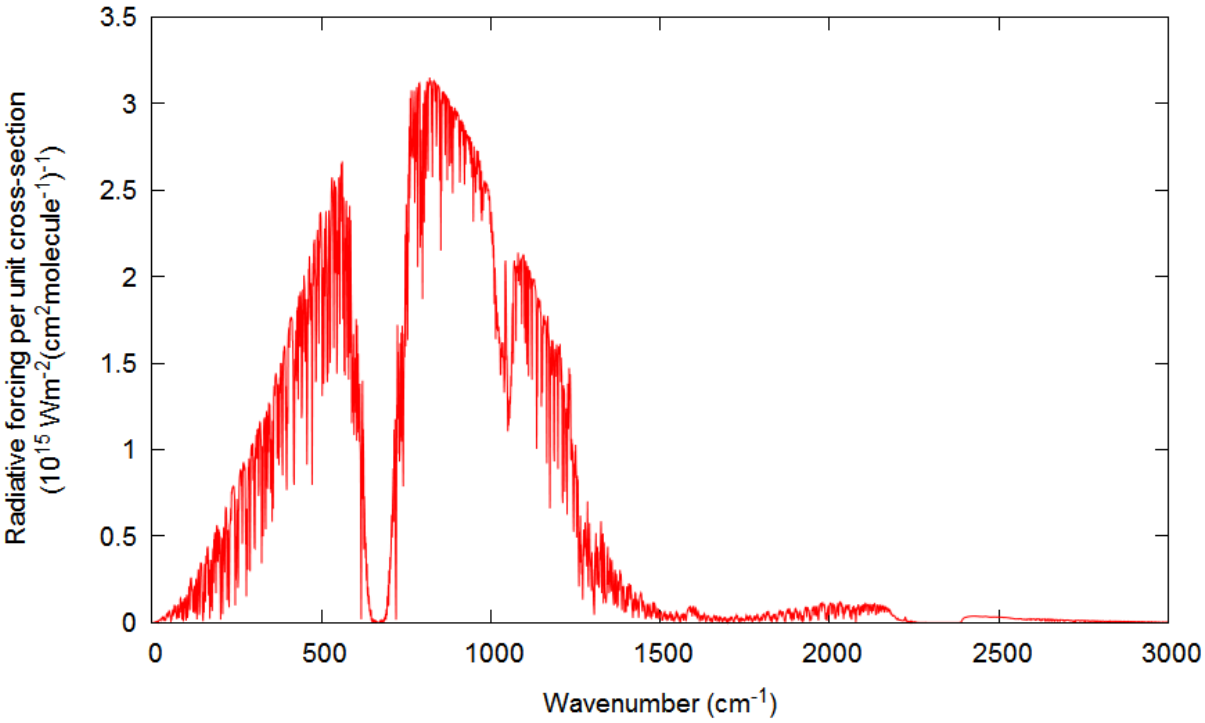

Figure 2.2: Pinnock's curve plotted using the Oslo LBL model at a resolution of 1 cm^{-1}. Oslo LBL model data taken from [7].

2012 that uses 1 cm^{-1} bins and newer atmospheric data; the new Pinnock's curve is calculated using the Oslo line-by-line (LBL) model employing a two atmosphere approach, *i. e.* one for tropics the (30N30S) and one for the extratropics (30N90N and 30S90S), instead of one global mean atmosphere. The updated Pinnock's curve is shown in Figure 2.2. Hodnebrog *et al.* [7] state that this method of calculating the RE has an uncertainty of 5% from the radiation scheme, 5% from accounting for clouds, 3% from water vapour distribution, 3% from surface and atmospheric temperature, 5% from tropopause level, 1% from temporal and spatial averaging, and the uncertainty from the absorption cross-section. For theoretical spectra, they estimate the uncertainties on absorption cross-sections to be approximately 10%. The uncertainty on REs is the sum in quadrature of these listed uncertainties.

As stated earlier, the GWP is a common metric for evaluating the strength of a compound as a greenhouse gas. Explicitly, it is the time-integrated RF per unit mass over a given time horizon relative to a reference gas. The reference gas used is CO_2, so for a given compound i, the GWP is:

$$\mathrm{GWP}(H) \;=\; \frac{\int_0^H \mathrm{RF}_i(t)\mathrm{d}t}{\int_0^H \mathrm{RF}_{CO_2}(t)\mathrm{d}t} \;=\; \frac{\mathrm{AGWP}_i(H)}{\mathrm{AGWP}_{CO_2}(H)}, \tag{2.36}$$

where H is the time horizon and AGWP is the absolute global warming potential. The AGWP can be expressed such that it depends on the RE, the lifetime/residence time in the atmosphere (τ), and time horizon [7]:

$$\mathrm{AGWP}_i(H) \;=\; \mathrm{RE}_i\tau(1 - exp(-\frac{H}{\tau})). \tag{2.37}$$

A time horizon of 100 years is used following common practice in international regulations. The AGWP of CO_2 used here is 9.17x10^{-14} W m^{-2} yr kg^{-1}, which is the currently accepted value used by the IPCC [6]. The AGWP of CO_2 is more complicated to calculate, as a pulse emission of it does not follow a simple exponential decay in the atmosphere like halocarbons do.

Hodnebrog *et al.* [7] also provide different methods to calculate GWP depending on the vertical distribution of the greenhouse gas volume mixing ratio (VMR). The Pinnock method to calculate RE assumes a well-mixed VMR; if the VMR is not well-mixed, then fractional corrections to the RE need to be made before calculating the GWP. These fractional corrections depend primarily on the atmospheric lifetime of the species and the removal process from the atmosphere. Hodnebrog *et al.* [7] derive an empirical expression for fractional correction as a function of lifetime ($f(\tau)$) based on observed differences between instantaneous RE and RE derived using a combined chemical transport and radiative transfer model for a variety of atmospheric species. If the removal process is more tropospheric (e.g., reactions with OH radicals) $f(\tau)$ will have more of an S-shape, given by:

$$f(\tau) = \frac{a\tau^b}{1 + c\tau^d}, \tag{2.38}$$

where a=2.962, b=0.9312, c=2.994, and d=0.9302. This expression is valid for lifetimes in the range: 10^{-4} yr $< \tau < 10^4$ yr. If the removal process is more stratospheric (e.g., photolysis), $f(\tau)$ valid for lifetimes in the range 10 yr $< \tau < 10^4$ yr has an exponential shape, given by:

$$f(\tau) = 1 - 0.1826\tau^{-0.3339}. \tag{2.39}$$

A plot of these two equations is shown in Figure 2.3. The uncertainty added to the RE from these corrections is estimated to be 5% for compounds with lifetimes greater than five years, and 20% for compounds with lifetimes less than five years.

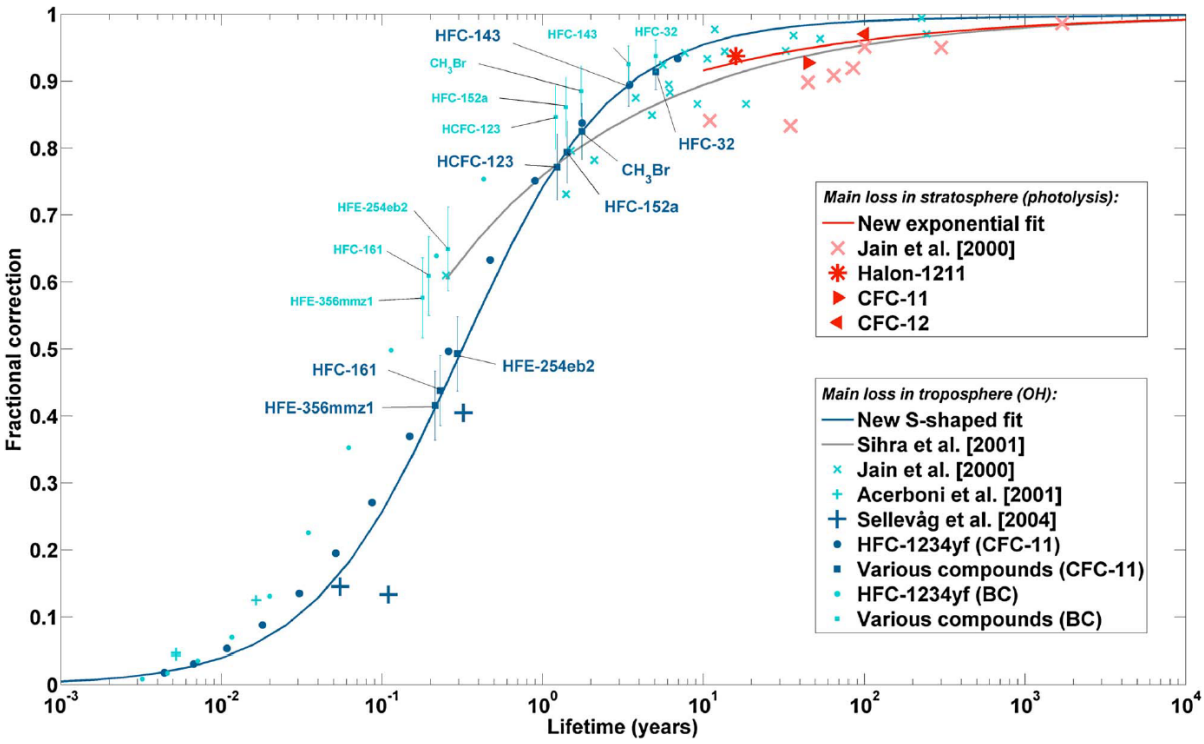

Figure 2.3: Factor needed to correct RE to account for non-uniform vertical and horizontal distribution versus atmospheric lifetime. The red symbols are for compounds whose main loss mechanism is stratospheric photolysis, while the blue symbols are for compounds which are mainly lost in the troposphere by reaction with OH. Dark blue symbols have been used in the calculation of the S-shaped fit (blue line), and dark red symbols have been used in the calculation of the exponential fit (red line). Light blue and light red symbols are shown for comparison. Image taken from [7].

Another correction factor to the RE is known as the stratospheric temperature adjustment. Due to strong absorption in the atmospheric window, halocarbons tend to warm the stratosphere as a result of the increased absorption of IR in the atmospheric window, resulting in an increase of downwards radiation in order to achieve a new equilibrium state. The end result of this is that the instantaneous forcing underestimates the climate impact. To account for this, Hodnebrog *et al.* recommend that the RE be adjusted by increasing it by 10% before using it to derive the GWP. This 10% increase is from studies into the differences between instantaneous and stratospheric-temperature adjusted RE values [7]. In this work REs are reported as instantaneous REs, however the GWP values are calculated using adjusted REs. The uncertainty associated with the stratospheric temperature adjustment is 4%. Sources of uncertainty on GWP values are from RE, the lifetime, and the AGWP of CO_2. The AGWP of CO_2 has an uncertainty of 26% for a time horizon of 100 years; and the uncertainties on lifetimes of halocarbons removed in the troposphere are estimated to be approximately 20%. For species removed in the stratosphere via photolysis, their long lifetimes make the GWP_{100} insensitive to lifetime compared to other sources of error.

Chapter 3

Experimental Methods

This chapter describes the experimental apparatus and procedures used to collect data.

3.1 Experimental Apparatus

A diagram of the experimental apparatus used this work is shown in Figure 3.1. The spectrometer is a Bomem DA8.002 FTS. The maximum optical path difference is 250 cm; by resolution criterion $1/L$, this leads to a maximum resolution of 0.004 cm^{-1}. The spectral range is determined by the combination of source, beamsplitter, and detector used. The source can be either globar (IR) or quartz-halogen (visible). The beamsplitter can be potassium bromide (KBr, 450-4000 cm^{-1}) or calcium flouride (CaF_2, 1200-8500 cm^{-1}). The detector is either mercury cadmium telluride (MCT, 500-5000 cm^{-1}) or indium antimonide (InSb, 1800-11000 cm^{-1}). The IR absorption spectra described in this thesis were obtained using the globar source, KBr beamsplitter, and MCT detector. The MCT detector operates using the photovoltaic effect; when illuminated with light of sufficient energy, an electron is excited from the valance band to the conduction band, resulting in a change in electric potential that leads to an electric signal that can be detected. The MCT detector has a non-linear response between measured signal and photon flux. For high intensities, corrections for this need to be done before phase corrections and Fourier transform [39]. Alternatively, if the intensity is kept low, the non-linear effects are minimal and can be ignored.

There exist other sources of error from the spectrometer that need to be accounted for [40]. The first is back scattering from the surface of the aperture back into the source. This results in double modulation of a small component of the light, which shows up as an additional signal in the spectrum at twice the frequency of the initial beam. This effect is removed by coating the back side of the aperture to reduce reflectivity or by making

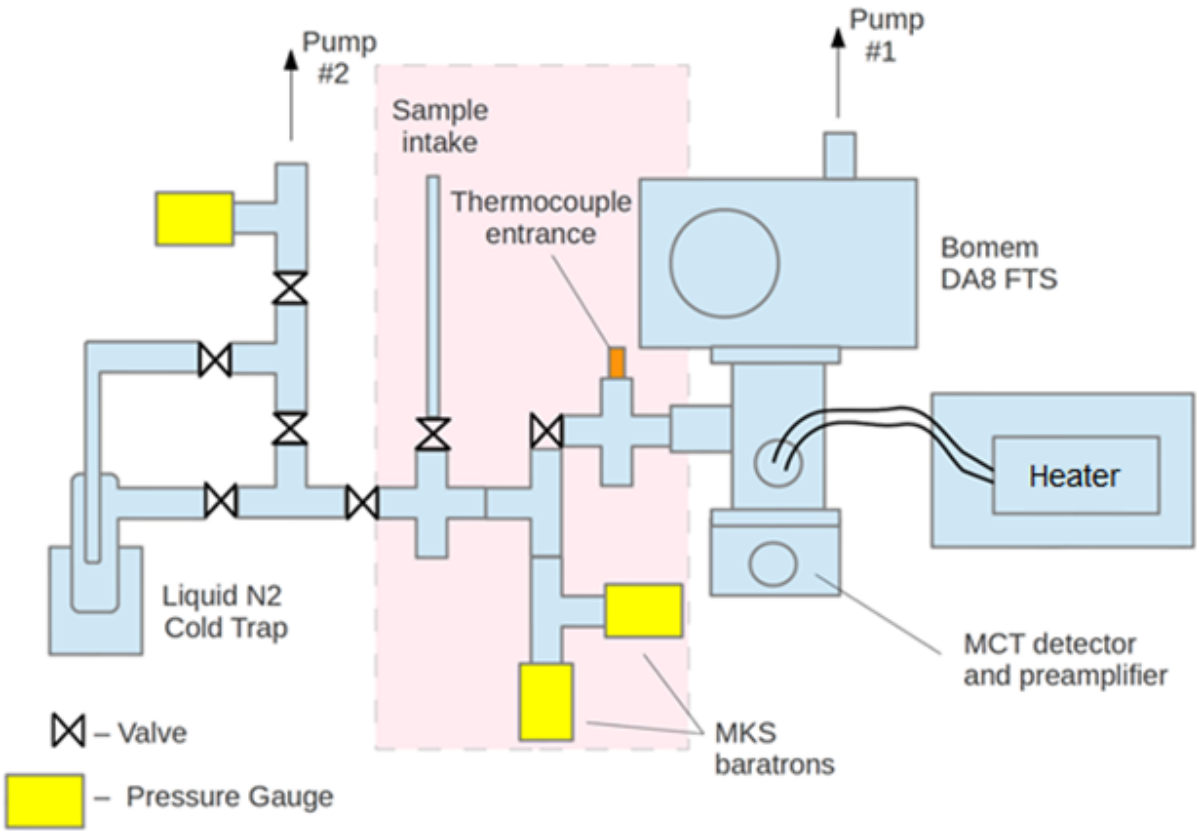

Figure 3.1: Schematic diagram of the experimental set-up. Diagram is not to scale.

the back side conical so reflections don't travel back into the system. The second error is that heating of the aperture can cause a thermal distribution that alters the spectrum. The detector ends up seeing the light source through the aperture, along with an outer warm annulus from the aperture itself. The smaller the aperture, the greater the effect. A simple mitigation to this distortion is to add a second aperture after the interferometer [40]. This way the thermal contamination from the first aperture can be reduced by an order of magnitude by the second aperture and the heating of the second aperture is seen by the detector without modulation, and hence is discarded in the Fourier transform. Both apertures in the system were set to 3.5 mm diameter, which limits the amount of light reaching the detector in order to avoid non-linear effects, but still allows enough for good signal-to-noise ratio. A resolution of 0.1 cm^{-1} was chosen as it was the same resolution or better than previous studies into the molecules of interest. Furthermore, it achieves a balance between experimental run time and level of resolution.

Spectra were recorded from 530 to 3400 cm^{-1}. This spectral range was determined by the experimental limitation of the MCT detector and KBr beamsplitter combination. Each measurement run consisted of 400 to 500 co-added spectra. The gas cell used was 10.0±0.1 cm long stainless-steel with one inlet. A coolable cell was intended to be used, but unfortunately suffered a leak when the coolant line was welded to it.

Before allowing the sample into the cell, it was subjected to multiple freeze-pump-thaw cycles to remove possible residual ambient air, including water vapour, from the sample flask. A freeze-pump-thaw cycle consists of using liquid nitrogen to freeze the sample, then while the sample is frozen, pumping out the air from the flask and sealing the flask again. The sample can then be thawed and some impurities will outgas from the sample. This process is repeated at least 2 to 3 times. The cell was evacuated using a Varian 250 turbo pump. The gas sample was allowed to diffuse into the heatable cell in order to reach the desired pressures. Temperature control was provided by electric heating bands attached to a voltage control. The temperature was measured by an in-line thermocouple located at the centre inside wall of the cell. Wedged ZnSe windows with Buna-N o-rings were used to seal the ends of the cell.

The pressure in the gas cell was measured using a 10 Torr MKS baratron pressure gauge. The cell's leak rate was approximately 0.03 Torr/hr. This pressure change did not significantly alter the spectrum during a co-added spectra measurement run, which takes approximately two hours. At each temperature, measurements were made at 7-10 different pressures in the range of 0.1-10.0 Torr to avoid saturated signal absorption. The pressure and temperature sensor calibration was done by performing an N_2O spectral line test of the system and by attaching a second baratron to the system in order to confirm

the accuracy of the first baratron. An N_2O spectral line test is done by filling the cell with N_2O, and looking at the position of a well known line to confirm the spectrometer's line position accuracy. The line at 2200.74692 cm^{-1} was measured at 2200.74663 cm^{-1}, a shift of 0.00029 cm^{-1}, which is within the 0.004 cm^{-1} resolution tolerance; thus no calibrations were made to position. From the fitting the line parameters of the N_2O, the temperature of the gas can be retrieved, which agreed within error with the thermocouple reading. Additional temperature calibration was achieved by setting the zero of thermocouple using an ice-water bath.

Fluctuations in the lab temperature and ambient air can also affect the measurements. To minimize these effects, the cell was enclosed in a vacuum jacket to isolate it from the environment; this second chamber was evacuated with a rotary pump to a pressure of approximately 2.7 Torr. A yoke mount for the inner cell was designed to support the inner cell in the centre of the outer jacket and is shown in Figure 3.2. Two yokes are used to support the cell, one at each end. The mounted short-cell with heating band is shown in Figure 3.3. Empty cell scans were performed between filled cell runs to monitor baseline stability (i.e. alternating filled and empty cell runs).

3.2 Data Analysis

3.2.1 Cross-Section Calculation

The before and after empty cell runs were averaged to obtain a baseline for the filled cell measurements. Figure 3.4 shows an example of the spectra obtained after performing a Fourier transform on the detector signal. These spectra have been vertically offset to match the true saturation value of the detector, which is taken to be the average value found in the range of 280-440 cm^{-1}. This value is then subtracted from the spectra so that the saturation intensity value is zero, as shown in Figure 3.4.

The next processing step was to account for fluctuations in globar intensity. Under ideal circumstances, locations of known zero absorption locations should be of equal intensity for filled and empty cell scans, but due to fluctuations in globar intensity, differences arise. These fluctuations can result in an over/under estimation of the strength of the absorption. Typical fluctuations can be seen in Figure 3.5. To account for this effect, a polynomial was fitted to the difference between the filled cell and the empty cell in zero absorption regions, as shown in Figure 3.5. This polynomial was used to adjust the intensity of the empty cell spectra, such that the filled and empty cell spectra would be of equal intensity in regions of known zero absorption, and extrapolates an adjustment

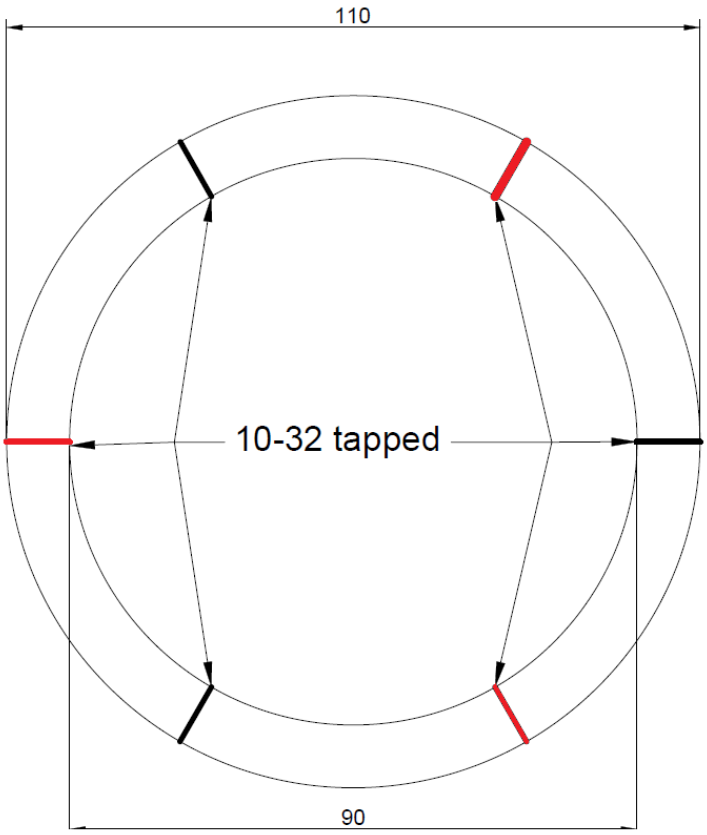

Figure 3.2: Design of the yoke mount for the inner cell. Three of the screws face inwards to support the cell (marked in red), while the remaining three face outwards (marked in black) to hold in yoke in place against the outer jacket. The yoke is made of Teflon and the screws holding the cell in place have Teflon caps to reduce thermal energy transfer from the outer wall to the cell. Units are in mm and 10-32 refers to the screw size of the holes.

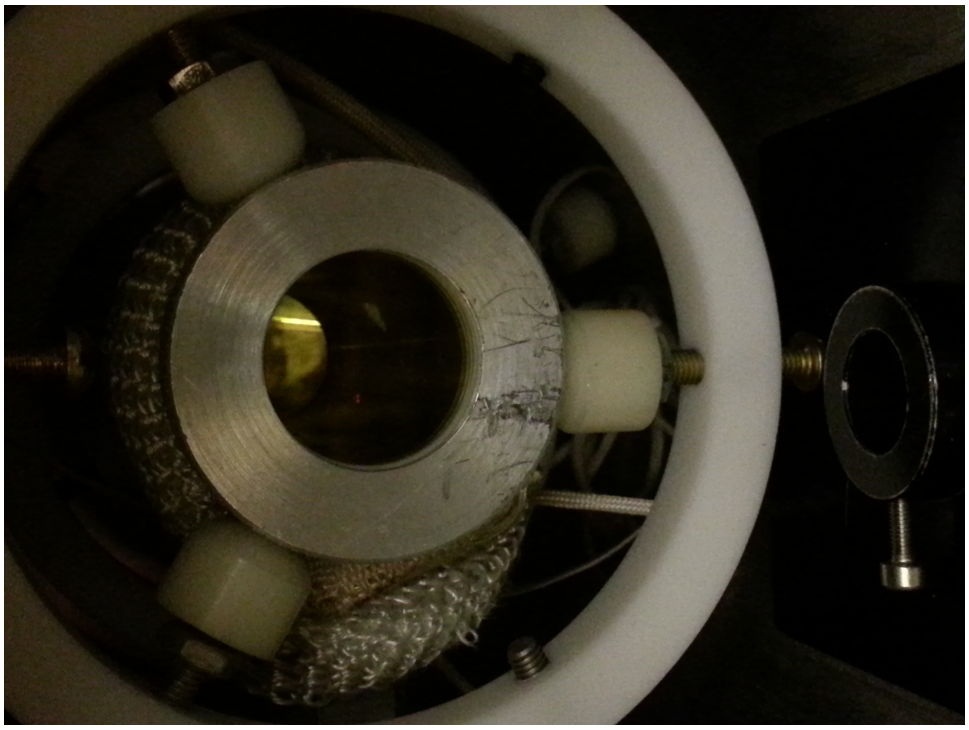

Figure 3.3: Short-cell mounted inside the outer jacket. The heating band can be seen wrapped around the cell.

in regions of absorption. This correction did not have a major impact for most of the spectra, but was vital to regions of low absorption. An example of this adjustment is shown in Figures 3.6 and 3.7.

Next, the ratio of filled cell spectrum to empty cell spectrum was taken to obtain the optical depth ($\chi(\tilde{\nu})$) using Equation 2.1. Using Equation 2.2, the cross-section can be found for a given pressure. Previous publications using the same set-up describe the error analysis [41, 42, 43, 44, 45]. Following those papers, sources of error include temperature fluctuations ($\pm$0.2 K), pressure readout ($\pm$0.015 Torr), and path length ($\pm$1 mm). These errors are propagated in the calculation of the optical depth to determine its uncertainty. The uncertainty of the optical depth is used to assign weights in the linear fit against pressure to find the zero-Torr absorption cross-section. The remaining sources of error due to the non-linearity of the MCT detector, baseline drift, data reduction, and instrument noise can be accounted for in the linear fit. Only points with an optical depth between 0.0 and 2.0 are processed. This selection avoids non-physical (negative absorption) and non-linear detector effects. An example of a linear fit of optical depth is shown in Figure 3.8. The final uncertainty is the sum, in quadrature, of the linear fit error and sample purity error ($\pm$2.0%), chosen at the 99.7% confidence limit (3σ).

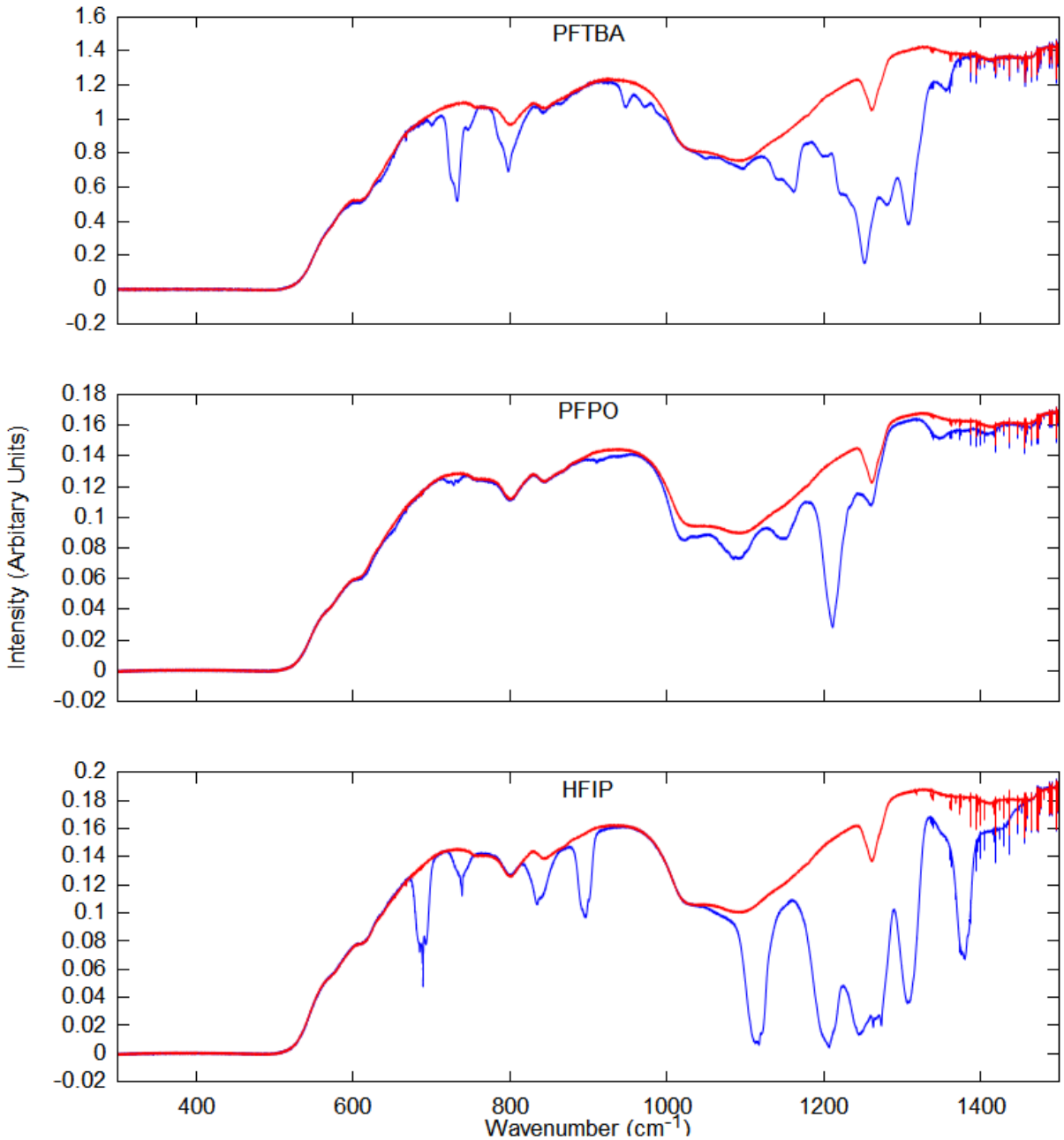

Figure 3.4: Examples of filled (blue) and averaged (before and after) empty cell (red) spectra for PFTBA, PFPO, and HFIP. Water vapour absorption lines can be seen beyond 1400 cm^{-1} due to a small leak in the system.

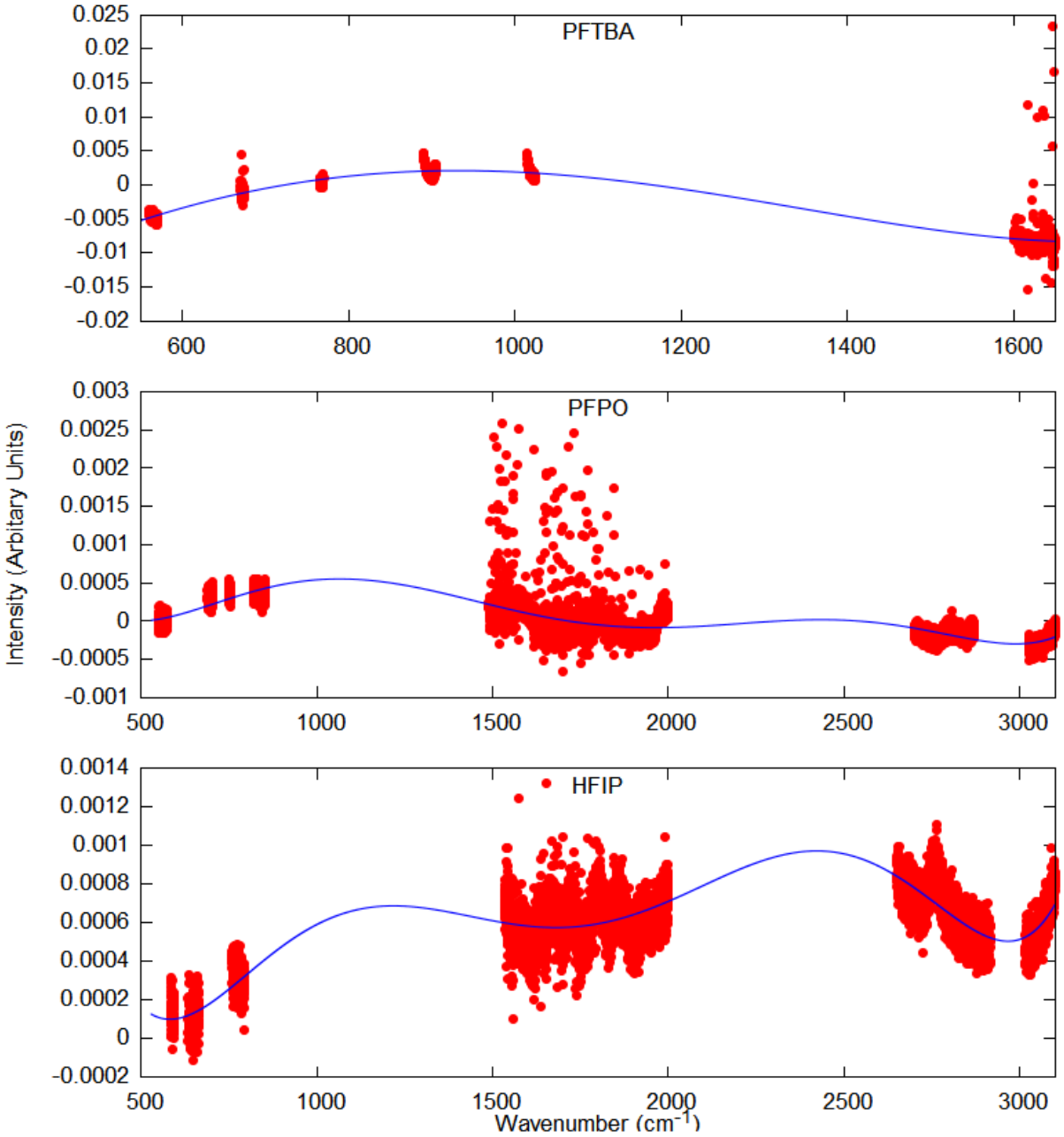

Figure 3.5: Red points are the difference between filled and averaged empty cell spectra at locations of known zero absorption. The blue line is a polynomial fit. Examples shown are for PFTBA, PFPO, and HFIP.

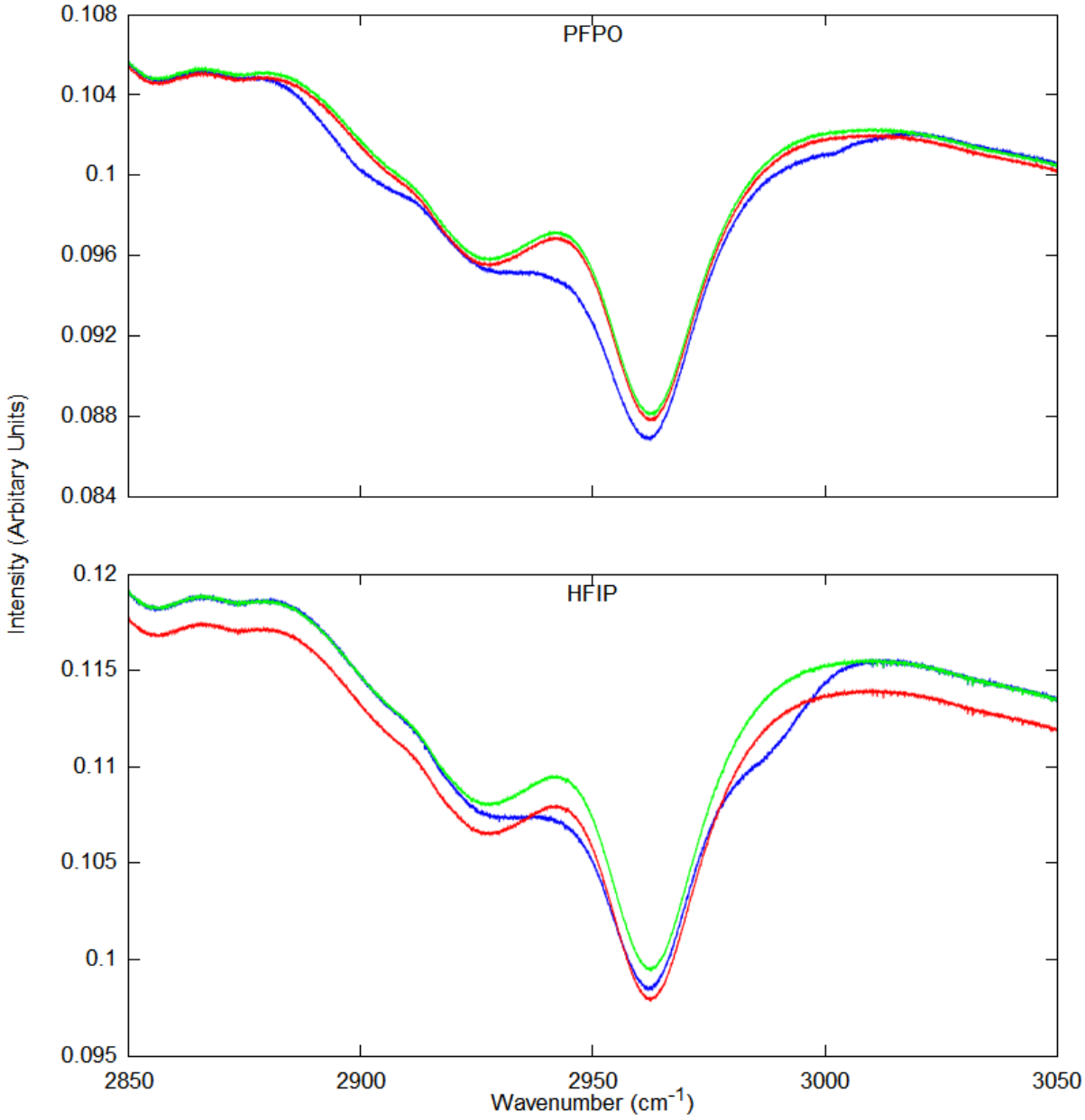

Figure 3.6: Examples of filled cell (blue) and averaged empty cells spectra before (red) and after (green) baseline polynomial adjustment for PFPO and HFIP.

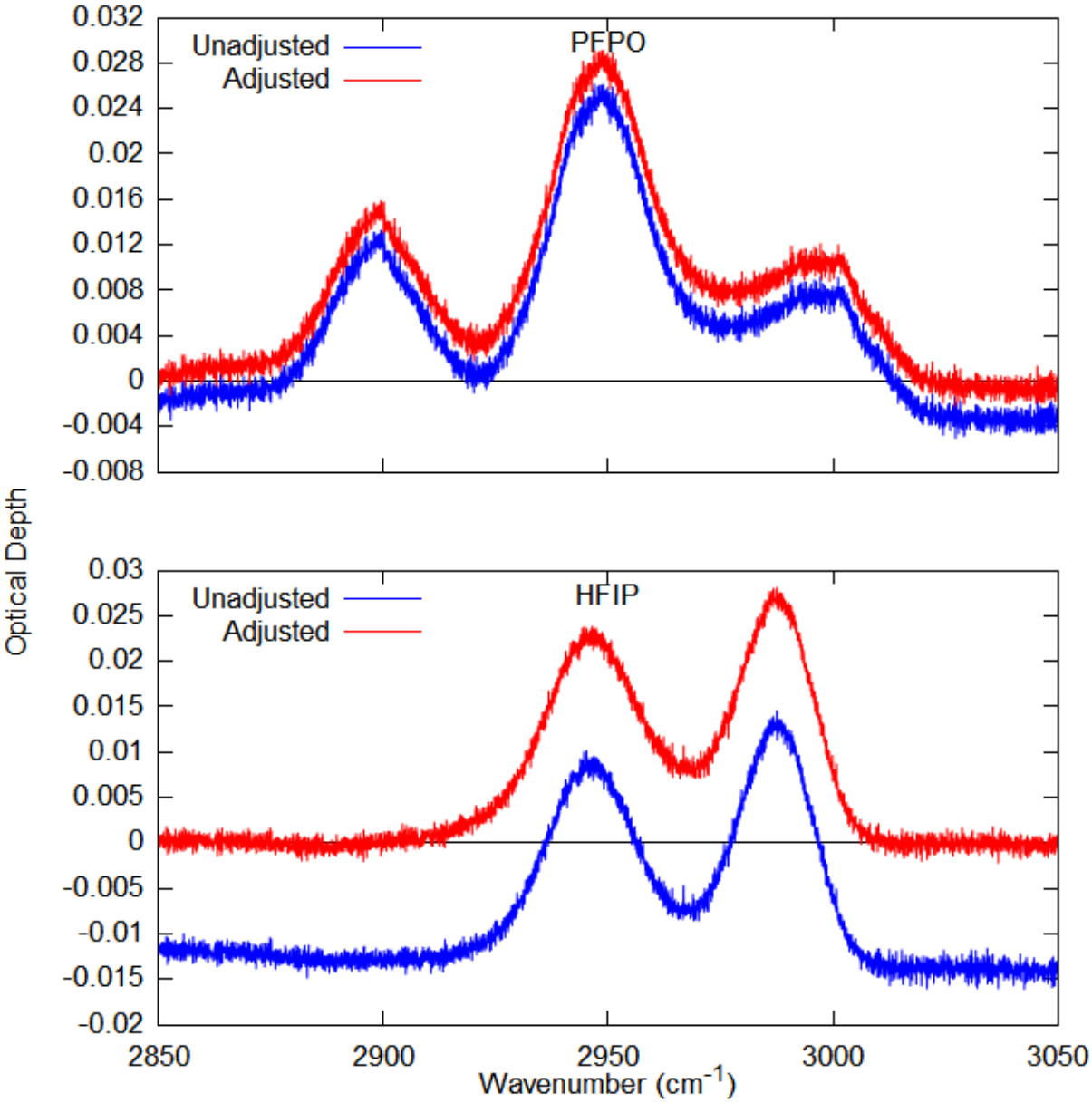

Figure 3.7: Examples of optical depth with (red) and without (blue) polynomial adjustment for PFPO and HFIP.

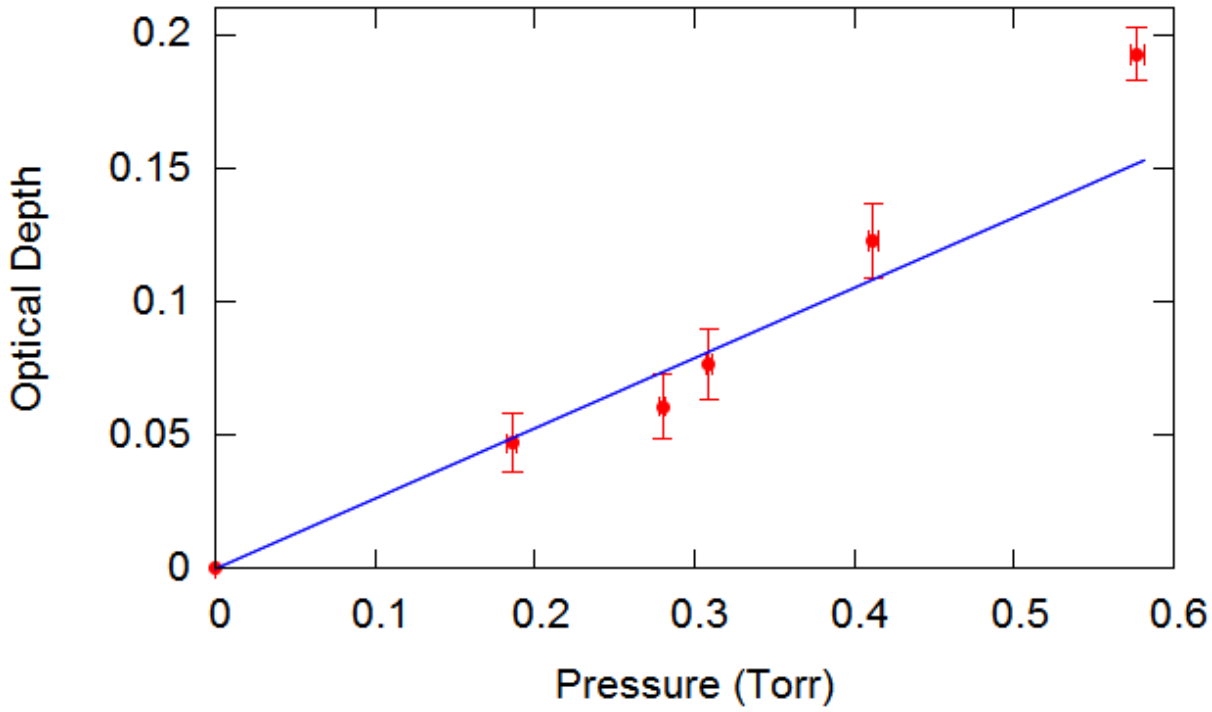

Figure 3.8: Plot showing linear fit of optical depth against pressure for PFTBA at 303.5 K and 1273.2 cm^{-1} with a forced convergence at the origin. Errorbars are from propagation of the uncertainties of temperature, pressure, and pathlength in the calculation of optical depth.

3.2.2 DFT Scaling

Through direct comparison of cross-sections, the relationship between theory and experimental band positions can be evaluated. The DFT calculation only provides the centre location of a vibrational band and the band strength. A theoretical spectrum is produced by approximating each fundamental vibrational band of overlapping rotational lines as a Gaussian function with a width of 8.5 cm^{-1}. Closely spaced fundamental modes can be difficult to resolve in the experimental spectra as the bands overlap. For such cases, the DFT band that most closely matches the location of the centre of the experimental band is chosen to express the theoretical location of that band. The relationship between experimental and DFT band locations can be fitted to a linear function. The uncertainty of the parameters for the linear fits are those found by linear least-squares method and are reported at one standard deviation. Linear relationships between experimental and DFT band positions have been reported by other groups [8, 9, 10, 52]. The derived linear relation is applied to the DFT spectrum to adjust positions of peaks outside of the experimental spectral range for which there are no experimental data, resulting in a scaled DFT spectrum. From this analysis, a DFT spectrum is produced that closely matches the experimental spectrum in the observed range and can be used to better predict the spectrum outside of this range.

3.2.3 Integrated Band Strength and Centroid Shift Calculation

As explained in Section 2.3, for large molecules it is difficult to resolve individual rotation-vibration lines and extract line parameters; instead absorption cross-sections and integrated band strengths are reported. Trapezoidal numerical integration is used to derive the latter, approximating an integral as follows:

$$\int_a^b f(x)dx \approx \frac{b-a}{2N}\sum_{n=1}^{N}(f(x_n)+f(x_{n+1})) \tag{3.1}$$

$$= \frac{b-a}{2N}\left[f(x_1)+2f(x_2)+\cdots+2f(x_N)+f(x_{N+1})\right], \tag{3.2}$$

where a and b are the limits of integration, N is the number of data points, and the spacing between points is assumed to be constant value of $(b-a)/N$. From error propagation, this method yields an uncertainty given by:

$$Error = \frac{b-a}{N}\sqrt{\sum_{n=1}^{N}\Delta f(x_n)^2}. \tag{3.3}$$

Additionally there is an added uncertainty in trapezoidal numerical integration, from over/underestimation due to curvature, which is given by:

$$Error = -\frac{(b-a)^3}{12N^2}f''(\xi), \tag{3.4}$$

where $f''(\xi)$ is the maximum second order derivative in the range of integration [48]. $f''(\xi)$ is estimated by calculating the differences of the differences between cross-section data points. The final uncertainty on integrated band strength is the sum, in quadrature, of the uncertainty given in Equations 3.3 and 3.4 at the 99.7% confidence interval.

Centroid shifts are also calculated as they can indicate the presence of hot bands arising in the cross-section with varying temperature. The centroid is defined as the cross-section intensity-weighted average wavenumber of the band:

$$Centroid\ = \frac{\int_{\tilde{\nu}_1}^{\tilde{\nu}_2}\tilde{\nu}\sigma(\tilde{\nu})d\tilde{\nu}}{\int_{\tilde{\nu}_1}^{\tilde{\nu}_2}\sigma(\tilde{\nu})d\tilde{\nu}}. \tag{3.5}$$

The uncertainty analysis is similar to that for the integrated band strengths.

3.2.4 RE and GWP Derivation

In order to use the Pinnock method to calculate the RE, the experimental and DFT spectra are first averaged over 1 cm^{-1} bins, so that the resolution of the spectra now matches the resolution of the Pinnock's curve. Each bin is multiplied by the Pinnock's curve at the corresponding wavenumber and the final result is integrated over the range of the Pinnock curve, which is 0-3000 cm^{-1}. The result of this is the instantaneous RE.

As explained in Section 2.6, before the instantaneous RE can be used to derive the GWP, it must first be adjusted to correct for stratospheric heating and VMR distribution. All REs calculated are subjected to a 10% increase due to the stratospheric temperature adjustment. Depending to the primary sinks of the species in the atmosphere, either the exponential or S-shaped fractional lifetime is also applied to the RE. This corrected RE is used in Equation 2.37 to derive the GWP of the species.

Chapter 4

Perfluorotributylamine

4.1 Introduction

This chapter summarizes the results of temperature-dependent absorption cross-section measurements of perfluorotributylamine (PFTBA), which have also been published as: Godin *et al.*, Temperature-dependent absorption cross-sections of perfluorotributylamine, *J. Mol. Spec.*, 2015 [46]. PFTBA is a fully-fluorinated liquid, with the molecular structure shown in Figure 4.1. In this chapter, the first known temperature-dependent measurements of PFTBA are presented; these measurements are compared to theoretical DFT calculations and the previously published data. Additionally, the RE and GWP for PFTBA are calculated.

The PFTBA sample was a commercial product from Sigma-Aldrich (certified 99±0.5% pure). Temperatures in the range of 298-344 K were studied. At each temperature, measurements were made at 7-10 different pressures in the range of 0.1-1.1 Torr.

4.2 Absorption Cross-Sections

Measured absorption cross-sections as a function of temperature are shown in Figure 4.2. Note that these were derived as described in Section 3.2.1. The vertical black lines indicate the regions used to calculate the integrated absorption band strengths: 570-675, 675-770, 770-900, 900-1025, and 1025-1500 cm^{-1}. The integrated band strengths are described in detail in Section 4.4.

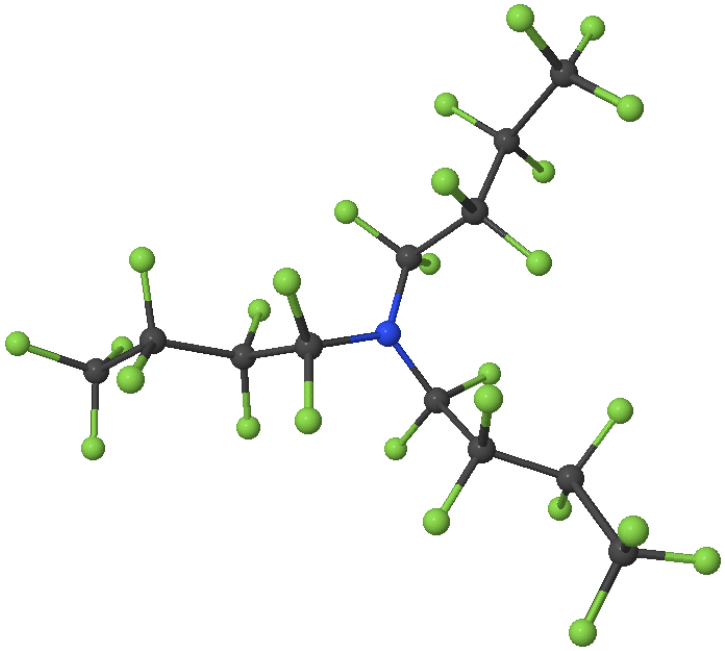

Figure 4.1: Projection image of PFTBA. The blue atom is nitrogen, the green atoms are fluorine, and the grey atoms are carbon.

4.3 Density Functional Theory

The ground state geometry and vibrational frequencies of PFTBA were determined using the 6-311+G(*2d,p*) basis set and B3LYP functionals with a resolution of 0.679 cm^{-1}. Higher levels of theory and/or including anharmonic couplings failed to converge. As this calculation is for the vibrational ground state, other spectral features, such as hot bands or combination bands, can be present in the experimental spectra but not in the DFT result. Due to the presence of internal rotors, PFTBA could have multiple different ground state configurations. However, given the high number of internal rotors, a coordinate scan to find all stable configurations was impossible to do within reasonable computation time. Bravo *et al.* [9] found that for linear perfluoroalkanes, the difference in RE calculated from including all conformers versus just one conformer was less than 1%. Thus, it is assumed that the configuration found is representative of other possible configurations and that each configuration will have a similar electronic energy and theoretical spectra.

From visual inspection, peaks in the experimental and theoretical spectra are identified, to evaluate how well the theory determines the position of each transition. These results are shown in Table 4.1 and plotted in Figure 4.3. The results of this comparison are fit to a linear function in order to scale the positions of bands outside of the ex-

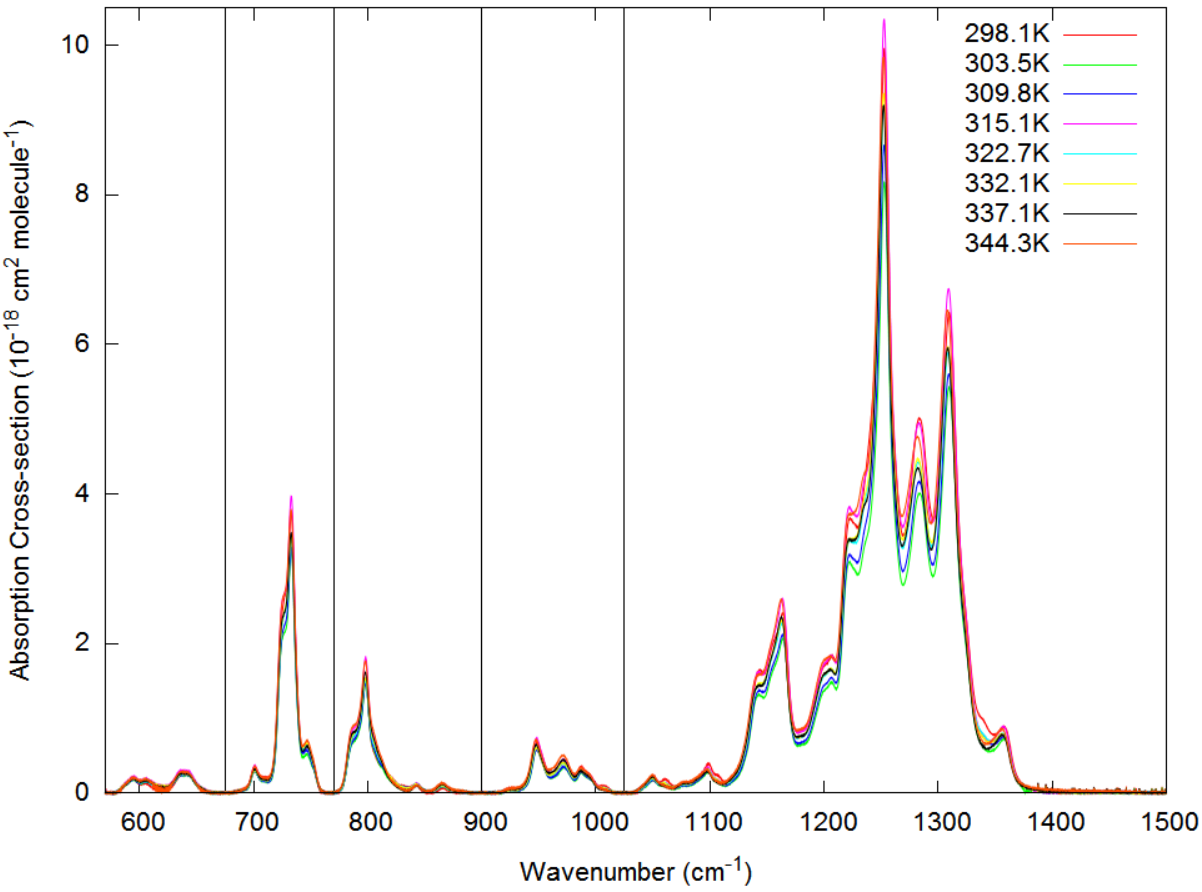

Figure 4.2: Experimental cross-sections of PFTBA. The absorption bands are identified by the vertical black lines. Bands are defined from 570-675, 675-770, 770-900, 900-1025, and 1025-1500 cm^{-1}.

perimental range or modes that could not be resolved well enough in the experimental spectra to give an assignment. The linear relation between experiment and DFT is shown in Figure 4.3. The linear expression is: $\tilde{\nu}_{Exp} = 1.01 * \tilde{\nu}_{DFT} - 2.44$ cm^{-1}. The final result of this scaling is shown in Figure 4.4. Significant improvement in the simulated spectra is seen after adjusting the position of the bands based on the experimental spectra.

Table 4.1: Summary of unadjusted band positions and strength for PFTBA from DFT calculations, along with experimental band locations.

Mode	**DFT (cm^{-1})**	**Experimental (cm^{-1})**	**Band Strength (km/Mole)**
1	16.8		0.002
2	18.2		0.002
3	23.0		0.012
4	24.5		0.001
5	29.2		0.012
6	31.5		0.008
7	43.2		0.002
8	49.0		0.030
9	62.3		0.012
10	64.2		0.033
11	70.9		0.050
12	74.5		0.025
13	83.1		0.023
14	101.0		0.015
15	113.1		0.083
16	124.7		0.032
17	139.2		0.503
18	146.9		0.188
19	168.0		0.386
20	185.3		0.052
21	191.7		0.382
22	201.6		4.088
23	211.9		2.059
24	212.7		1.863
25	226.1		0.083

Mode	**DFT (cm^{-1})**	**Experimental (cm^{-1})**	**Band Strength (km/Mole)**
26	229.8		0.450
27	236.4		0.077
28	241.7		0.036
29	245.1		0.105
30	250.0		0.066
31	266.3		0.321
32	281.9		0.940
33	287.2		5.102
34	288.3		2.951
35	291.5		0.859
36	296.5		4.073
37	308.5		2.035
38	314.8		0.399
39	318.4		0.427
40	327.4		0.229
41	330.4		0.254
42	348.4		2.074
43	356.2		1.506
44	362.4		0.078
45	367.3		0.063
46	368.7		0.603
47	371.4		0.169
48	375.5		0.484
49	380.9		0.588
50	385.9		0.067
51	393.6		0.142
52	424.3		9.964
53	458.5		0.354
54	460.8		0.474
55	480.6		8.995
56	522.6		13.481
57	525.3		3.850
58	526.9		10.713

Mode	DFT (cm^{-1})	Experimental (cm^{-1})	Band Strength (km/Mole)
59	532.6		2.433
60	540.3		0.685
61	547.6		1.641
62	578.7	586.5	3.800
63	581.8	587	1.186
64	587.8	593.5	27.417
65	595.2	600	5.038
66	599.2	605.5	11.162
67	600.9	608	3.599
68	625.4	634.7	49.822
69	638.4	644.2	23.850
70	647.6	653	1.402
71	694.2	700.9	32.933
72	703.4	706	3.834
73	704.4	713	5.665
74	716.2	728	154.614
75	726.6	733.1	255.440
76	736.1	746.5	7.730
77	773.4	786	52.313
78	791.5	798.2	201.847
79	835.7	842.7	26.222
80	940.2	948.3	48.633
81	947.6	972.6	62.584
82	1058.0	1007.8	2.207
83	1087.3	1049.4	19.901
84	1092.8	1060	13.976
85	1107.7	1098	29.762
86	1114.3	1103	5.957
87	1117.0	1108	19.245
88	1133.5	1127	45.880
89	1136.5	1124	8.664
90	1147.9	1150	320.334
91	1159.5	1154	47.713

Mode	DFT (cm^{-1})	Experimental (cm^{-1})	Band Strength (km/Mole)
92	1162.4	1156	35.795
93	1167.2		32.554
94	1169.8		36.880
95	1171.8		57.924
96	1178.3		31.338
97	1179.1		8.347
98	1185.3	1200	241.617
99	1189.1	1222.5	479.081
100	1196.5		65.636
101	1208.5	1245	120.209
102	1212.2	1247	166.718
103	1217.7	1250	196.207
104	1220.0	1253	176.147
105	1220.1	1255	590.049
106	1231.3		147.026
107	1258.2	1277	315.664
108	1270.1		53.561
109	1276.0	1287	338.660
110	1283.0	1307	478.979
111	1290.2	1312	535.660
112	1328.4	1340	90.078
113	1338.9	1355	27.366
114	1340.6	1360	15.075

4.4 Integrated Band Strengths and Centroid Shifts

Integrated band strengths are reported in Table 4.2. Within the error bars, good agreement was seen with previously published data [13]. It should be noted that the initial purity of the sample used in the previously published data is unknown. Furthermore, when calculating the integrated band intensities, a discrepancy was noticed between their published value for total integrated band strength and the value calculated in this work using their raw data file; instead of a value of $7.08 \text{x} 10^{-16}$ cm/molecule, a value of

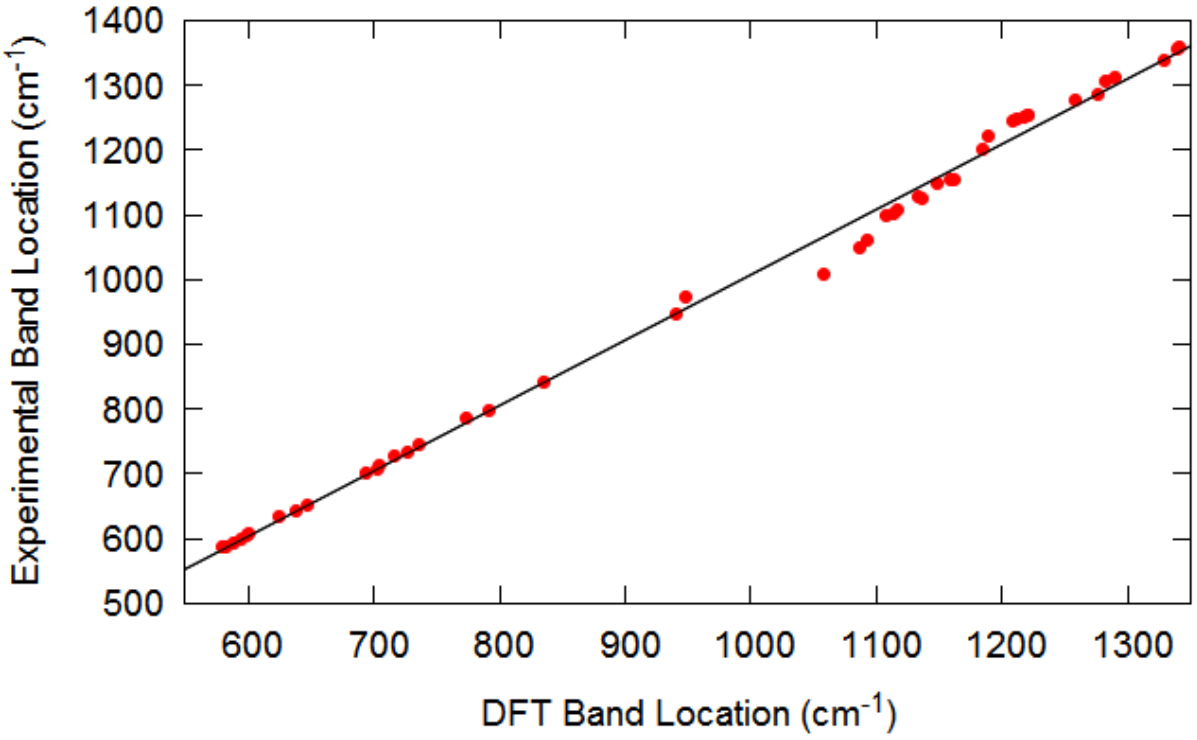

Figure 4.3: Theoretical absorption band location versus experimental band location. Fitted line has slope of 1.01 and intercept of -2.44 cm^{-1}.

8.51x10^{-16} cm/molecule was obtained. For consistency in this work, the values of integrated band strength used are calculated directly from the supplementary data files in [13].

The regions used to calculate the integrated absorption band strengths are: 570-675, 675-770, 770-900, 900-1025, and 1025-1500 cm^{-1}. The overall integrated band strength is defined for the range 570-1500 cm^{-1}. The integrated band strengths as a function of temperature are shown in Figure 4.5. The overall (570-1500 cm^{-1}) integrated band strength shows no significant change with temperature, and neither do the integrated band strengths for any of the individual bands. The integrated band strengths are also reported in Table 4.2 along with values from Hong *et al.* [13] and the DFT calculation. DFT calculations provide integrated absorption cross-sections for each vibrational mode, so the intensity values for each vibrational mode can be simply summed up in a given region and compared to the experimental result. Overall, the DFT calculated integrated band strengths overestimate the experimental results. The exception is the 900-1025 cm^{-1} band, for which the DFT underestimates the experimental result. The experimental band strengths agree with the results from Hong *et al.* [13] for most of the bands. The exceptions are the 770-900 and 900-1025 cm $^{-1}$ bands; here Hong *et al.* [13] results are higher

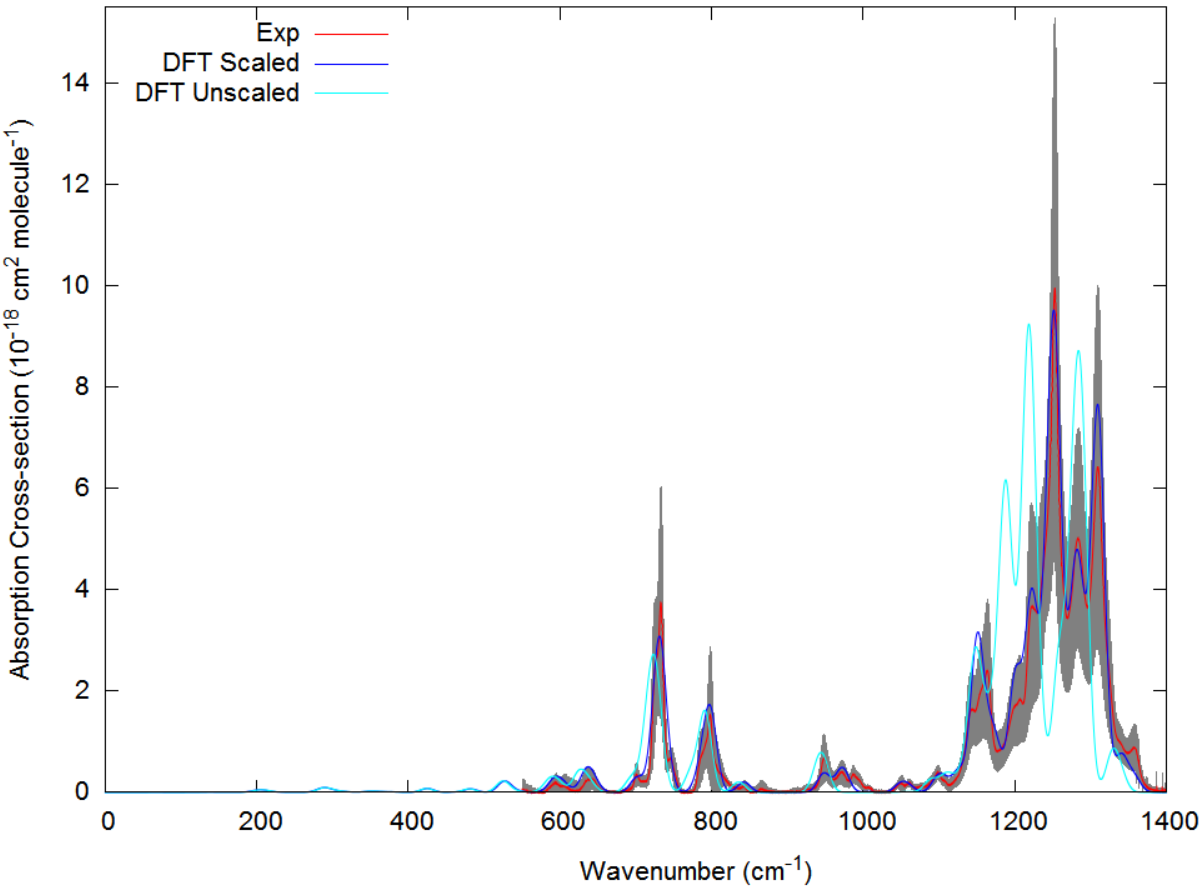

Figure 4.4: Simulated and experimental absorption cross-sections of PFTBA. The experimental cross-section was recorded at 298.1 K. Grey shading indicates the uncertainty of the experimental spectrum.

Table 4.2: Integrated band strengths of PFTBA at different temperatures.

Temperature (K)	**Integrated Band Strengths (10^{-17} cm molecule^{-1})**					
	Overall (570-1500 cm^{-1})	570-675 cm^{-1}	675-770 cm^{-1}	770-900 cm^{-1}	900-1025 cm^{-1}	1025-1500 cm^{-1}
296.0±0.5[13]*	85.1±4.3	1.46±0.07	6.82±0.34	4.14±0.21	2.79±0.14	69.8±3.5
DFT	95.21	2.114	7.642	4.656	1.883	78.91
298.2±0.16	85.1±3.4	0.98±0.21	6.54±0.32	3.21±0.19	2.39±0.21	71.9±2.1
303.5±0.08	71.4±2.5	1.09±0.13	5.65±0.31	3.44±0.12	1.95±0.09	59.6±1.8
309.8±0.11	71.9±1.6	1.08±0.17	5.60±0.13	3.17±0.15	1.89±0.10	60.2±0.8
315.1±0.13	85.8±2.2	1.30±0.13	6.75±0.05	3.55±0.10	2.38±0.17	71.6±1.2
322.7±0.18	77.4±3.6	1.10±0.41	5.99±0.15	3.35±0.12	2.11±0.15	64.8±1.1
332.1±0.22	78.6±2.5	1.17±0.10	6.12±0.07	3.49±0.10	2.12±0.07	65.7±1.3
337.1±0.06	77.6±4.0	1.13±0.46	6.14±0.17	3.51±0.14	2.24±0.07	64.6±1.7
344.1±0.29	97.1±5.0	1.29±0.56	7.70±0.23	3.59±0.17	2.88±0.13	80.8±1.4
Average	77.50±0.92	1.158±0.058	6.091±0.071	3.442±0.045	2.151±0.036	65.31±0.49

*Calculated in this work using cross-section from [13].

than new results. For the overall (570-1500 cm^{-1}) integrated band strength, there is agreement between these results and [13].

As shown in Figure 4.6, no significant trend is seen in the position of the centroid as a function of temperature for any of the bands, indicating that temperature has no significant impact on the absorption cross-sections of PFTBA in the range studied.

4.5 Radiative Efficiencies and Global Warming Potentials

An instantaneous RE for PFTBA of 0.782±0.156 Wm^{-2}ppbv^{-1} was calculated from the experimental data for 550-3000 cm^{-1}, which agrees within error with previously published data by Hong *et al.* of 0.86 Wm^{-2}ppbv^{-1} for a range of 600-1500 cm^{-1} [13]. For the DFT calculation, an instantaneous RE of 0.9275 Wm^{-2}ppbv^{-1} was calculated, which is due to an overestimation in intensity of the band strengths. Using the scaled DFT spectra, we can estimate the RE in the region below 550 cm^{-1}; here the DFT calculation finds an RE of 0.021 Wm^{-2}ppbv^{-1}, yielding a total instantaneous RE of 0.803 Wm^{-2}ppbv^{-1} for 0-3000 cm^{-1} when combined with the experimental result.

There are no known lifetime measurements of PFTBA. However it lacks the functional groups that react with OH radicals, thus it is suspected that PFTBA is long lived in the atmosphere and is ultimately removed via photolysis in the stratosphere [13]. Hong *et al.*

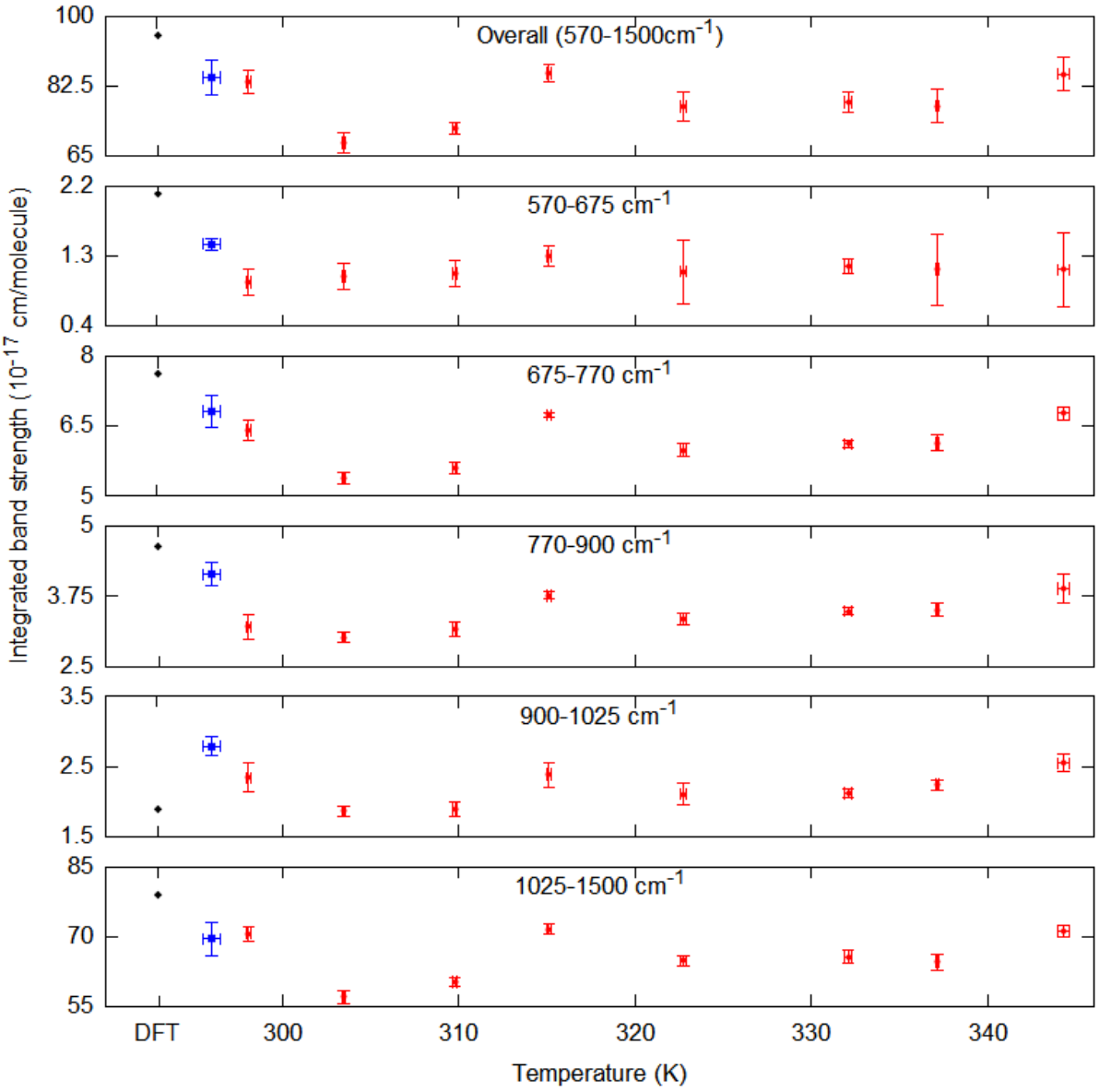

Figure 4.5: Integrated band strengths for PFTBA at different temperatures. Red circles are from this work and the blue squares are the previously published data from [13] calculated using our method. The horizontal errorbars indicate the standard deviation from all measurements taken at that temperature; whereas the vertical errorbars indicate the uncertainty in integrated band strength from Section 3.2.3. The black diamonds are from the DFT calculation.

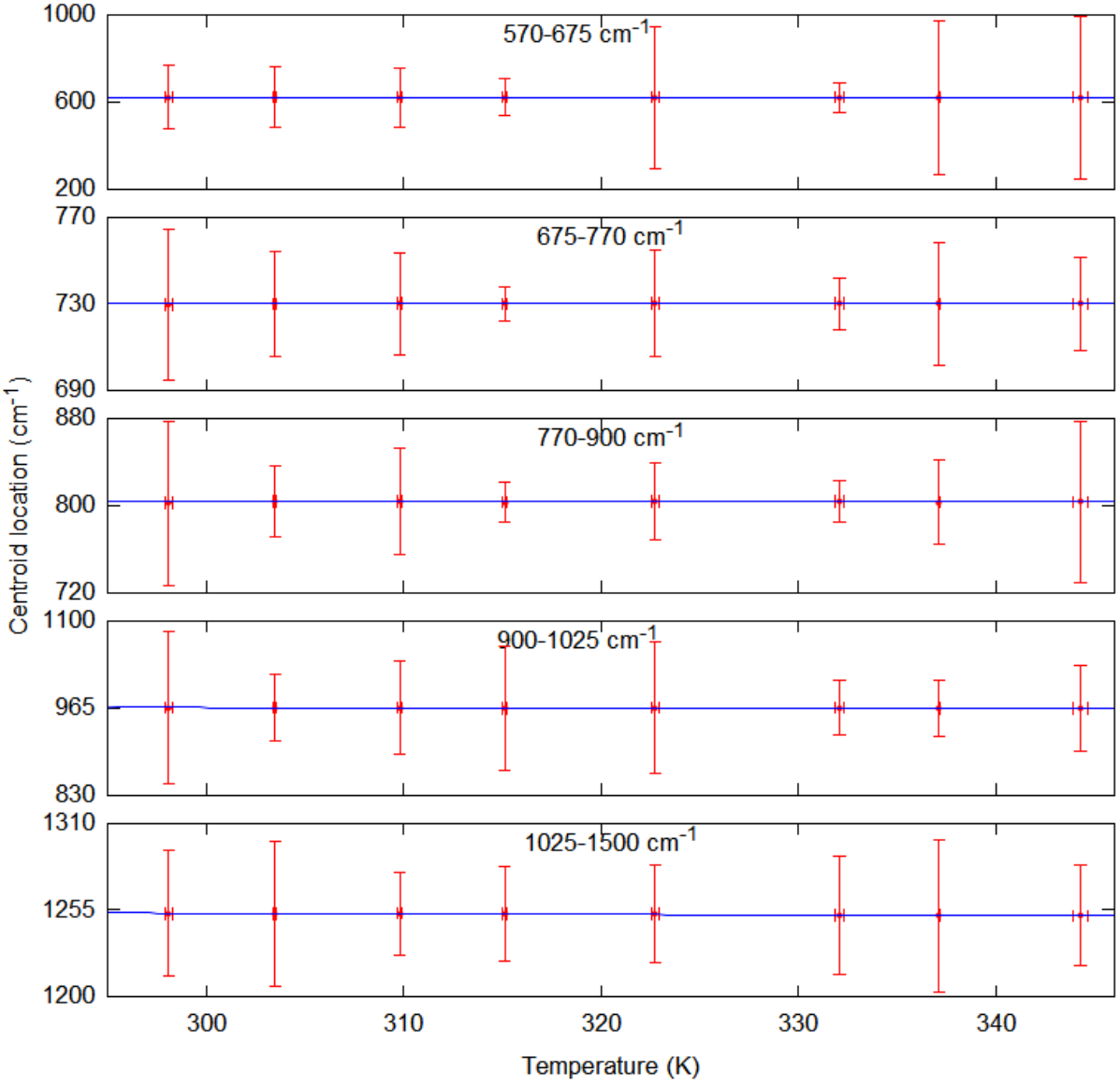

Figure 4.6: Position of the centroid in each band of PFTBA at different temperatures. Red points are from this work and the blue lines are linear fits. The horizontal errorbars indicate the standard deviation from all measurements taken at that temperature; whereas the vertical errorbars indicate the uncertainty centroid position from Section 3.2.3.

Table 4.3: Summary of RE and GWP_{100} for PFTBA at room temperature for different lifetimes and data sets.

Data Set	**Range (cm^{-1})**	**RE**	**Lifetime (years)**	**GWP_{100}**
Experimental	550-3000	0.782±0.106	500	6980±2090
			2000	7580±2270
DFT	0-3000	0.928±0.132	500	8280±2490
			2000	8990±2700
DFT+Exp	0-3000	0.803±0.106	500	7170±2150
			2000	7780±2330
Hong *et al.* [13]	500-3000	0.86±0.094	500	7100
3M [49]			2000	7200

[13] assumed a life time of 500 years and calculated a GWP of 7100, while 3M Inc. [49] published a lifetime of 2000 years leading to a GWP of 7200. Table 4.3 lists the GWP of PFTBA calculated for both lifetimes. For the lifetime of 500 years, the new result is smaller than the value of GWP previously reported in [13] when we only compare the experimental result; including the DFT calculation below 550 cm^{-1} yields a GWP higher than the Hong *et al.* reported value. For a lifetime of 2000 years, all of the GWP values from this work are higher than the value reported by [49]. From the error estimates described in Section 2.6 along with the uncertainty in absorption cross-sections, the GWP has an uncertainty of ˜30%. Overall, the conclusion of this work is that the previously published values for the GWP of PFTBA underestimate the true value.

Chapter 5

2,2,3,3,3-Pentafluoropropanol

This chapter summarizes the results of temperature-dependent absorption cross-section measurements of 2,2,3,3,3-pentafluoropropanol (PFPO). The work presented in this chapter has also been published as: Godin *et al.*, A study of the temperature dependence of the infrared absorption cross-sections of 2,2,3,3,3-pentafluoropropanol in the range of 298-362 K, *J. Quant. Spec. Rad. Trans.*, 2016 [47]. PFPO ($CF_3CF_2CH_2OH$) is a fluorinated alcohol, whose structure is shown in Figure 5.1. In this chapter, the first known temperature-dependent measurements of the IR absorption cross-sections of PFPO are presented. Additionally, the RE and GWP for PFPO are calculated, and compared with the previously published data.

5.1 Absorption Cross-Sections

Measured absorption cross-sections as a function of temperature are shown in Figure 5.2. Following Sellevåg *et al.* [15], the regions used to calculate the integrated absorption band strengths are: 565-700, 700-825, 850-1500, and 2840-3040 cm^{-1}. The peak absorption in the 850-1500 cm^{-1} band is approximately 30-60 times stronger than the peak absorption in the other bands.

5.2 Density Functional Theory

Badawi *et al.* [17] made DFT calculations for PFPO using the B3LYP functional and 6-311+G** basis set. They found that PFPO has three low-energy conformers depending on the orientations of the F-C-C-C (ϕ_1), C-C-C-O (ϕ_2), and C-C-O-H (ϕ_3) dihedral angles, as shown in Figure 5.1. The three conformers are named based on the positions of the

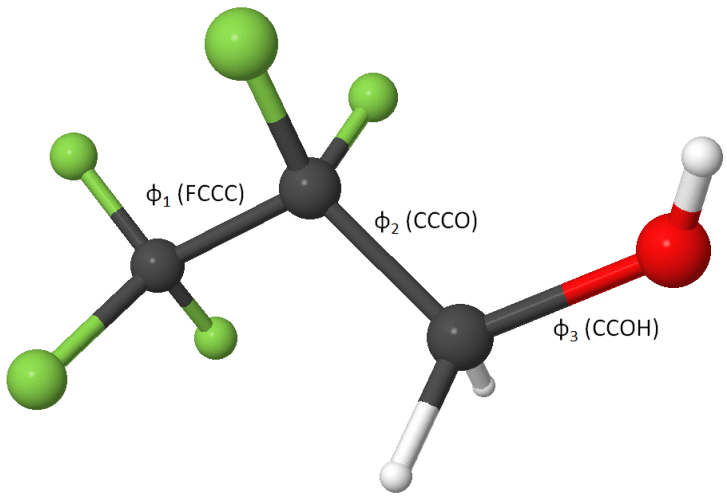

Figure 5.1: Projection image of PFPO. The red atom is oxygen, the green atoms are fluorine, the white atoms are hydrogen, and the grey atoms are carbon. Based on the published density functional theory study [17], there exist three low energy conformers: *Tgg* ($\phi_1 = 173^o$, $\phi_2 = 64^o$, $\phi_3 = 64^o$), *Ttg* ($\phi_1 = 181^o$, $\phi_2 = 183^o$, $\phi_3 = 63^o$), and *Tggl* ($\phi_1 = 181^o$, $\phi_2 = 72^o$, $\phi_3 = -71^o$). The *Ttg* conformation is shown.

dihedral angles: *trans-gauche-gauche (Tgg), trans-trans-gauche (Ttg)*, and *trans-gauche-anti-gauche (Tggl)*. From the calculated DFT minimum conformer electronic energies of these states, the equilibrium mixture of the different conformations of PFPO at a given temperature can be determined. A plot of the equilibrium ratios as a function of temperature is shown in Figure 5.3. Over the range of temperatures studied, the ratio between the different conformations changes very little.

The changing conformer ratio can be used to assign peaks to specific conformers by looking at the changes in the experimental spectra with temperature. From Figure 5.3, absorption peaks that decrease in amplitude correspond to vibrational modes from either the *Tgg* or *Ttg* conformers, whereas peaks that increase with temperature are from the *Tggl* conformer. Using the experimentally determined positions and calculated IR intensities of the three conformations from Badawi *et al.* [17], a theoretical spectrum is generated by combining the spectra of each of the individual conformers and scaling the IR intensities relative to their individual population percentages. Each vibrational band is approximated as a Gaussian function with a width of 8.5 cm^{-1}. The difference in both the experimental and theoretical spectra with temperature is shown in Figure 5.4.

The comparison of the locations of the vibrational modes between theory and experiment is shown in Figure 5.5. The difference between the theoretical transition location and observed location at 297.8 K is expressed as the linear relationship:

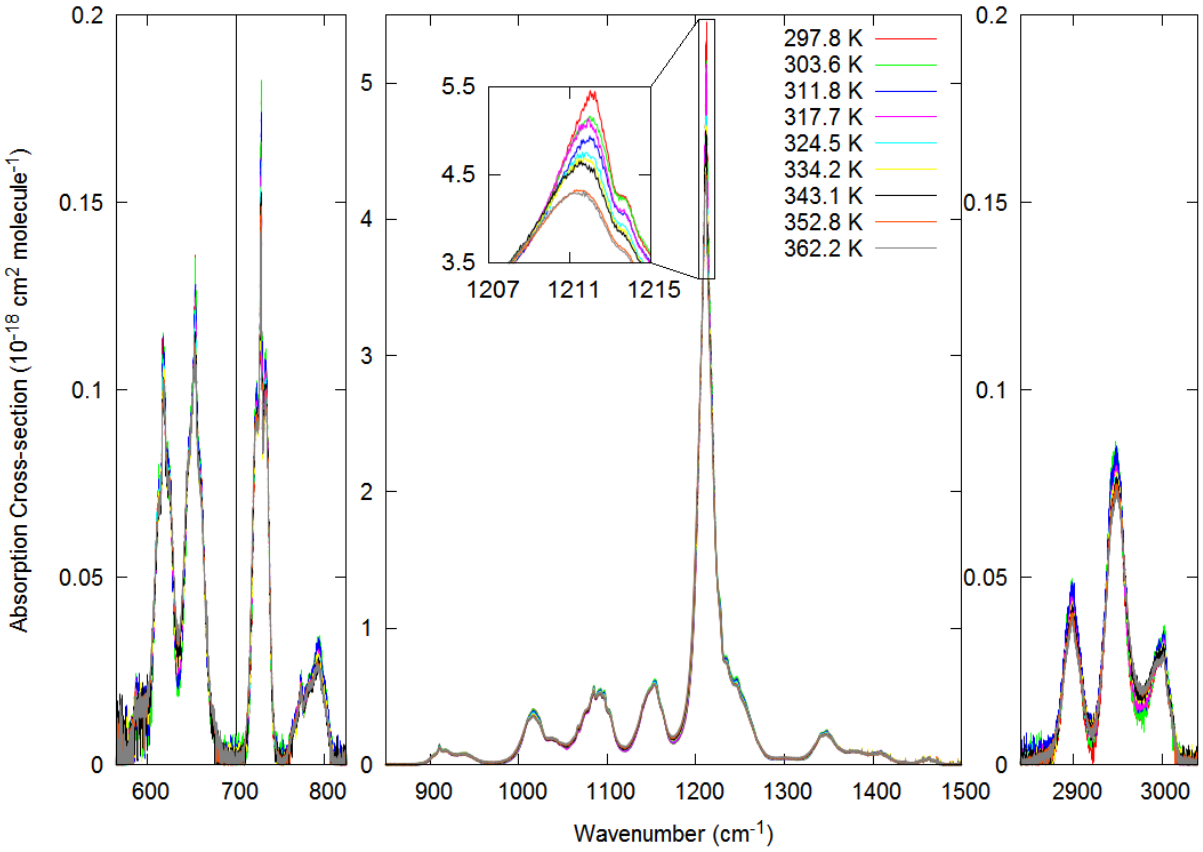

Figure 5.2: Experimental cross-section of PFPO at nine temperatures. Four absorption bands are defined from 565-700, 700-825, 850-1500, and 2840-3040 cm^{-1}. The overall integrated band has a defined range of 570-3025 cm^{-1}. The vertical scaling changes with the bands to account for the difference in strength between peak absorption of each band.

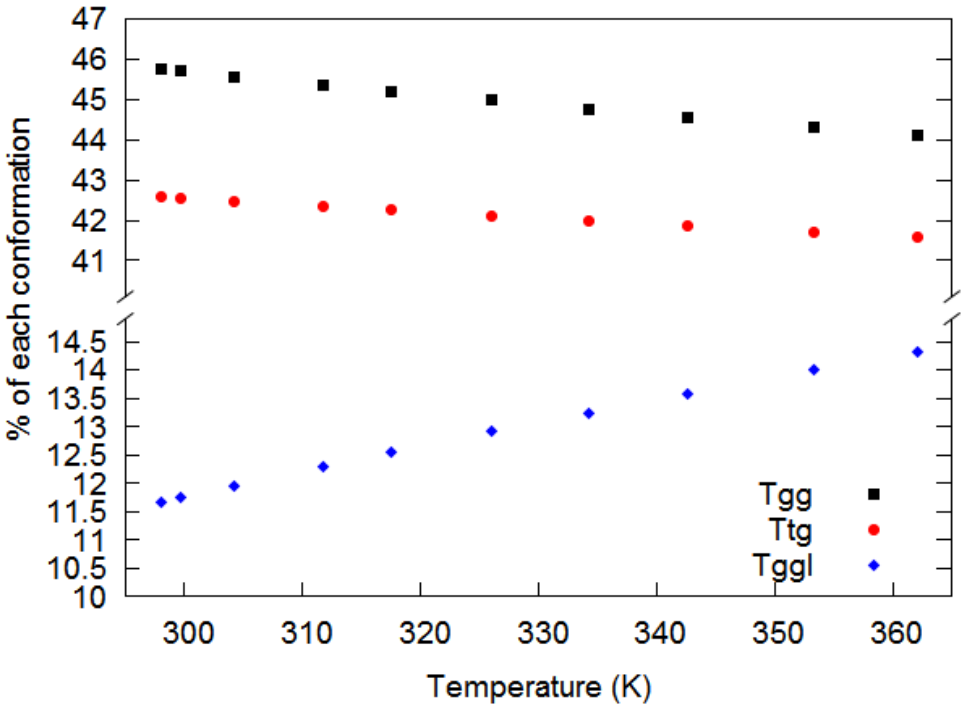

Figure 5.3: Equilibrium populations of the three conformations of PFPO as a function of temperature based on their relative energies calculated by Badawi *et al.* [17].

$\tilde{\nu}_{Exp} = 0.940 * \tilde{\nu}_{DFT} + 80.4\,\mathrm{cm}^{-1}$. This linear relation is applied to the composite DFT spectrum in order to adjust it to more closely match the experimental results for peaks that were outside of the experimental range. A direct comparison of the linearly scaled composite DFT and experimental spectra is shown in Figure 5.6. The DFT calculation overestimates the strength of the absorption of several peaks, and underestimates it for a few as well.

5.3 Integrated Band Strengths and Centroid Shifts

The integrated band strengths as a function of temperature are shown in Figure 5.7. The overall (565-3040 cm^{-1}) integrated band strength shows no significant change with temperature. Integrated band strengths are reported in Table 5.1. Overall, good agreement is seen between the previously published data [14, 15, 16] and these new measurements, with the exception being the 565-825 cm^{-1} bands where our results do not agree with the measurements from Antiñolo *et al.* [16]. It should be noted that the initial purity of the sample used in the study by Imasu *et al.* [14] is not specified, while in the work by Sellevåg *et al.* [15] the purity is 97%, and in Antiñolo *et al.* [16] it is 99.8%. The study by

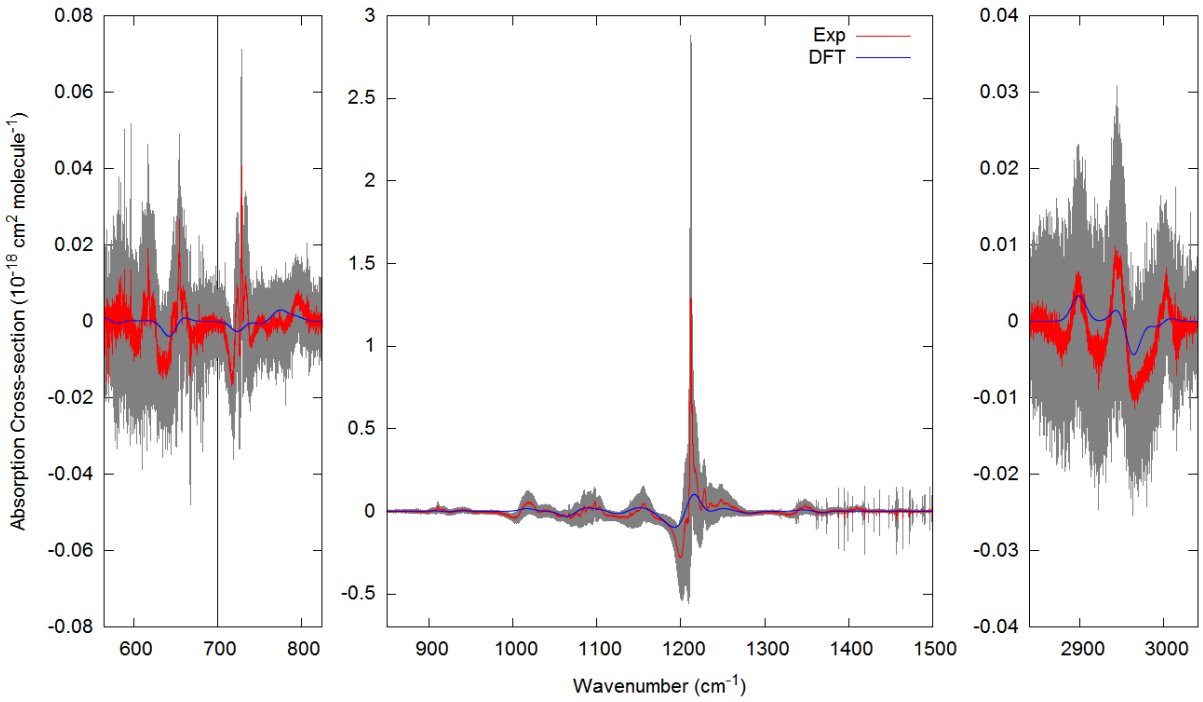

Figure 5.4: Difference in PFPO cross-section between the 297.8 K and 362.2 K spectra. Grey shading indicates the uncertainty of the experimental spectrum. The DFT spectrum difference is produced by assuming a conformer population predicted by a Maxwell-Boltzmann distribution going from 297.8 to 362.2 K and approximating absorption bands with Gaussian functions with a width of 8.5 cm^{-1} for the fundamental modes.

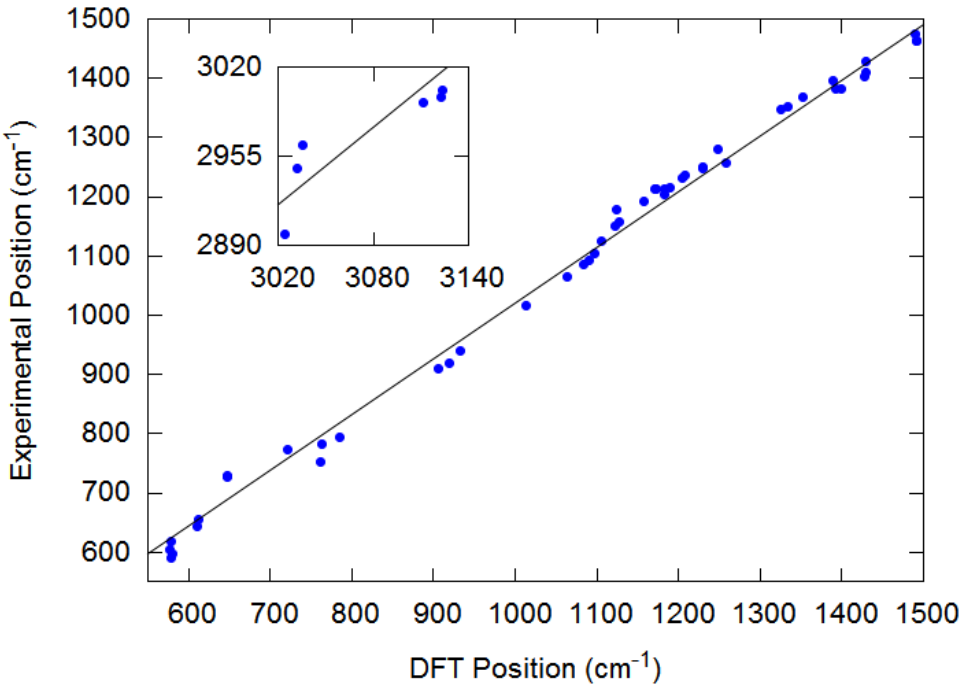

Figure 5.5: Theoretical absorption band locations of PFPO versus experimental band locations. Fitted line for 297.8 K has a slope of 0.940 ± 0.004 and intercept of $80.4 \pm 6.2\,\mathrm{cm}^{-1}$.

Imasu *et al.* [14] only covers 700-1500 cm^{-1} and thus does not include the 565-700 and 2840-3040 cm^{-1} bands; this explains why their overall integrated cross-section is lower than all other studies. DFT calculations provide integrated absorption cross-sections for each vibrational mode, so the intensity values for each vibration in a given region can be summed up and compared to the experimental result. The DFT calculation overestimates the strength of the absorption in all of the bands.

As shown in Figure 5.8, no significant trend in the position of the centroid as a function of temperature for any of the bands is seen, supporting the conclusion that temperature has little impact on the absorption cross-section of PFPO in the range studied.

5.4 Radiative Efficiencies and Global Warming Potentials

An instantaneous RE for PFPO of 0.257 ± 0.051 $\mathrm{Wm}^{-2}\mathrm{ppbv}^{-1}$ is calculated from the experimental data for a spectral range of 565-3000 cm^{-1}, which agrees within error with previously published data [7, 14]. The DFT calculation finds an instantaneous RE of

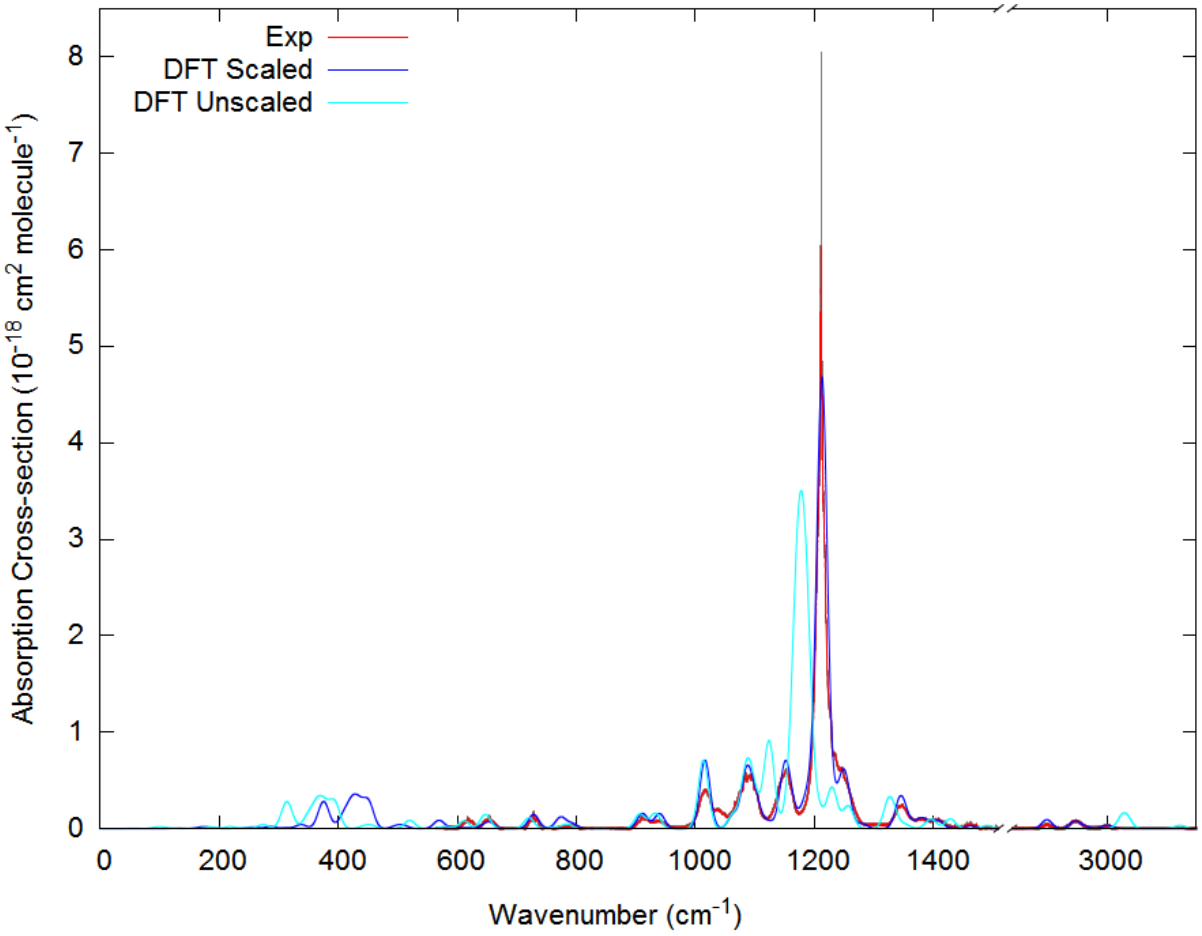

Figure 5.6: Comparison of experimental cross-section of PFPO with DFT adjusted calculations. The DFT spectrum is composed of the spectra of each of the three low energy conformers at the population ratios from Figure 5.3 for 297.8 K using Gaussian functions to approximate the vibrational modes with the locations of the modes linearly scaled to match with the experimental result. Grey shading indicates the error bars on the experimental data.

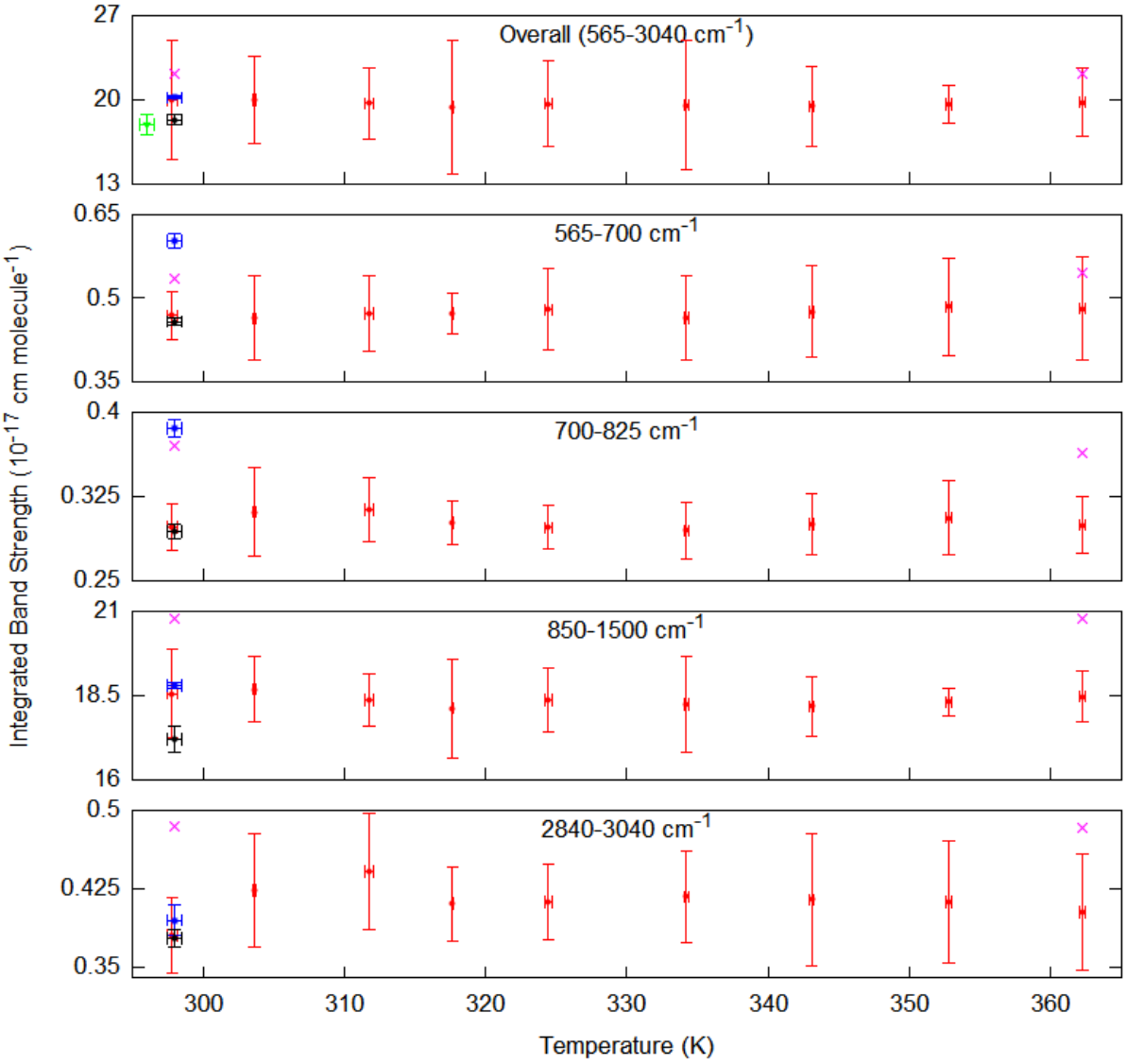

Figure 5.7: Integrated band strengths for PFPO at different temperatures. The red circles indicate data from this work, the blue squares for data from [16], the black diamonds are data from [15], the green triangle is data from [14], and the purple Xs are the DFT calculation. The horizontal errorbars indicate the standard deviation from all measurements taken at that temperature; whereas the vertical errorbars indicate the uncertainty in integrated band strength from Section 3.2.3.

Table 5.1: Published and measured integrated band strengths of PFPO at different temperatures.

Temperature	**Integrated Band Strengths (10^{-17} cm molecule^{-1})**				
(K)	565-3040 cm^{-1}	565-700 cm^{-1}	700-825 cm^{-1}	850-1500 cm^{-1}	2840-3040 cm^{-1}
296.0±0.5*	17.9±0.7				
298.0±2**	18.330±0.400	0.458±0.006	0.294±0.007	17.2±0.4	0.378±0.008
298.0±0.5***	20.183±0.102	0.602±0.012	0.386±0.008	18.8±0.100	0.395±0.014
DFT	21.18	0.535	0.371	20.79	0.484
297.8±0.32	19.9±5.0	0.469±0.043	0.298±0.021	18.5±1.3	0.380±0.036
303.6±0.07	20.0±3.7	0.464±0.075	0.311±0.039	18.7±1.0	0.424±0.053
311.8±0.35	19.7±3.0	0.473±0.068	0.314±0.029	18.4±0.8	0.441±0.055
317.6±0.05	19.4±5.6	0.473±0.036	0.302±0.019	18.1±1.5	0.411±0.035
324.4±0.24	19.7±3.5	0.480±0.072	0.297±0.020	18.4±0.9	0.412±0.036
334.2±0.17	19.5±5.4	0.465±0.074	0.295±0.026	18.2±1.4	0.417±0.044
343.1±0.16	19.5±3.3	0.476±0.081	0.300±0.027	18.2±0.9	0.415±0.063
352.8±0.22	19.6±1.6	0.484±0.087	0.306±0.033	18.3±0.4	0.412±0.058
362.2±0.25	19.8±2.8	0.481±0.092	0.300±0.025	18.5±0.7	0.403±0.055
DFT	21.18	0.545	0.363	20.79	0.483
Average	19.7±1.0	0.472±0.020	0.301±0.008	18.35±0.26	0.410±0.015

* Value taken from [14]. ** Values taken from [15]. *** Values taken from [16].

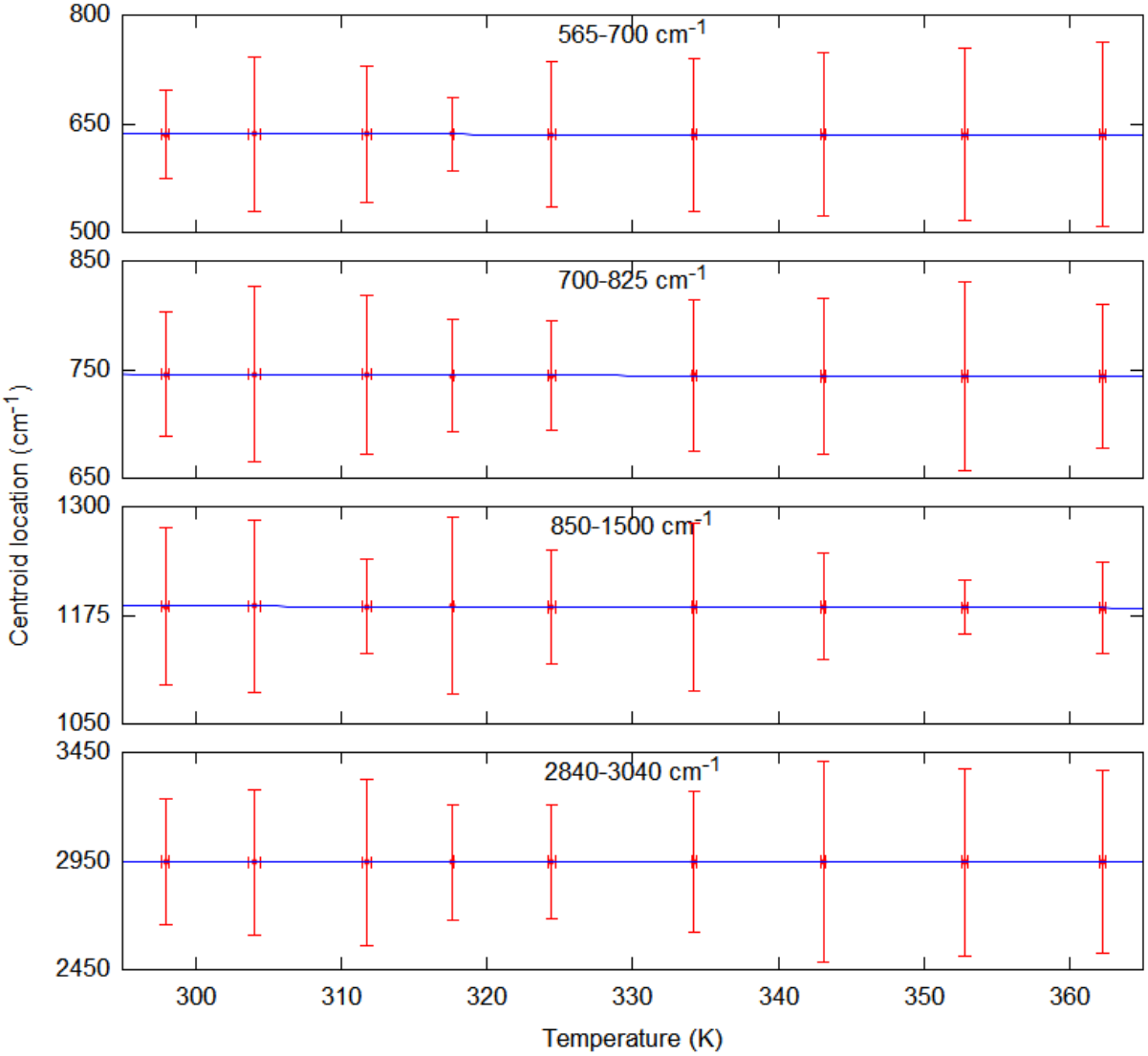

Figure 5.8: Position of the centroid in each band of PFPO at different temperatures. The horizontal errorbars indicate the standard deviation from all measurements taken at that temperature; whereas the vertical errorbars indicate the uncertainty centroid position from Section 3.2.3. The blue lines are linear fits.

0.301 $Wm^{-2}ppbv^{-1}$, which is largely due to an overestimation in intensity of the band strength of some of the vibrational modes. Using the scaled theoretical spectrum, the RE in the region below 565 cm^{-1} can be estimated; here the DFT calculation finds an RE of 0.043 $Wm^{-2}ppbv^{-1}$, yielding a total instantaneous RE of 0.300 $Wm^{-2}ppbv^{-1}$ for 0-3000 cm^{-1} when combined with the experimental result. A summary of PFPO REs are shown in Table 5.2.

Imasu *et al.* [14] used a lifetime of 0.43 yr based on empirically derived reaction rates with the OH radical and did not take lifetime corrections into account. Antiñolo *et al.* [16] used a lifetime of 0.33 yr based on their experimentally derived reaction rates with the OH radical. Furthermore, they considered other sinks of PFPO to be negligible, and only based their lifetime on OH radical reactions, but they also did not apply the fractional lifetime correction to account for VMR profile when determining GWP. Both papers stress that the lifetime is approximate as it relies heavily on the concentration of the OH radical, which can vary significantly with location and season. Both Imasu *et al.* [14] and Sellevåg *et al.* [15] express their GWP relative to CFC-11; converting to GWPs relative to CO_2 is done by multiplying their values by the GWP of CFC-11 relative to CO_2. Hodnebrog *et al.* [7] and the AR5 [6] use the REs from previous publications along with lifetime of 0.3 yr and S-shaped $f(\tau)$ when determining the GWP of PFPO. Choice of lifetime can change the GWP value by 14%.

A summary of PFPO GWP calculations is given in Table 5.2. From the error estimates described in Section 2.6 along with the uncertainty in absorption cross-sections, the GWP has an uncertainty of ˜40%. The new value for the GWP of PFPO falls within the range of previously published values, and increases confidence in these values.

Table 5.2: Summary of RE and GWP_{100} values for PFPO at room temperature.

Data Set	**Range (cm^{-1})**	**Lifetime (yr)**	**f(t)**	**RE ($Wm^{-2}ppb^{-1}$)**	**GWP_{100}**
Imasu *et al.* [14]	700-1500	0.43	1		18
Sellevåg *et al.* [15]	490-1500	0.33	1	0.252±0.028	23.1±9.2
Antiñolo *et al.* [16]	500-4000	0.33	1	0.26±0.028	25.0±10
Hodnebrog *et al.* [7]	700-1500	0.3	S-Shaped	0.27±0.029	19±7.6
DFT	0-3000	0.33	S-Shaped	0.344±0.048	23.2±9.3
Experimental	565-3000	0.33	S-Shaped	0.257±0.026	19.8±7.9
Experimental+DFT	0-3000	0.33	S-Shaped	0.300±0.027	23.1±9.2

Chapter 6

1,1,1,3,3,3-Hexafluoro-2-propanol

This chapter summarizes the results of temperature-dependent absorption cross-section measurements of 1,1,1,3,3,3-hexafluoro-2-propanol, also known as 1,1,1,3,3,3-hexafluoropropan-2-ol or hexafluoroisopropanol (HFIP). The results of this chapter have been submitted as a paper to the *Journal of Quantitative Spectroscopy and Radiative Transfer* and have recently been accepted as Godin *et al.*, Conformational analysis and global warming potentials of 1,1,1,3,3,3-hexafluoro-2-propanol from absorption spectroscopy, *J. Quant. Spec. Rad. Trans.*, 2017 [53]. HFIP ($(CF_3)_2CHOH$) exists in two stable conformers, generally referred to as *trans* and *gauche*, based on the position of the H-C-O-H dihedral bond angle [18]. The *trans* and *gauche* conformers are shown in Figure 6.1. The *trans* conformer is reported by several groups to be more energetically stable than the *gauche* conformer by approximately 4 kJ/mol [54, 55, 56, 57].

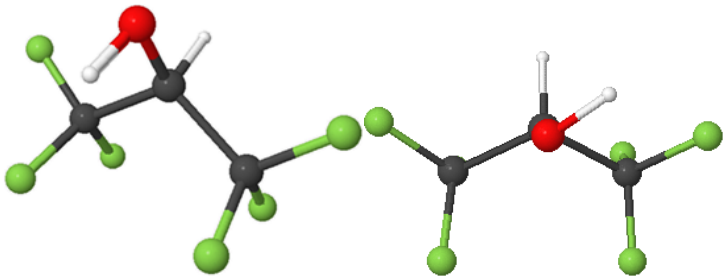

(a) *Trans*-conformer (b) *Gauche*-conformer

Figure 6.1: Projection image of HFIP. The red atom is oxygen, the green atoms are fluorine, the white atoms are hydrogen, and the grey atoms are carbon. There exist two low-energy conformers based on the dihedral angle of the H-C-O-H group.

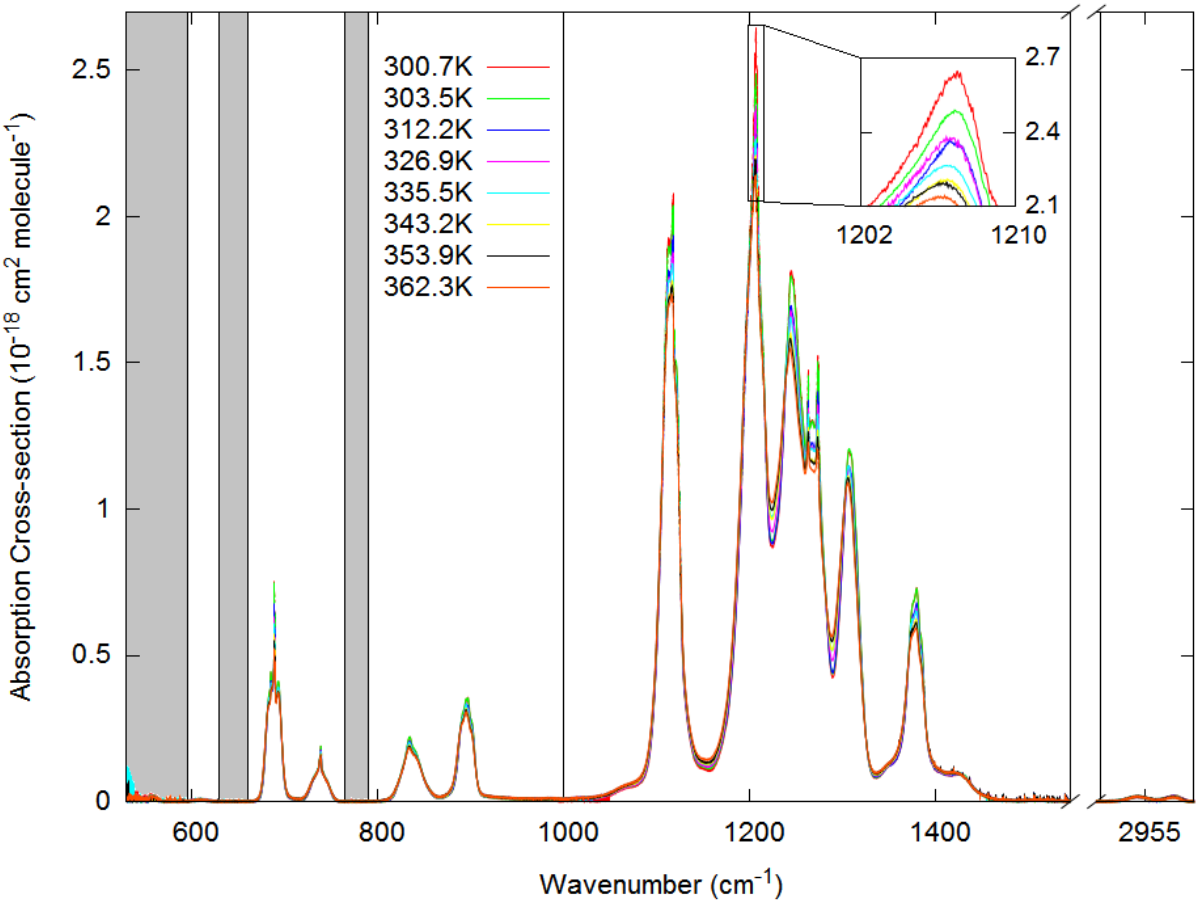

Figure 6.2: Experimental cross-section of HFIP at eight temperatures. Five absorption bands are defined from 595-630, 660-765, 790-1000, 1000-1545 and 2905-3010 cm^{-1}. The overall integrated band has a defined range of 595-3010 cm^{-1}. The grey shading indicates regions that have no observed absorption.

6.1 Absorption Cross-Sections

Measured absorption cross-sections of HFIP as a function of temperature are shown in Figure 6.2. Near 530 cm^{-1}, the limit of the detector is reached and the amplitude of the cross-section becomes less reliable. Nevertheless, the location of peaks in that vicinity can still be resolved. There are some weak ($< 10^{-20}$ cm^{2}molecule^{-1}) overtone bands present in the 2200 to 2600 cm^{-1} region that are not included in the figures.

6.2 Density Functional Theory

DFT calculations for HFIP were performed using the B3LYP functional and 6-311++G(3*df*, 3*pd*) basis set with anharmonic couplings, which is at a higher level of

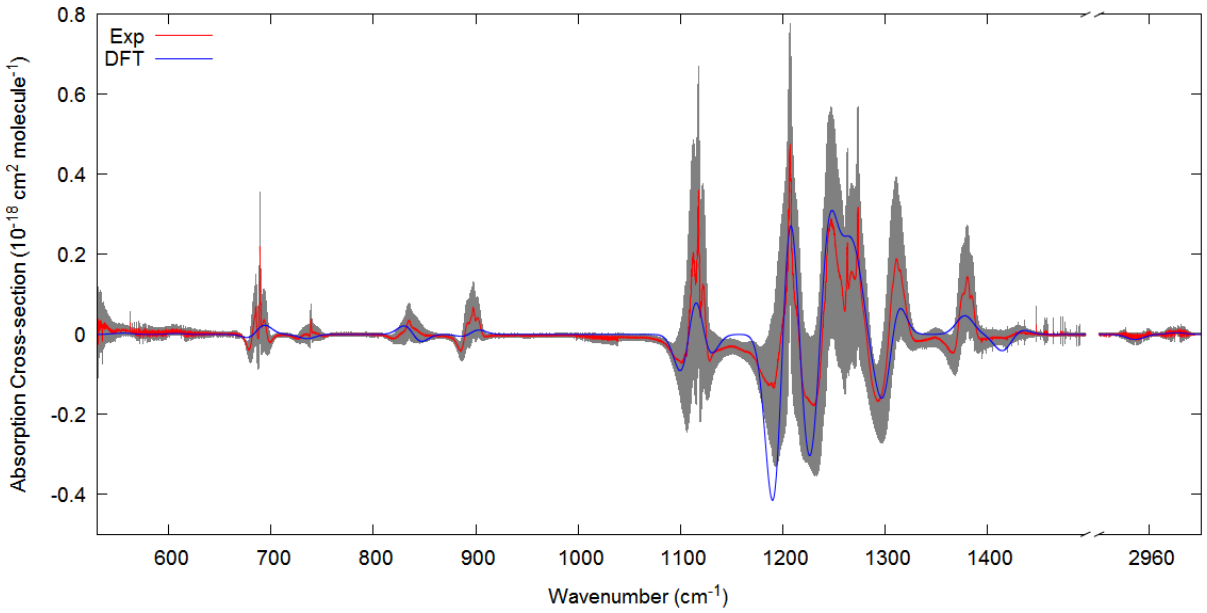

Figure 6.3: Difference in cross-section between the 300.6 K and 362.3 K spectra of HFIP. The DFT spectra difference is produced by assuming a change of 14% in conformer population going from 300.6 to 362.3 K and assuming a Gaussian shape with a width of 8.5 cm^{-1} for the fundamental modes. The grey shading indicates the uncertainty on the experimental values.

complexity than previously published DFT calculations for HFIP [22, 54, 55, 56]. The DFT calculation of band position agrees with prior published values to within 10 cm^{-1}, with the exception of the OH torsion of the *gauche*-conformer (mode #4), where the value disagrees by 36 cm^{-1}. The conformer ratio is predicted to vary with temperature following a Maxwell-Boltzmann distribution as the *gauche*-conformer becomes more populated at higher temperatures. By looking at the changes between experimental spectra with increasing temperature, transitions can be assigned to the correct conformer depending on whether the strength of the absorption increased (*gauche*-conformer) or decreased (*trans*-conformer) as shown in Figure 6.3. The assignments and comparisons to DFT and prior publications are shown in Tables 6.1 and 6.2. The assignments in this work agree with the prior publications and DFT prediction for the majority of the lines. The exception is vibrational mode #28, for which the *gauche*-conformer is observed at lower wavenumber than the *trans*-conformer, which is opposite to both the DFT calculation and prior publication assignments [22].

Additionally, the amplitude of the peaks in Figure 6.3 can be used to determine the change of ratio between the conformers over the temperature range studied. A Boltzmann distribution using the DFT-calculated energy for each conformer predicts a change of approximately 8% in conformer ratio over this temperature range, with 72% of molecules

in the *trans*-conformer at 300.6 K. Another method to estimate the ratio is by looking at a well-resolved doublet, such as the OH stretching at 2905-3010 cm^{-1}. Using the relative amplitude of this vibrational mode, a ratio of 78% *trans* and 22% *gauche* at 300.6 K and 64% *trans* and 36% *gauche* at 362.3 K are obtained. This ratio change of 14% agrees with the experimental result better than the 8% ratio change predicted from a Maxwell-Boltzmann distribution.

The difference between the DFT spectra and experimental spectra reveals the location of combination bands. The locations, strengths, and possible assignments of the combination bands are shown in Table 6.3. Each vibrational mode was assumed to have a Gaussian shape with a width of 8.5 cm^{-1}, while the combination bands were assumed to have a width of 11 cm^{-1} to obtain a DFT spectrum that best resembles the experimental result.

From the assignments, the relationship between theoretical and experimental line positions can be evaluated. The comparison between theory and experiment is shown in Figure 6.4. The relationship between the theoretical transition and observed transition (using both data from this work and [18, 19, 21]) is fitted to a linear function: $\tilde{\nu}_{Exp} = 0.973 * \tilde{\nu}_{DFT} + 23.6\,cm^{-1}$. This linear relation was applied to the composite DFT spectrum to adjust locations of peaks below 530 cm^{-1} for which there are no experimental data.

From this analysis, a DFT spectrum is produced that closely matches the experimental spectrum in the observed range and that is believed to more accurately predict the spectrum outside of this range. A direct comparison of the composite DFT spectrum and experimental absorption cross-sections is shown in Figure 6.5.

6.3 Integrated Band Strengths and Centroid Shifts

Measured absorption cross-sections as a function of temperature are shown in Figure 6.2. The regions used to calculate the integrated absorption band strengths are: 595-630, 660-765, 790-1000, 1000-1545 and 2905-3010 cm^{-1}. The integrated band strengths as a function of temperature are shown in Figure 6.6. The overall (595-3010 cm^{-1}) integrated band strength shows no significant change with temperature.

Integrated bands strengths are reported in Table 6.4. There is good agreement with previously published data [14] within the error bars. It should be noted that the initial purity of the sample used in the study by Imasu *et al.* [14] is not specified and it only covers a 700-1500 cm^{-1} range; thus does not include the 595-630 and 2905-3010 cm^{-1} bands. This explains why their overall integrated cross-section appears lower than this work. DFT calculations provide integrated absorption cross-sections for each vibrational

Table 6.1: Summary of band locations of the HFIP *trans*-conformer from DFT and experiment.

Mode	**Experiment (this work) (cm^{-1})**	**Experiment ([21]*, [19]**, [22]***) (cm^{-1})**	**B3LYP 6-311++G(3*df*, 3*pd*) (cm^{-1})**	**B3LYP 6-311++G(*df*,*pd*) [22] (cm^{-1})**
1			21	22
2		90*	85.5	84
3		163*	164.9	163
4		235*	225	225
5			246.9	246
6		289*	286.9	288
7		331*	321.4	320
8		352*	340	340
9		332*	378.7	388
10		460**	454.5	455
11		518**	510.5	512
12	536.8	535**	528.2	529
13	555	554**	547.4	550
14	608.8	609**	603.5	605
15	689.1	688**	686.2	688
16	738.9	740**	734.9	736
17	834.5	836**	826.3	827
18	897.3	898**	892.2	894
19	1112.9	1105**	1094.3	1103
20	1117.7	1113**	1114.1	1115
21	1188	1146***	1158	1168
22	1207	1202**	1188.5	1196
23	1245	1216***	1216.3	1227
24	1263.7	1243**	1244.1	1245
25	1275	1260**	1268.2	1270
26	1309	1311**	1305.4	1307
27	1378.5	1380**	1376.3	1378
28	1433	1415**	1424	1423
29	2986.5	2994**	3109	3104
30		3604**	3792.1	3794

Table 6.2: Summary of band positions (cm^{-1}) of the HFIP *gauche*-conformer from experiment and DFT.

Mode	**Experiment (this work) (cm^{-1})**	**Experiment ([21]*, [19]**, [22]***) (cm^{-1})**	**B3LYP 6-311++G(3*df*, 3*pd*) (cm^{-1})**	**B3LYP 6-311++G(*df*,*pd*) [22] (cm^{-1})**
1			36.4	43
2			86.3	82
3			158.6	155
4		211*	228.9	193
5		288.9**	237.1	228
6		233**	262.3	258
7		297**	295.7	297
8		328**	324.2	323
9		350**	349.2	347
10		463**	458.5	457
11		513**	511.3	513
12	533.3	532**	531.8	533
13	548.9	548**	546.4	547
14	616	610**	604.1	603
15	685.1	684***	680.4	683
16	737.2	739**	733.6	734
17	842	841***	844.4	842
18	895	892***	887.8	892
19	1105	1105***	1088.8	1096
20	1121	1122***	1134.3	1132
21	1128.6	1127***	1146.4	1146
22	1192	1182***	1183	1185
23	1222	1198***	1196.3	1200
24	1231	1224***	1229.8	1233
25	1282	1270***	1289	1281
26	1300	1295***	1295.4	1302
27	1379	1376***	1383.1	1385
28	1415	1422***	1439.4	1440
29	2946.1	2938***	3045	3039
30		3617***	3831	3843

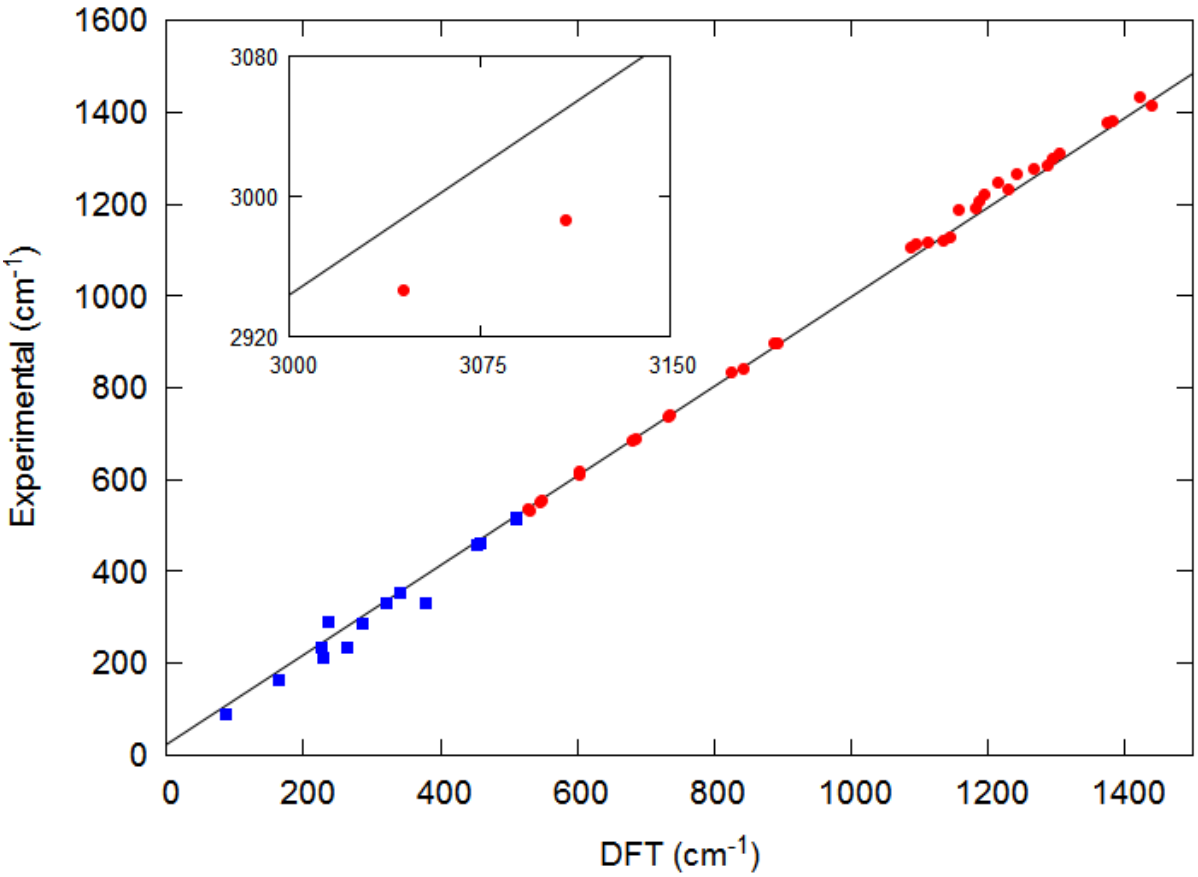

Figure 6.4: Experimental absorption peak locations of HFIP versus DFT peak locations. The fitted line has a slope of 0.973 ± 0.005 and an intercept of 23.6 ± 5.8 cm^{-1}. Red circles indicate data from this work, while the blue squares are experimental data below 530 cm^{-1} are taken from [18, 19, 21].

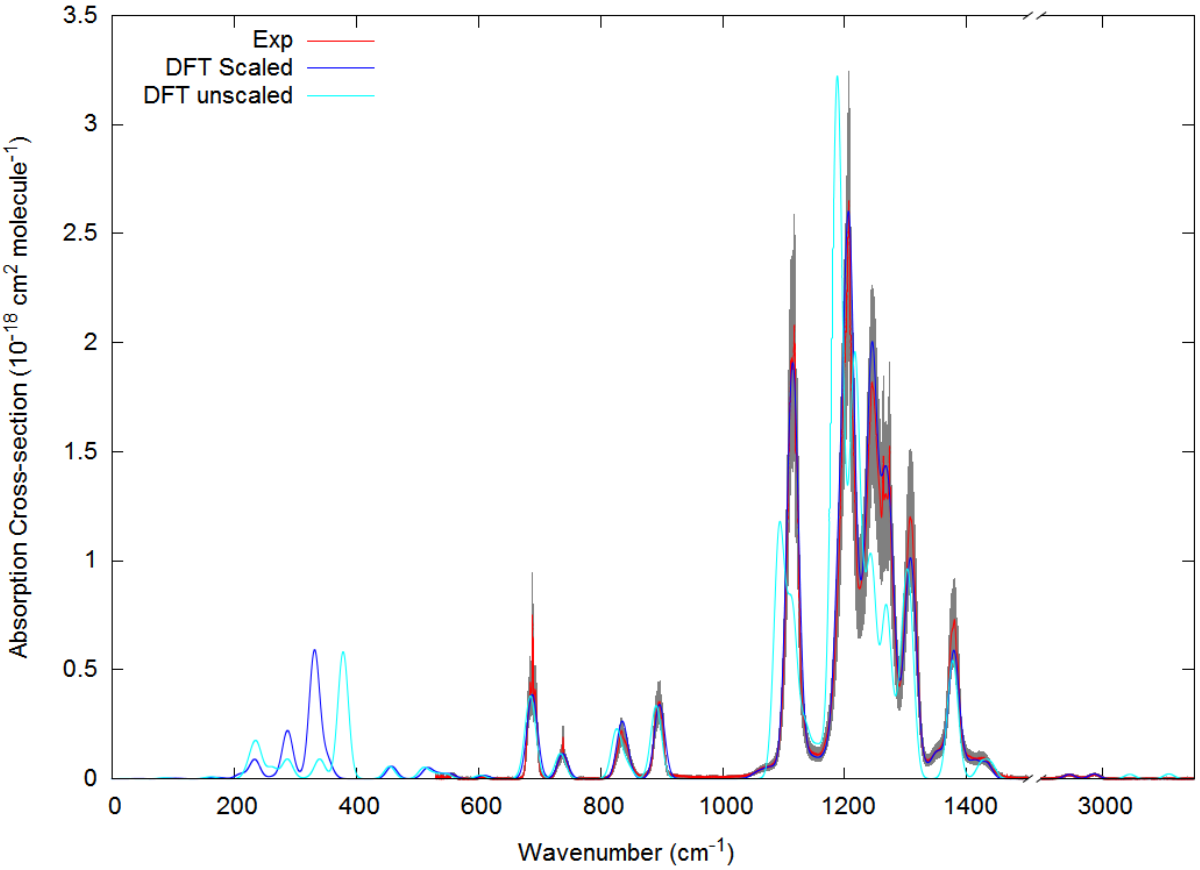

Figure 6.5: Comparison of experimental cross-sections of HFIP with DFT calculations. The DFT spectrum is composed of the spectra of each of the two low energy conformers at the population ratio of 78% *trans* and 22% *gauche* assuming a Gaussian shape with a width of 8.5 cm^{-1} for the fundamental modes, and a width of 11 cm^{-1} for the combination bands. The grey shading indicates the uncertainty on the experimental values.

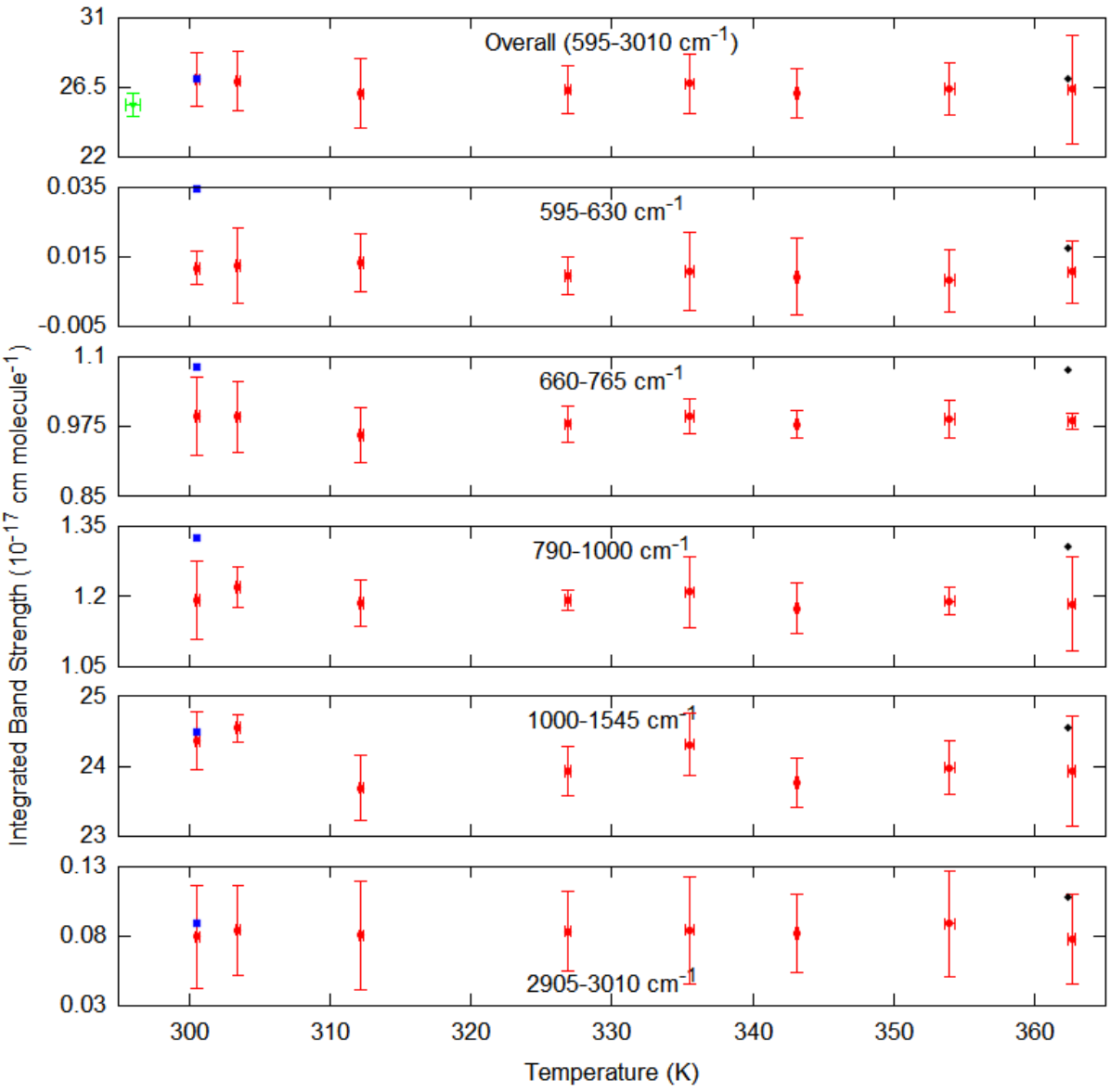

Figure 6.6: Integrated band strengths for HFIP at different temperatures. Red circles indicate data experimental data from this work, the blue squares indicate the DFT calculations for 300.6 K conformer ratio, the black diamonds indicate the DFT calculations for 362.3 K conformer ratio, and the green triangle indicates the previously published data from [14]. The horizontal errorbars indicate the standard deviation from all measurements taken at that temperature; whereas the vertical errorbars indicate the uncertainty in integrated band strength from Section 3.2.3.

Table 6.3: Identified combination bands in HFIP.

Location (cm^{-1})	**Line Strength (km/Mol)**	**Possible Assignment**
1059	5	*trans*-modes 3 and 18
1080	8	*gauche*-modes 10 and 14 *gauche*- modes 12 and 13
1146	15	*gauche*-modes 10 and 15 *trans*-modes 12 and 17
1172	18	*gauche*-modes 1 and 20 *trans*-modes 7 and 17
1318	16	*trans*-modes 1 and 25
1352	20.5	*trans*-modes 4 and 22 *trans*-modes 11 and 19
1395	12	*gauche*-modes 5 and 19

mode, so the intensity values for each vibrational mode can be simply summed up in a given region and compared to the experimental result. There is generally good agreement between the experimentally derived integrated band strengths and the DFT calculated values.

As shown in Figure 6.7, no significant trend in the position of the centroid as a function of temperature for any of the bands is seen, supporting the conclusion that temperature has little impact on the absorption cross-section of HFIP in the range studied.

6.4 Radiative Efficiencies and Global Warming Potentials

The instantaneous RE for HFIP was found to be 0.293±0.059 $Wm^{-2}ppbv^{-1}$ from the experimental data at 300.6 K using a spectral range of 530-3000 cm^{-1}, which agrees within error with previously published data [7, 14]. From the DFT spectrum, an instantaneous RE of 0.324 $Wm^{-2}ppbv^{-1}$ is calculated. This is higher than the experimentally derived value largely due to an overestimation in intensity in the 765-1300 cm^{-1} region. Using the scaled DFT spectrum, the RE in the region 0 to 530 cm^{-1} can also be estimated. Including this region, the DFT calculation now yields an instantaneous RE of 0.348 $Wm^{-2}ppbv^{-1}$ for 0-3000 cm^{-1}, an increase of 0.024 $Wm^{-2}ppbv^{-1}$ from only the 530 to 3000 cm^{-1} range. The increase can be added to the experimental RE value to give a combined experimental/DFT RE of 0.317±0.063 $Wm^{-2}ppbv^{-1}$, which is the best estimate of the RE

Table 6.4: Measured and published integrated band strengths of HFIP at different temperatures.

Temperature	**Integrated Band Strengths** (10^{-17} **cm molecule**$^{-1}$)					
(K)	595-3010 cm^{-1}	595-630 cm^{-1}	660-765 cm^{-1}	790-1000 cm^{-1}	1000-1545 cm^{-1}	2905-3010 cm^{-1}
296.0±0.5*	25.4±0.8					
300.6**	27.03	0.035	1.082	1.326	24.50	0.090
300.6±0.2	27.0±1.7	0.012±0.005	0.994±0.070	1.192±0.083	24.37±0.41	0.079±0.037
303.5±0.1	26.9±1.9	0.013±0.011	0.993±0.064	1.220±0.044	24.55±0.20	0.084±0.032
312.2±0.1	26.1±2.2	0.013±0.008	0.960±0.048	1.186±0.049	23.69±0.47	0.080±0.039
326.9±0.2	26.3±1.6	0.010±0.005	0.980±0.033	1.192±0.022	23.93±0.36	0.083±0.028
335.5±0.3	26.8±1.9	0.011±0.011	0.994±0.031	1.210±0.076	24.31±0.45	0.084±0.039
343.1±0.1	26.1±1.6	0.009±0.011	0.980±0.024	1.174±0.055	23.76±0.36	0.082±0.028
353.9±0.4	26.4±1.7	0.008±0.009	0.988±0.034	1.190±0.028	23.98±0.39	0.089±0.038
362.6±0.3	26.4±3.5	0.011±0.009	0.985±0.015	1.184±0.102	23.93±0.80	0.078±0.033
362.6**	27.08	0.030	1.077	1.309	24.55	0.108
Average	26.49±0.65	0.011±0.003	0.986±0.009	1.193±0.014	24.21±0.12	0.082±0.012

* Value taken from [14]. ** DFT Calculation.

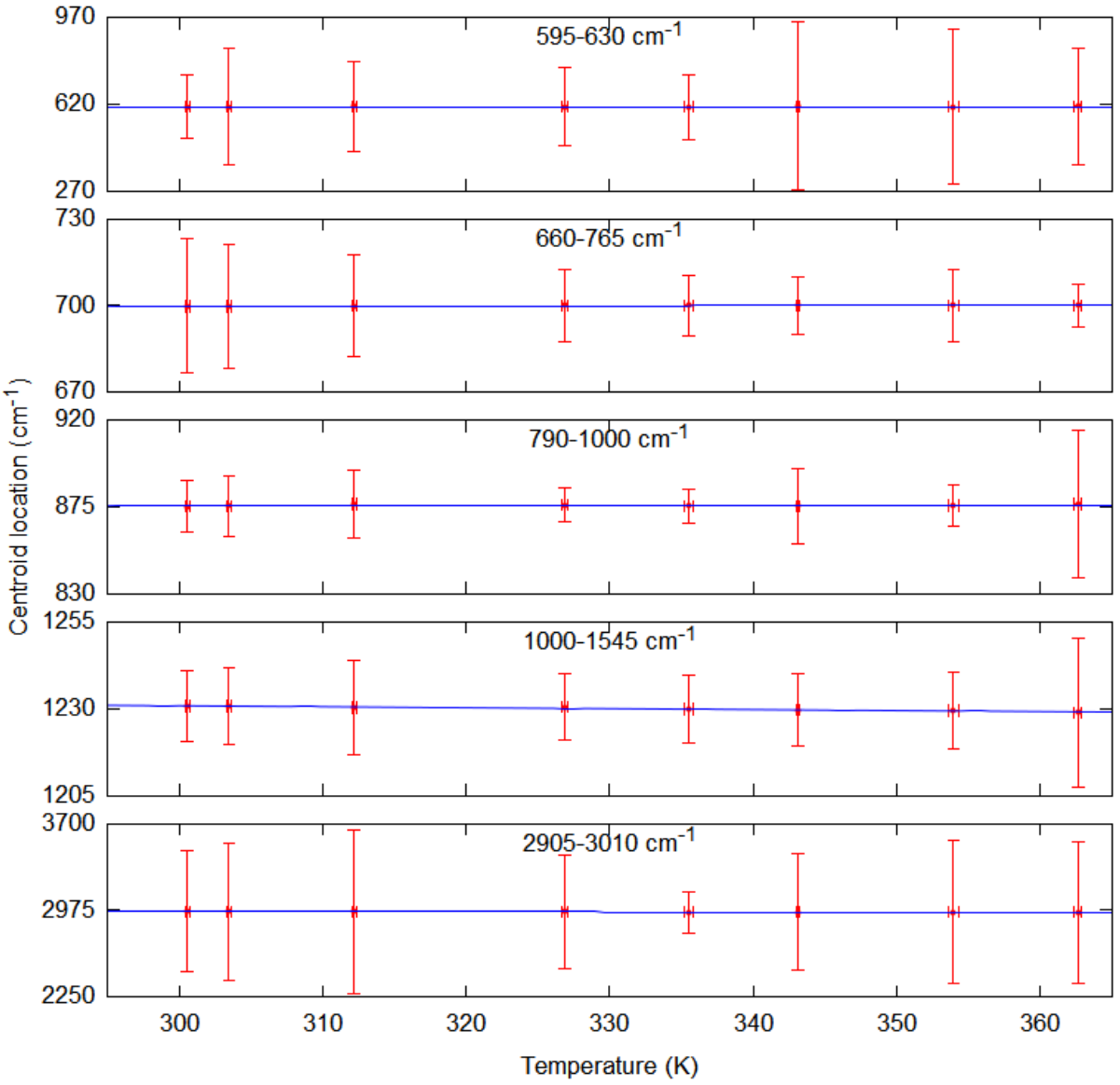

Figure 6.7: Position of the centroid in each band of HFIP at different temperatures along with linear fits. The horizontal errorbars indicate the standard deviation from all measurements taken at that temperature; whereas the vertical errorbars indicate the uncertainty centroid position from Section 3.2.3.

Table 6.5: Summary of GWP_{100} values for HFIP at room temperature.

Data Set	**Temp. (K)**	**Range (cm^{-1})**	**RE ($Wm^{-2}ppb^{-1}$)**	**GWP_{100}**
Imasu *et al.* [14]	296	700-1500	0.31±0.062	100±40
Hodnebrog *et al.* [7]	296	700-1500	0.31±0.062	182±73
Exp	300.6	530-3000	0.293±0.040	188±75
DFT	300.6	0-3000	0.348±0.049	223±89
Exp+DFT	300.6	0-3000	0.317±0.040	203±81

of HFIP over the full range of the Pinnock curve.

There are no measured vertical profiles available for HFIP. Hodnebrog *et al.* [7] assumed an S-shaped $f(\tau)$, which is also used in the IPCC AR5 [6]. Following this, an S-shaped $f(\tau)$ is also assumed and the suggested lifetime correction is applied when calculating the GWP. For the calculation of GWP, Imasu *et al.* [14] used a lifetime of 1.9 years based on empirically derived reaction rates with the OH radical and did not take the fractional lifetime corrections into account. Imasu *et al.* [14] express their GWP relative to CFC-11; to convert to GWPs relative to CO_2 their values are multiplied by the GWP of CFC-11 relative to CO_2. Hodnebrog *et al.* [7] use the REs from previous publications along with lifetime of 1.9 years and S-shaped $f(\tau)$ when determining the GWP of HFIP.

A summary of HFIP GWP calculations is given in Table 6.5. From the error estimates described in Section 2.6 along with the uncertainty in absorption cross-sections, the GWP has an uncertainty of ˜40%. This new value for the GWP of HFIP falls within the range of previously published values, and increases our confidence in these values; however these values do not include contributions from below 530 cm^{-1}, suggesting the accepted value is underestimating the GWP of HFIP.

Chapter 7

Perfluorodecalin and 2H,3H-perfluoropentane

This chapter summarizes the results of temperature-dependent absorption cross-section measurements of fluorinated compounds measured in collaboration with Dr. Karine Le Bris. Dr. Le Bris made measurements using our facilities and I assisted with taking some of the measurements and the calculations of RE and GWPs. The two molecules are perfluorodecalin (PFDC), and 2H,3H-perfluoropentane (HFC-43-10mee). PFDC is shown in Figure 7.1, and HFC-43-10mee is shown in Figure 7.2. These molecules were only studied at three temperatures in the range of 300-340 K. The PFDC results have been published as Le Bris, *Cis-* and *trans*-perfluorodecalin: Infrared spectra, radiative efficiency and global warming potential, *J. Quant. Spec. Rad. Trans.*, 2017 [58]. The HFC-43-10mee results are in press in the *Journal of Molecular Spectroscopy* [59].

7.1 Absorption Cross-Sections

Measured absorption cross-sections of PFDC as a function of temperature are shown in Figures 7.3 and 7.4. Measured absorption cross-sections of HFC-43-10mee as a function of temperature are shown in Figure 7.5. PFDC was measured at 300, 320, and 340 K; while HFC-43-10mee was measured at 305, 320, and 340 K. Absorption cross-sections for both species were recorded at at resolution of 0.1 cm^{-1} and a spectral range of 550-3000 cm^{-1}.

Pure *cis*-PFDC and a 50/50 mixture of *cis/trans*-PFDC samples were used in the experiment. The *trans*-PFDC spectra are the result of subtracting the pure *cis*-PFDC spectra from the 50/50 mixture spectra. For this reason the error estimates on *cis*-PFDC are 3%, while for *trans*-PFDC they are 5%. The HFC-43-10-mee sample was a mixture of both *threo* and *erythro* diastereomers, with one diastereomer at 14% and the other

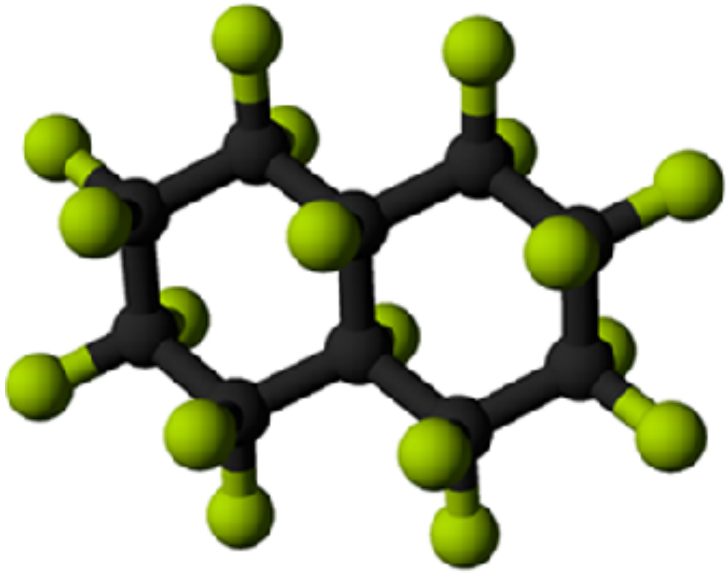

Figure 7.1: Projection image of PFDC. The green atoms are fluorine and the grey atoms are carbon. PFDC can exist as either *cis* or *trans* based on the location of the centre fluorine atoms. The *trans* conformation is shown.

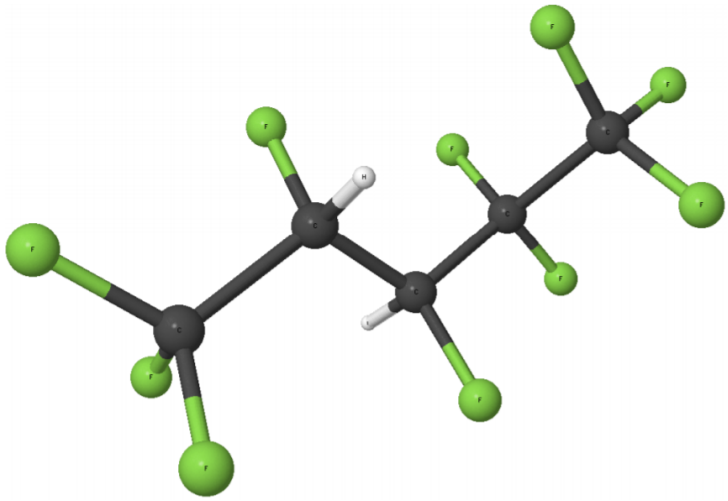

Figure 7.2: Projection image of HFC-43-10-mee. The green atoms are fluorine, the white atoms are hydrogen, and the grey atoms are carbon. HFC-43-10-mee exists as two diastereomers, *threo* and *erythro*, based on the relative positions of the hydrogen atoms. *Threo*-HFC-43-10-mee is shown.

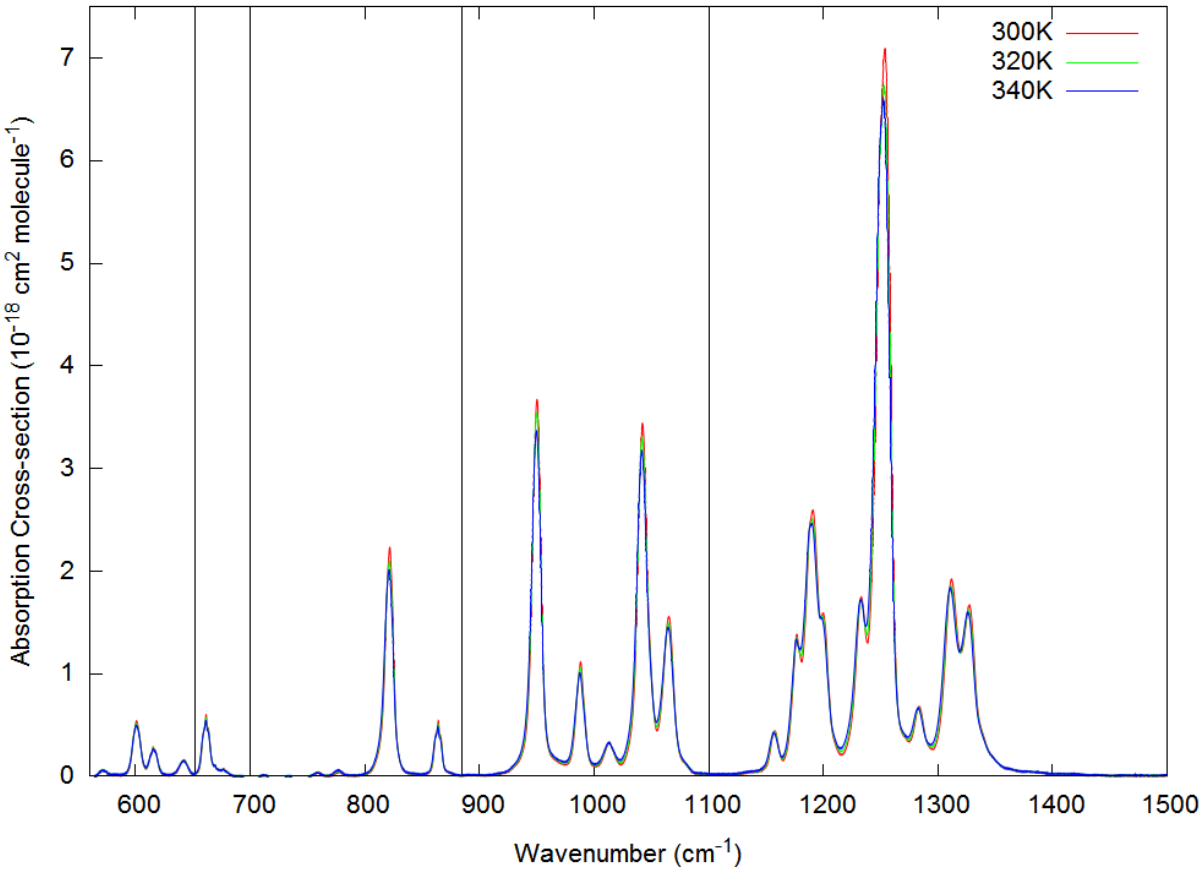

Figure 7.3: Experimental cross-section of *cis*-PFDC at three temperatures. Four absorption bands are defined from 560-652, 652-700, 700-885, 885-1100, and 1110-1500 cm^{-1}. The overall integrated band has a defined range of 560-1500 cm^{-1}.

at 86%, but the supplier was not sure which isomer was dominant. However, using well-resolved bands from the DFT calculations, *erythro*-HFC-43-10-mee was identified as the dominant isomer.

7.2 Density Functional Theory

DFT calculations were made using the B3LYP/6-311+G(2d) level of theory for PFDC. The linear relationship between experimental and theoretical vibrational mode locations was found to be: $\tilde{\nu}_{DFT} = 0.98 * \tilde{\nu}_{Exp} + 9.66$,cm^{-1}. This linear relationship is used to scale the DFT calculation below 560 cm $^{-1}$. Vibrational modes are approximated as Gaussian functions with a width of 4 cm^{-1}.

For HFC-43-10mee, DFT calculations were made using the B3LYP/6-311+G(2d,p) level of theory. A synthetic spectra was made using a 0.86:0.14 mixture ratio of *erythro* to *threo*. The DFT spectra was not linearly scaled.

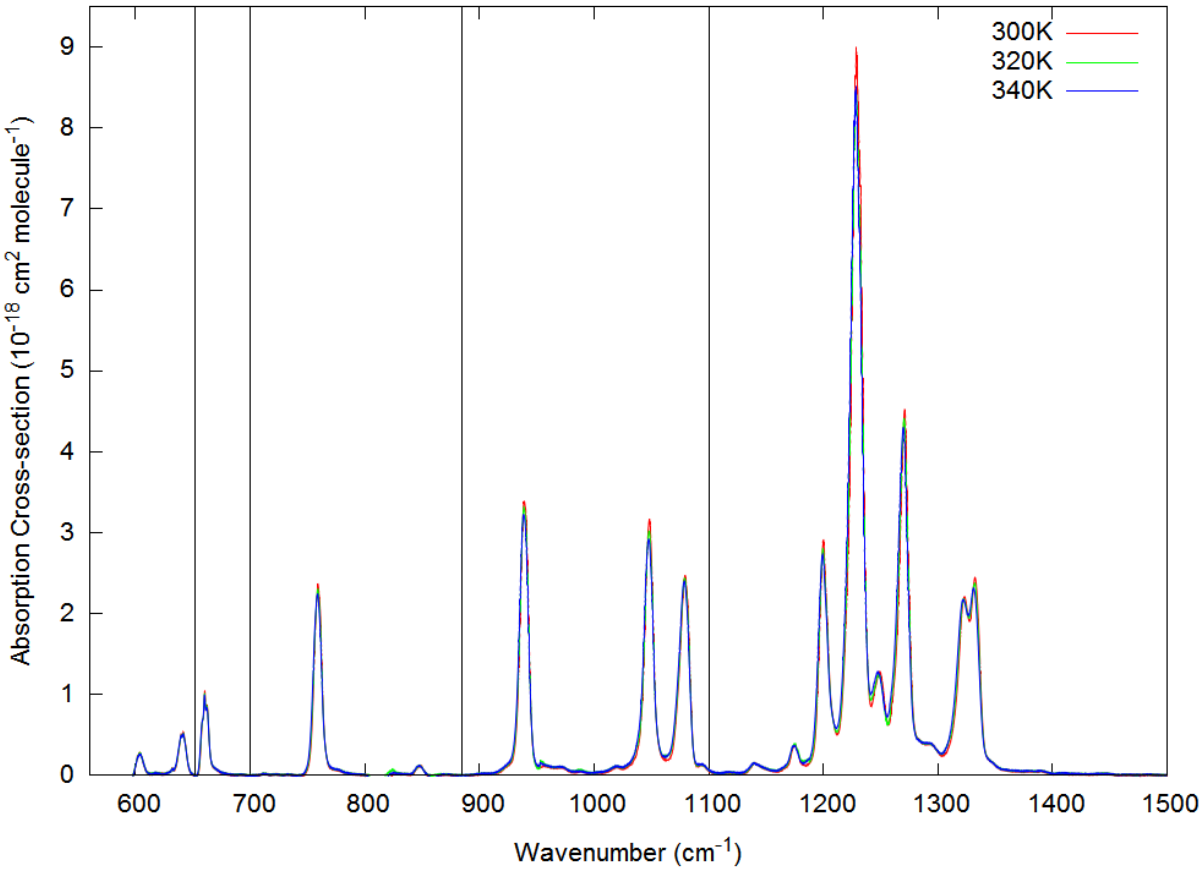

Figure 7.4: Experimental cross-section of *trans*-PFDC at three temperatures. Four absorption bands are defined from 560-652, 652-700, 700-885, 885-1100, and 1110-1500 cm^{-1}. The overall integrated band has a defined range of 560-1500 cm^{-1}.

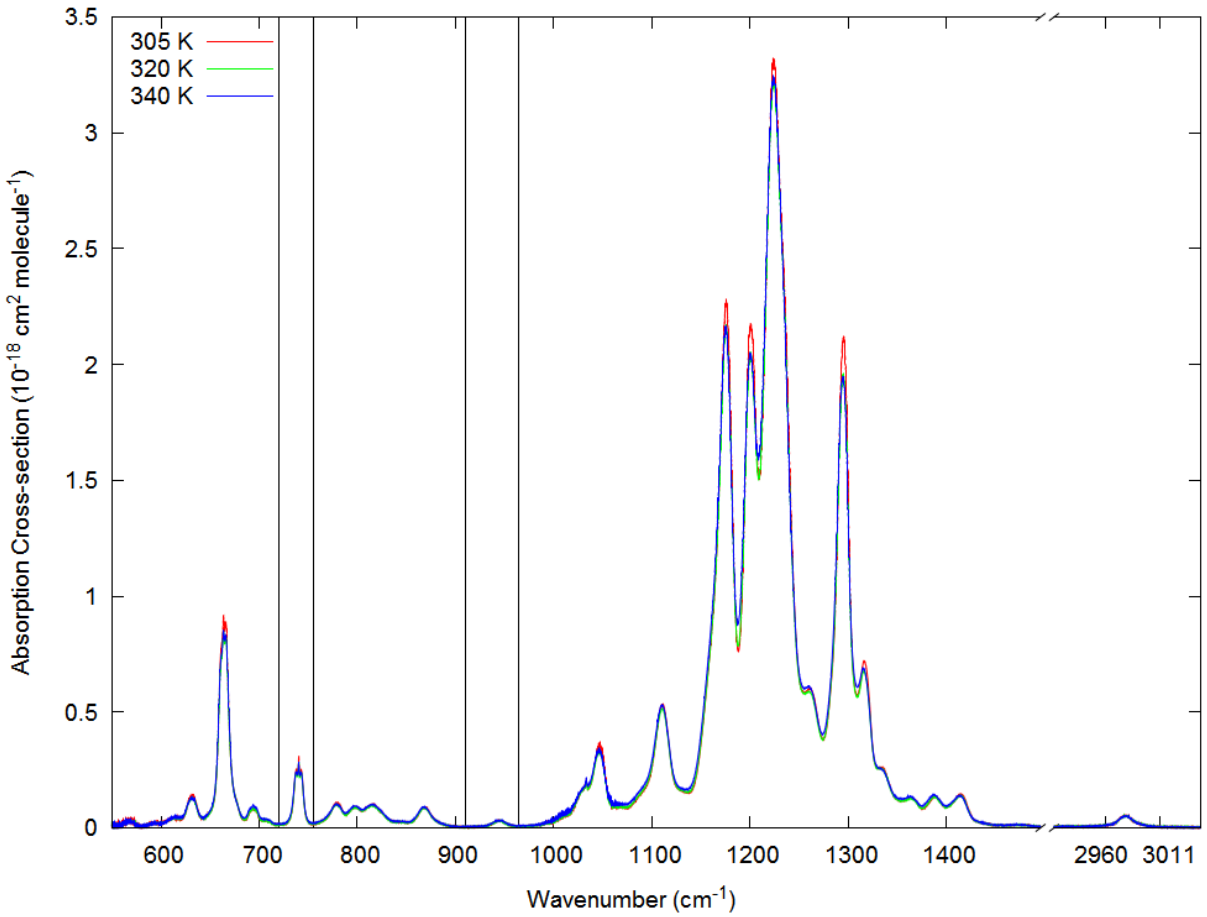

Figure 7.5: Experimental cross-section of HFC-43-10mee at three temperatures. Three absorption bands are defined from 550-975, 975-1500, and 2900-3050 cm^{-1}. The overall integrated band has a defined range of 550-3050 cm^{-1}.

7.3 Integrated Band Strength

Integrated band strengths for PFDC are included in Tables 7.1 and 7.2, along with comparisons to the DFT calculation and prior measurements made by Shine *et al.* [23]. The overall integrated band strengths in this work are larger than the previously published data in part due to the fact that Shine *et al.* [23] set their integrated cross-sections to zero outside of the defined band ranges.

Table 7.1: Published and measured integrated band strengths of *cis*-PFDC at different temperatures.

Temperature	**Integrated Band Strengths (10^{-17} cm molecule^{-1})**						
(K)	0-560 cm^{-1}	560-652 cm^{-1}	652-700 cm^{-1}	700-885 cm^{-1}	885-1100 cm^{-1}	1110-1500 cm^{-1}	Overall
296.0*			0.49	2.58	11.07	23.80	40.2
300		0.88	0.51	2.59	11.55	25.94	42.68
320		0.90	0.52	2.62	11.65	25.81	42.71
340		0.90	0.52	2.64	11.75	26.09	43.11
DFT	1.11	0.89	0.48	2.78	11.46	27.67	44.39

* Value taken from [23].

Table 7.2: Published and measured integrated band strengths of *trans*-PFDC at different temperatures.

Temperature	**Integrated Band Strengths (10^{-17} cm molecule^{-1})**						
(K)	0-560 cm^{-1}	560-652 cm^{-1}	652-700 cm^{-1}	700-885 cm^{-1}	885-1100 cm^{-1}	1110-1500 cm^{-1}	Overall
296.0*			0.68	2.02	8.75	24.19	37.9
300		0.59	0.72	2.15	9.78	27.48	42.28
320		0.58	0.75	2.32	10.08	27.66	42.98
340		0.55	0.75	2.27	10.24	28.17	43.57
DFT	1.47	0.70	0.73	2.35	10.55	29.02	44.82

* Value taken from [23].

Integrated band strengths for HFC-43-10mee are included in Table 7.3, along with comparisons to the DFT calculation and prior measurements made by PNNL [24]. The integrated band strengths in this work agree with the values from the N_2-broadened spectra from PNNL [24]. The DFT calculation is found to overestimate the integrated band strength by approximately 10%.

Table 7.3: Published and measured integrated band strengths of HFC-43-10mee at different temperatures.

Temperature (K)	**Integrated Band Strengths** (10^{-17} **cm molecule**$^{-1}$)							
	0-550 cm^{-1}	550-720 cm^{-1}	720-755 cm^{-1}	755-910 cm^{-1}	910-965 cm^{-1}	965-1600 cm^{-1}	2850-3100 cm^{-1}	Overall* (0-3100 cm^{-1})
278**		1.73	0.31	0.73	0.05	27.17	0.10	30.77±0.92
298**		1.69	0.31	0.73	0.05	28.04	0.10	31.68±0.95
305		1.70	0.32	0.77	0.07	27.24	0.20	30.97±1.09
320		1.65	0.31	0.75	0.07	26.53	0.21	30.18±1.68
323**		1.74	0.32	0.75	0.05	28.04	0.10	31.68±0.95
340		1.72	0.33	0.81	0.08	27.44	0.18	31.23±0.93
DFT	0.68	1.92	0.35	0.88	0.05	30.13	0.10	34.11

*Overall values for the experimental data include the 0-550 cm^{-1} band from the DFT mixture for the sake of comparison.

**Values taken from [24].

7.4 Radiative Efficiencies and Global Warming Potentials

A summary of *cis*-PFDC, *trans*-PFDC, and HFC-43-10mee RE and GWP calculations are given in Tables 7.4, 7.5, and 7.6 respectively. The fractional lifetime corrections and stratospheric temperature adjustments are applied to the REs before calculating GWP. PFDC is assumed to have a lifetime of 2000 years [23], whereas HFC-43-10mee has a lifetime of 16.1 years [60]. The lifetime fractional correction of PFDC follows the exponential shape, as its primary sink is photolysis in the upper atmosphere; whereas HFC-43-10mee is given the S-shaped correction, as it reacts with the OH radical in the troposphere. From the error estimates described in Section 2.6 along with the uncertainty in absorption cross-sections, the GWP has an uncertainty of ˜30% for PFDC and ˜35% for HFC-43-10mee.

Table 7.4: Summary of RE and GWP values for *trans*-PFDC at 296 K [23] and 300 K.

Data Set	**Range** (cm^{-1})	**RE**	**GWP**$_{100}$
Shine *et al.* [23]	560-1500	0.45±0.049	6290±1890
Experimental	560-1500	0.50±0.055	7060±2120
DFT	0-3000	0.58±0.081	8170±2450
Experimental+DFT	0-3000	0.53±0.058	7440±2230

Table 7.5: Summary of RE and GWP values for *cis*-PFDC at 296 K [23] and 300 K.

Data Set	**Range (cm^{-1})**	**RE**	**GWP_{100}**
Shine *et al.* [23]	560-1500	0.51±0.056	7240±2170
Experimental	560-1500	0.55±0.060	7770±2330
DFT	0-3000	0.60±0.084	8410±2520
Experimental+DFT	0-3000	0.57±0.062	8030±2410

Table 7.6: Summary of RE and GWP values for HFC-43-10mee at 298 K [24] and 300 K.

Data Set	**Range (cm^{-1})**	**RE**	**GWP_{100}**
PNNL [24]	500-3000	0.332±0.036	1385±485
Hodneborg *et al.*[7]		0.40±0.044	1650±578
Experimental	550-3000	0.329±0.036	1375±481
DFT	0-3000	0.435±0.061	1817±636
Experimental+DFT	0-3000	0.359±0.039	1410±494

Chapter 8

Conclusions and Future Work

8.1 Conclusions

8.1.1 Absorption Cross-sections

In this work, temperature-dependent absorption cross-sections of five fluorinated molecules that are radiatively active in the mid-IR spectral region were measured over a temperature range of 298-362 K. The molecules studied were PFTBA, PFPO, HFIP, PFDC, and HFC-43-10mee. Experimental absorption cross-sections were derived from FTIR spectra recorded from 530 to 3400 cm^{-1} with a resolution of 0.1 cm^{-1}. The cross-sections for these species have been submitted to the HITRAN database [31]. A summary of the temperature range, spectral range, and average integrated band strength can be found in Table 8.1.

These studies are the first ones to look at the temperature dependence of the chemicals investigated. For PFTBA, HFIP, PFDC, and HFC-43-10mee, the experimental spectral range in this work is expanded compared to previous work. Slight changes in the magnitudes of the absorption peaks are observed with changing temperature; these changes are due to a changing equilibrium mixture of stable conformers. Despite this temperature change, no changes in integrated band strengths or centroid position of the bands was observed.

8.1.2 Density Functional Theory

Theoretical DFT calculations were performed using the B3LYP method and a minimum of the 6-311++G(d,p) basis set. The calculations have simulated the spectra for different ground state configurations arising from the presence of internal rotors. As the

Table 8.1: Summary of overall experimental integrated band strengths.

Species	**Temperature Range (K)**	**Spectral Range (cm^{-1})**	**Integrated Band Strength (10^{-16} cm molecule^{-1})**
PFTBA	298.2-344.1	570-1500	7.790±0.087
PFPO	297.8-362.2	565-3040	1.96±0.10
HFIP	300.6-362.6	595-3010	2.649±0.064
PFDC	300-340	560-1500	4.283±0.074*
			4.29±0.12**
HFC-43-10mee	300-340	550-3050	3.098±0.065

*For *cis*-PFDC. **For *trans*-PFDC.

population of each configuration changes with temperature, changes in the absorption spectra occur; these differences were used to make accurate line assignments for each conformation. From this, the band positions of the theoretical spectra were calibrated to match the experimental spectra, which is assumed to also increase the accuracy of the DFT prediction outside of the experimental range. The DFT calculations for PFTBA, PFDC, and HFC-43-10mee are the first known published ones for those molecules. The DFT calculation of HFIP is at a higher level of theory compared to previously published calculations. A summary of the DFT calculations and linear scaling of each species can be found in Table 8.2.

Table 8.2: Summary of DFT calculations and linear scaling.

Species	**Basis Set**	**Slope**	**Intercept (cm^{-1})**
PFTBA	B3LYP/6-311G(d,p)	1.01±0.01	-2.44±10.4
PFPO*	B3LYP/6-311+G**	0.940 ± 0.004	80.4 ± 6.2
HFIP	B3LYP/6-311++G(3df,3pd)	0.973 ± 0.005	23.6 ± 5.8
PFDC	B3LYP/6-311+G(2d)	0.98	9.66
HFC-43-10mee	B3LYP/6-311+G(2d,p)	N/A	N/A

*DFT calculation taken from [17].

8.1.3 Radiative Efficiency and Global Warming Potential

Using the scaled DFT-calculated spectra, the wavenumber range was extended to 0 cm^{-1} when calculating radiative efficiencies and global warming potentials. When using only the experimental range, the new values agree with the previously published experimental values. However, when the range is extended to 0 cm^{-1} using the DFT spectra, the

Table 8.3: Summary of Improved RE and GWP using combined experimental and DFT cross-sections.

Species	**Lifetime (yr)**	**RE ($Wm^{-2}ppbv^{-1}$)**	**GWP**
PFTBA	500	0.803±0.106	7170±2150
	2000		7780±2330
PFPO	0.33	0.300±0.027	23.1±9.2
HFIP	1.9	0.317±0.040	203±81
trans-PFDC	2000	0.53±0.058	7440±2230
cis-PFDC	2000	0.57±0.062	8030±2410
HFC-43-10mee	16.1	0.359±0.039	1410±494

RE and GWP are increased, suggesting that the current values are underestimating the climate impacts of these species. A summary of the new RE and GWP values is shown in Table 8.3.

From the error estimates described in Section 2.6, the GWPs of PFPO and HFIP have uncertainties of ˜40%, the GWPs of PFTBA and PFDC have uncertainties of ˜30%, and the GWP of HFC-43-10mee has an uncertainty of ˜35%.

8.2 Future Work

Looking ahead, there is much that can be done with the experimental apparatus. The set-up described in Chapter 3 can remain as is to continue measuring absorption cross-sections of strongly absorbing compounds at room temperature and above. Alternatively, a coolant line could be installed around the cell to obtain spectra below room temperature. The outer vacuum jacket that surrounds the short cell has a feedthrough designed to interface with a coolant line. Thermally conductive epoxy could be used to attach a coolant line around the cell to provide thermal contact. Previous attempts to weld a coolant line to other short cells resulted in damage to the cell and a high leak rate; thus it is not advised to weld the cooling line to the short cell. A colder temperature range would be useful as a greater temperature difference could produce a greater change in spectra due to greater change in conformer ratio, which will further aid in making accurate band assignments. Colder temperatures are also more atmospherically relevant, as tropospheric temperatures decrease with altitude to as low as 220 K at the tropopause. Another possible change to the experiment could be to DC couple the detector instead of the current AC coupling. By having the detector DC coupled, it may be possible to better correct for changes in globar intensity, thus potentially removing the need for the poly-

nomial baseline adjustment described in Section 3.2.1. Regardless of possible short cell modifications, the system remains functional and can be used to continue to investigate other atmospherically relevant species listed in [7] that are lacking experimental measurements. Of particular note, the authors identified HFC-23, HFC-236ea, HFC-245ca, CCl_4, and several hydrofluoroethers as lacking suitable experimental spectra for GWP calculations.

More work is needed to complete the assembly and commissioning of the White cell before it becomes operational (see Appendix A). The D-mirrors (and possibly the T-mirror) need to be re-coated. Once this is done, the alignment and mirror mount controls need to be tested before the inner cell is moved into the outer jacket. Moving the inner cell into the outer jacket will require removing the T-mirror flange, because the size of the feedthrough makes it impossible to fit into the outer jacket while attached to the inner cell. The other challenge in moving the inner cell into position is that it will have to be lifted over the feedthrough openings as it slides into position. Once the inner cell is in place, the next step will be to align the beam path through the transfer optics tanks between the cell and spectrometer. After this, the outer jacket can be sealed and vacuum tested. Once all of this is completed successfully, the cell will be operational.

Areas of spectroscopy worth investigating with the system can be either improving the spectra of interfering gases in terrestrial retrievals or making CO_2 broadening measurements to aide with planetary missions. For example, the ACE satellite requires improvements to H_2O, $COCl_2$, HNO_4, HNO_3, and Rosenkranz line mixing parameters for CH_4. Instruments on missions to Venus and Mars, such as Solar Occultation at Infrared (SOIR) and Nadir and Occultation for MArs Discovery (NOMAD), require improved broadening coefficients to improve detections of various species such as CO_2, CO, O_3, CH_4 (and isotopes), C_2H_2, C_2H_4, C_2H_6, H_2CO, SO_2, H_2S, and HCl [64].

Appendices

Appendix A

White Cell

A.1 System Description

This appendix summarizes the commissioning of the lab's White cell that was done as part of this work. A schematic diagram of the intended configuration of the White cell is shown in Figure A.1. The purpose of the White cell is to detect weak absorption lines by having a long and adjustable active pathlength of the beam through the gas sample. This long pathlength is achieved by placing mirrors at the far ends of the cell and having the light beam bounce repeatedly between the mirrors, resulting in a pathlength much longer than the length of the cell. Mirrors 1 and 2 in Figure A.1 are known as the D-mirrors, while mirror 3 is known as the T-mirror. The D- and T-mirrors are spherical mirrors and have matching radii of curvature such that the light beam can bounce repeatedly between them. The radius of curvature was measured experimentally in the Space Instrument Characterization Facility clean room to be 200.2±0.3 cm [61]. The D- and T-mirrors have a gold coating that should give them a theoretical reflectivity of 98% [61]. Mirrors 4 and 5 are identical parabolic mirrors from B-Con Engineering Inc.. They also have a gold coating, but also have a protective layer that reduces reflectivity by 1%. Additional specifications of the parabolic mirrors are an outer diameter of 3.75", an effective focal length of 52.55", and a centre height of 2.5". Mirror 7 is another parabolic mirror, but with an outer diameter of 9.6 cm and an effective focal length of 32.4 cm. Mirror 7 has an aluminium coating.

Unlike the short cell, which is optically coupled to the DA8 spectrometer, the White cell is coupled to the emission port on the side due to space restrictions. The transfer optics tanks serve to direct the beam from the Bomem DA8 FTIR into the cell and back out towards the detector. Similar to the short cell system, the inner cell of the White cell system is supported inside the outer jacket in order to isolate it from the outside

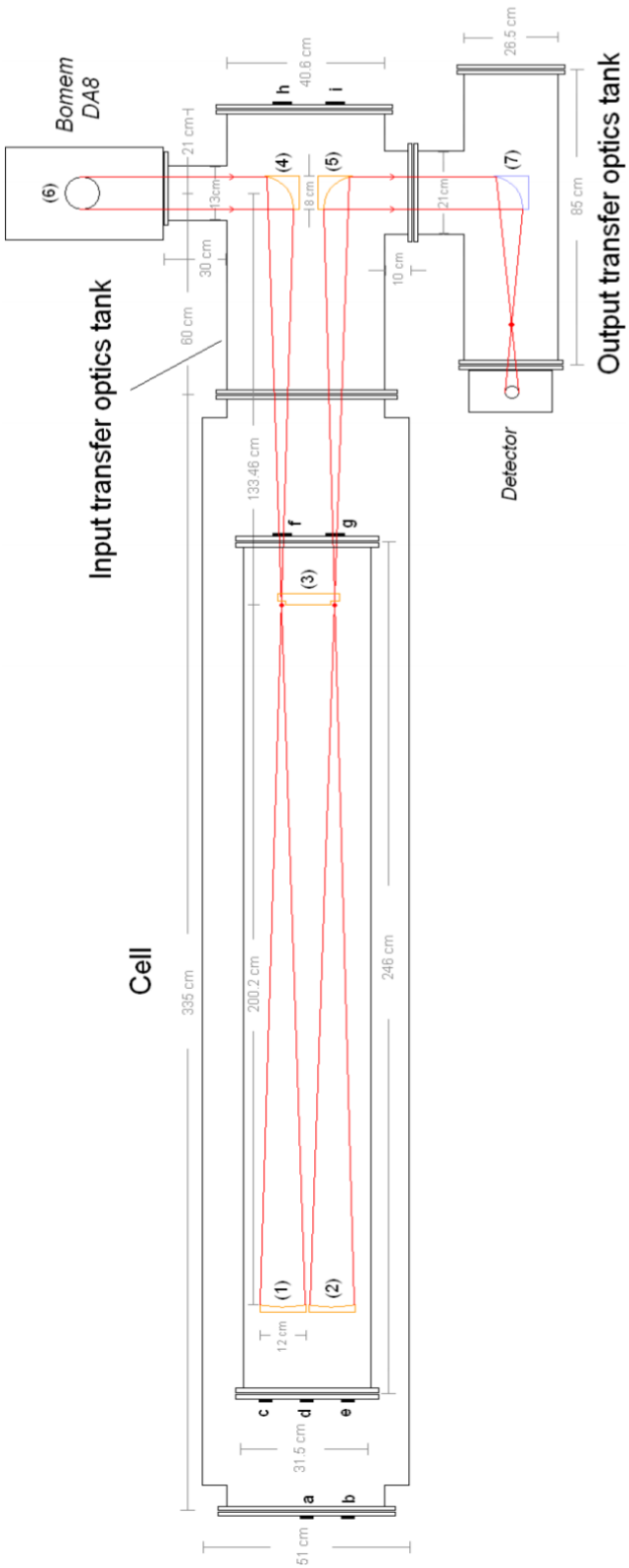

Figure A.1: A schematic diagram of the White cell currently under construction. Image taken from [61].

environment and to properly align the spectrometer beam path through the system.

A.2 Mirrors and Mounts

Since September 2012, much work has been done on construction and assembly of the system. To begin with, the mounts holding mirrors 4 and 5 were not initially made to the correct dimensions and had to be shortened. Additionally, the D-mirror holder also required several modifications that have since been completed; these included installing stronger support springs and adding a clamping mechanism to hold the mount in place. The D- and T-mirror positions are controlled using New Focus Inc. picomotors. One motor on the D-mirror mount was found to be under excessive pressure and was unable to work as intended. In order to get the D-mirror mount to function correctly, several steps were taken: metal rod bearings were replaced with Teflon rods and grease was added to lower the friction in the system, the springs were replaced with weaker springs, and additional spring mounts were added in other locations on the mirror mount. These added springs provided the restoring force needed to return the mirror to a previous position, but spread the pressure such that no motor is over strained and all can function properly. The motors for the mirror mounts have all been wired up and tested. A switch box was purchased to control the multiple picomotors. Unfortunately there does not appear to be a way to record the positions of each motor, so any adjustments will have to be done independently each time.

Continuing the subject of mirrors, mirror 6 had not been ordered and has since been purchased from Tower Optical Corporation. A design for a mount for mirror 6 was provided by Bomem (Figure A.3) and built; the assembled mount along with mirror 6 is shown in Figure A.4. Two of the 3 D-mirrors them have spots on them indicating that the coating has degraded. This can be seen in Figure A.2. The company that originally made the mirrors no longer provides the services required. Discussions with Dr. James Drummond suggest that all that is required is re-coating the mirrors and that re-polishing would be unnecessary as long as the experimental range is in the IR. The T-mirrors appear to be fine.

A.3 Vacuum Chambers and Pumping Systems

The square flange connecting the input transfer optics tank to the DA8 has been welded in place to the transfer optic tank such that a vacuum sealed connection to the DA8 spectrometer is now possible. The transfer optics tanks, along with their placement next

Figure A.2: D-mirror showing signs of coating degradation.

to the DA8, are shown in Figure A.5. A new Turbo-701 Navigator pump needed to replace an aged unit and vacuum pumping components were ordered. The turbo pump was connected to the inner cell via a gatekeeper valve and a DS602 1PH rotary vane pump. In addition to aiding the turbo pump in pumping down the inner cell, the rotary pump also connects directly to the outer cell to pump the outer jacket down as well. A pumping feedthrough connection between the inner and outer cells was designed and the parts were ordered and arrived. A photograph of the inner-cell vacuum pump system attachment is shown in Figure A.6. Some of the missing vacuum components that were ordered had to be sent to the machine shop to be welded together so that they could interface with the current components, such as the gas injection line, which has since been welded to the outer flange.

The raisers previously installed on the inner cell that control the position of the inner cell inside the outer jacket were too small, resulting in the inner cell being too low for the incoming laser beam alignment. The inner cell is now being supported with a yoke, the design of which is shown in Figure A.7. While the yoke has strength and stability, it does not have a method to fine tune the height adjustment; height adjustment will have to be done with thin shims.

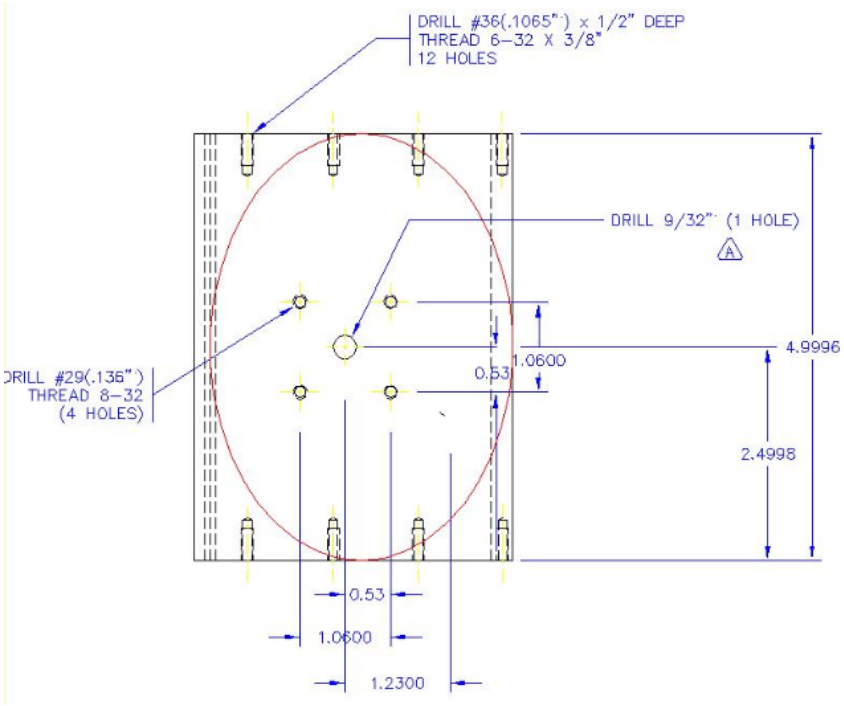

(a) Top-view

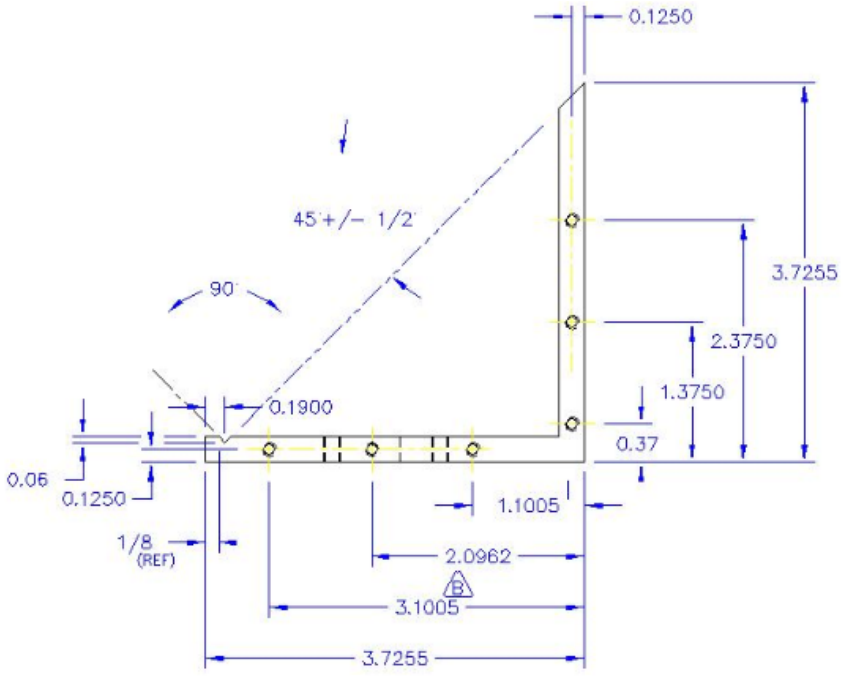

(b) Side-view

Figure A.3: Mount for the flat mirror. Units are in inches. Images provided by ABB Bomem Inc.

Figure A.4: Mounted flat mirror 6.

A.4 Temperature Control

The twelve thermocouples for the inner layer of the inner cell have been wired and attached to the brackets for the inner cell. The sixteen outer layer thermocouples have been attached using a thermally conductive epoxy. Both inner and outer layer thermocouples have been tested and all agree with each other to within ±1 K. A Johns Manville Cryo-Lite cryogenic blanket was ordered to insulate the cell and has been installed around the inner cell. Components for the coolant fluid feedthrough were ordered and have been welded together by the machine shop. The coolant fluid feedthrough system has been assembled and tested. No leaks were found anywhere on the piping and connections that will be inner side of the outer jacket.

A.5 Assembly

Assembling the inner cell requires fixing the end flanges to a bench, then rolling the inner cell into position; this is because there is too much torque on the flanges to simply mount them by hand without damaging the mirrors. An image of the assembled D-mirror mount

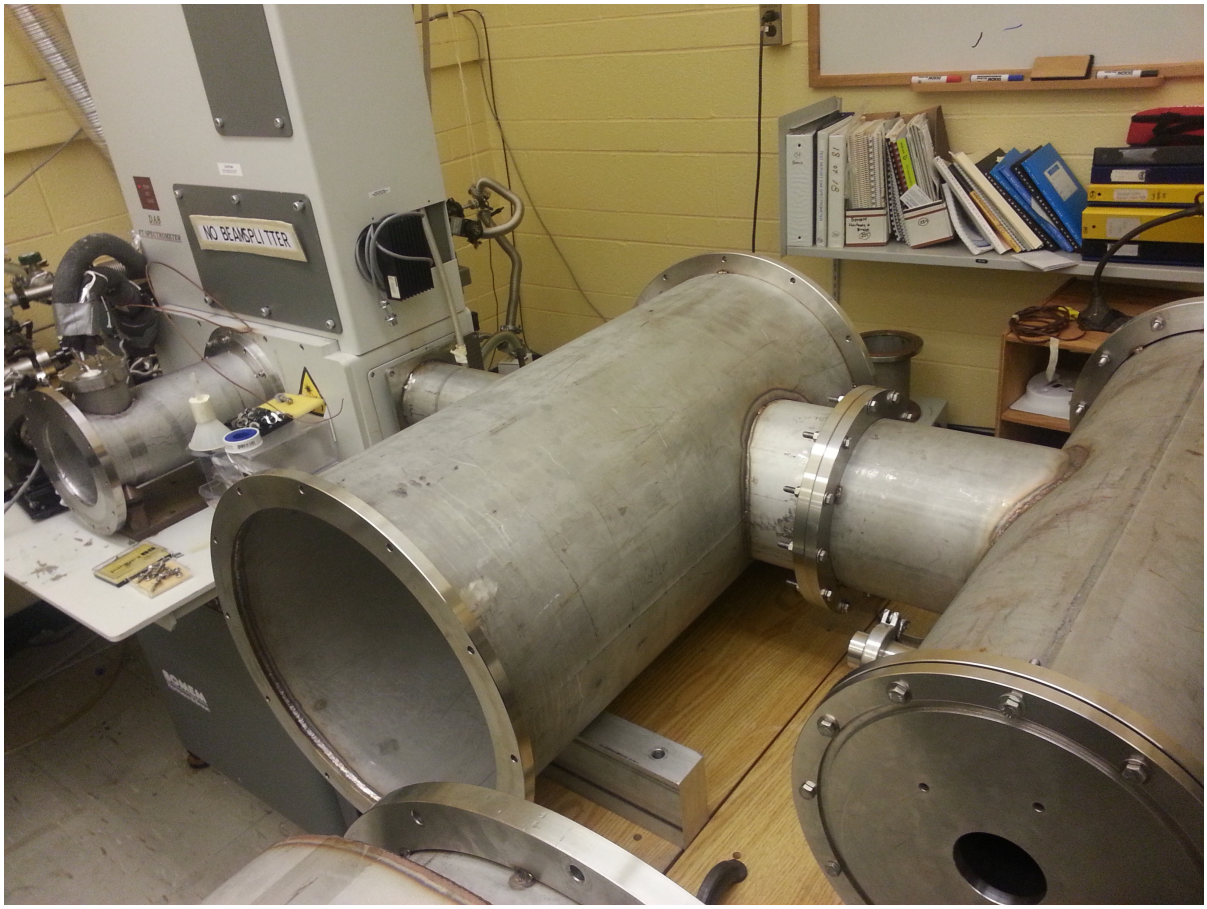

Figure A.5: Assembled transfer optics tanks. The square flange that connects the input transfer optics tank to the DA8 has been welded to the tank.

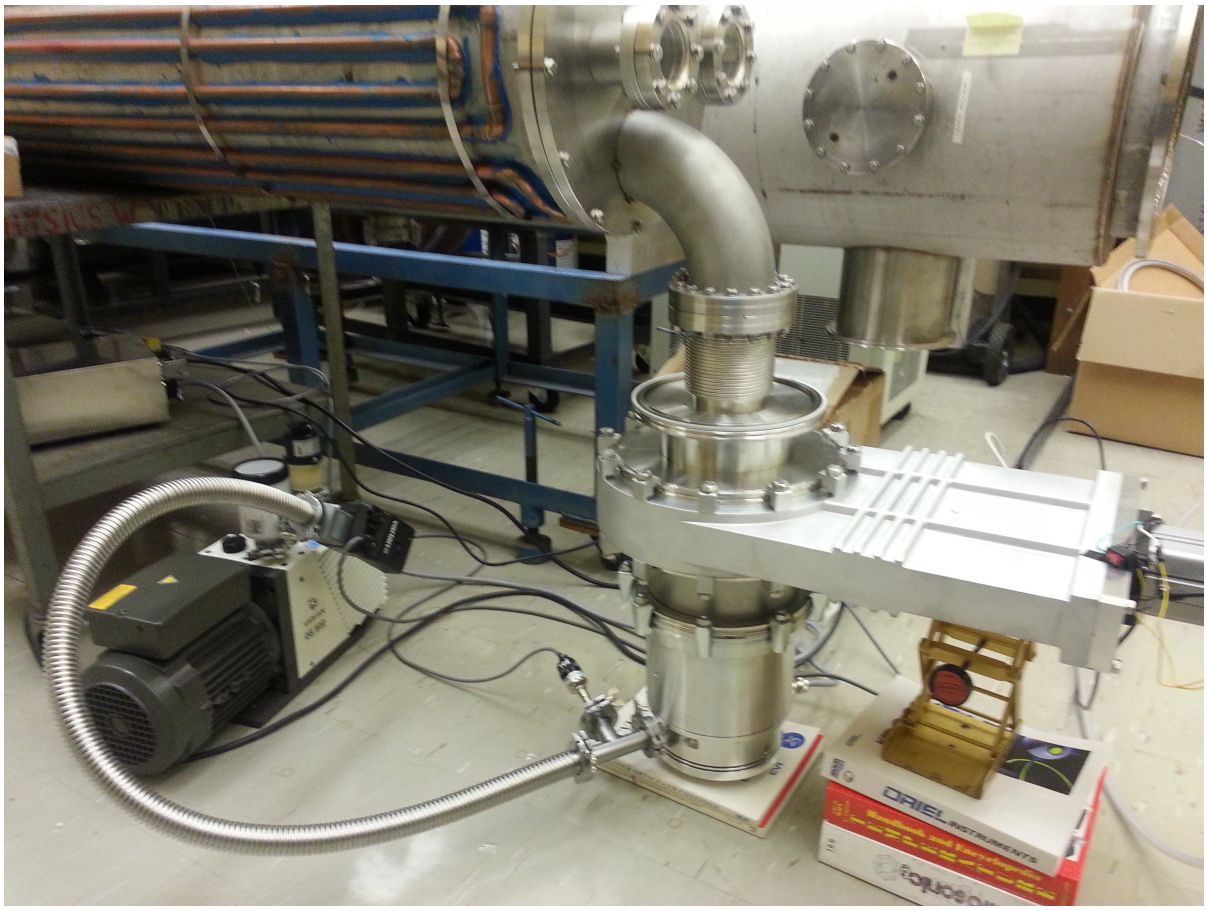

Figure A.6: Inner cell with vacuum pump feedthrough attachment.

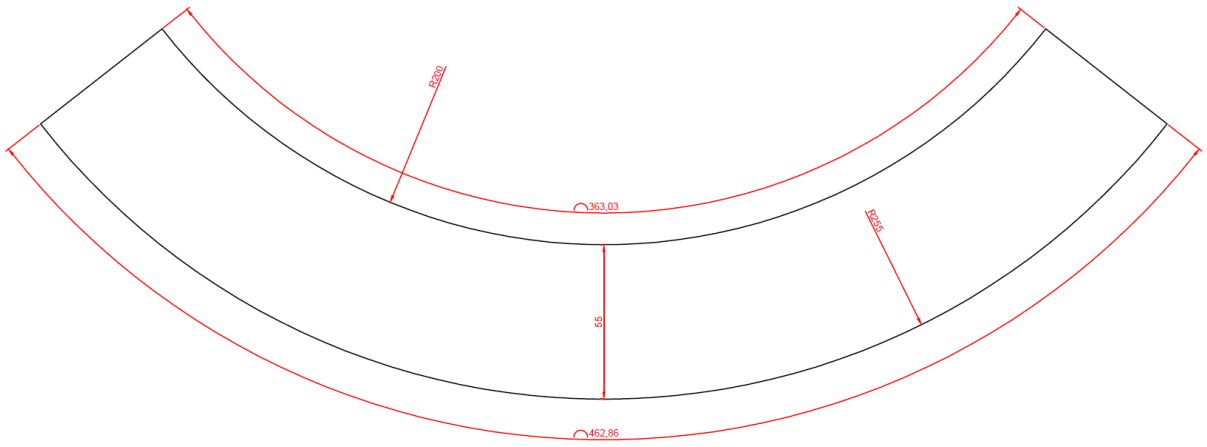

Figure A.7: Design of the yoke used to support the inner cell. Units are in mm.

being attached to the inner cell is shown in Figure A.8. Once the cell was assembled, the system was pumped down and testing of the alignment started. A laser pointer was mounted and used to follow the White cell alignment guide provided by Dr. Keeyoon Sung [62]; a diagram from [62] showing the expected beam path is shown in Figure A.9. Four reflections are required to get the beam from the spectrometer to the detector, not counting the multiple reflections between the D- and T-mirrors. It has been confirmed in the Space Instrument Characterization Facility clean room that it is possible to get twenty five reflections [61]. The picomotors of the D- and T-mirror mounts can be used to fine tune their positions. This allows the number of reflections to be varied to change the pathlength. In initial tests, two reflections were obtained but then the limit of the motor position was reached and the mirror slipped off the mount, requiring the system to be reopened. The T-mirror mount is quite restrictive in its movement and it might be worth adding an additional degree of freedom to this mirror mount.

A vacuum test of the inner cell was also performed, identifying one leak that has since been sealed. The inner cell achieves pressures on the order of 10^{-7} Torr. If the pump is turned off and the gatekeeper valve is sealed, the pressure inside the cell remains stable; rising up to 10^{-3} Torr over four days.

As of this writing, the remaining outstanding jobs to make the White cell operational are re-coating the D-mirrors, resealing the inner cell, confirming D- and T-mirror operation, inserting the inner cell into outer jacket, and overall optical alignment. Once assembly is complete, the system should be calibrated by taking a spectrum of a well-studied gas and confirming the accuracy of the spectrum produced compared to the literature.

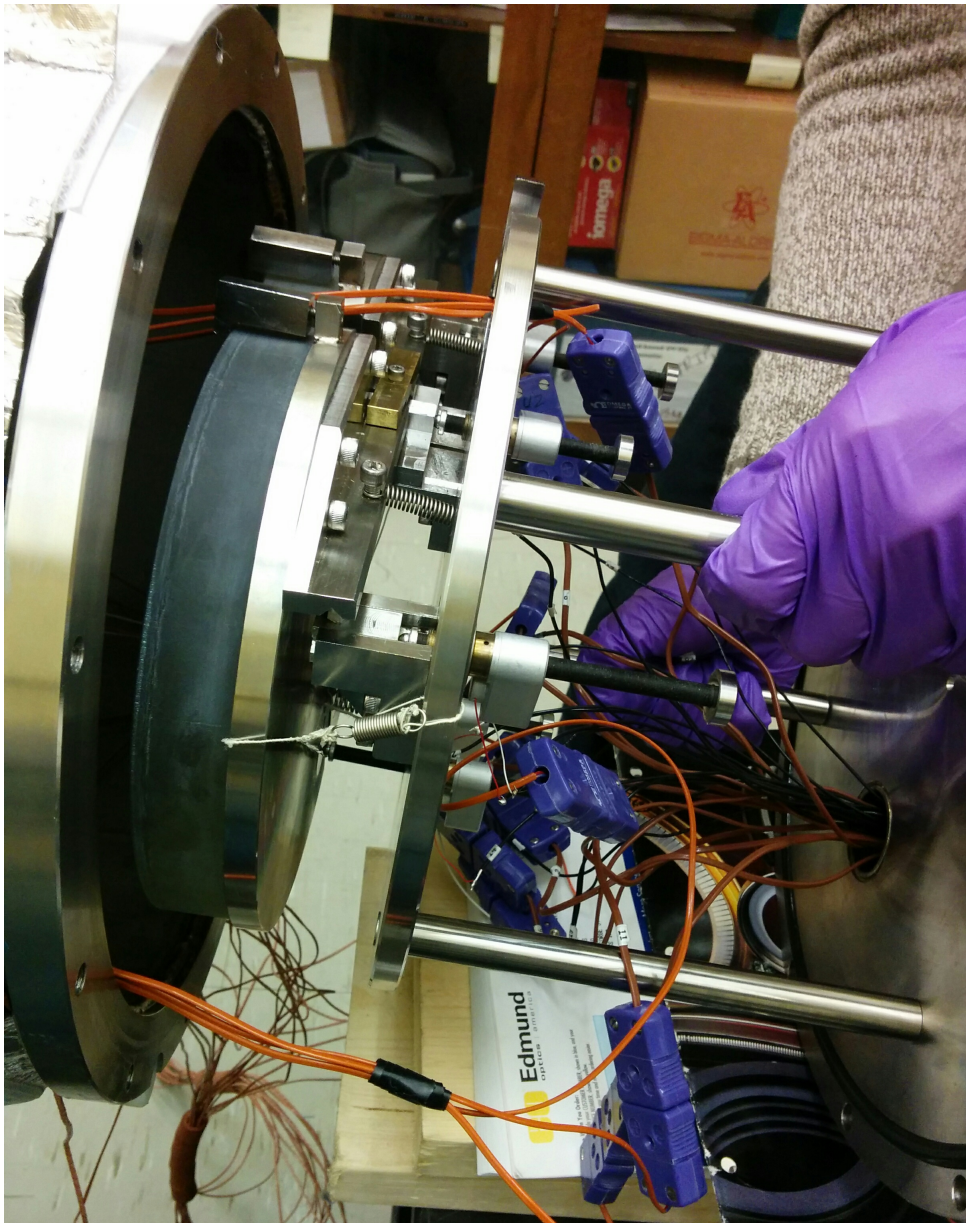

Figure A.8: Assembled D-mirror mount being attached to the inner cell. Black wires are connected to the picomotors. The orange wires with purple clips are the K-type thermocouples.

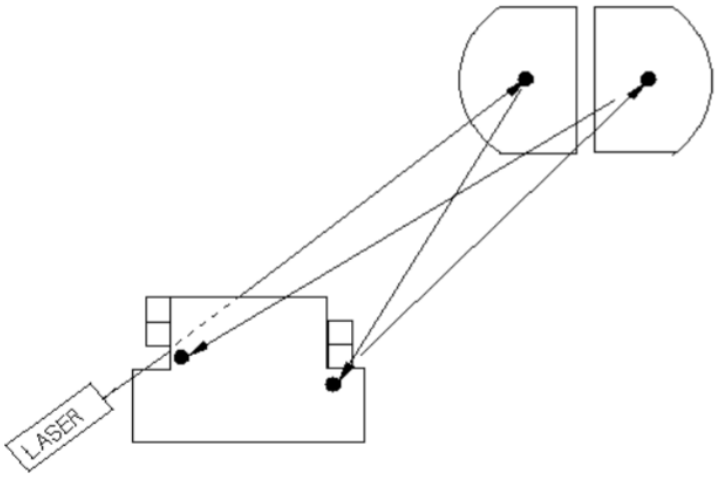

Figure A.9: Beam path for alignment of the White cell. Image taken from [62].

Bibliography

[1] S. Gupta, D. A. Tirpak, N. Burger, J. Gupta, N. Hhne, A. I. Boncheva, G. M. Kanoan, C. Kolstad, J. A. Kruger, A. Michaelowa, S. Murase, J. Pershing, T. Saijo, A. Sari, Policies, Instruments and Co-operative Arrangements. In Climate Change 2007: Mitigation. Contribution of Working Group III to the Fourth Assessment Report of the Intergovernmental Panel on Climate Change [B. Metz, O.R. Davidson, P.R. Bosch, R. Dave, L.A. Meyer (eds.)], *Cambridge University Press*, p.747-807 (2007).

[2] B. Metz, L. Kuijpers, S. Solomon, S. O. Andersen, O. Davidson, J. Pons, D. de Jager, T. Kestin, M. Manning, and L. Meyer, Safeguarding the Ozone Layer and the Global Climate System: Issues Related to Hydrofluorocarbons and Perfluorocarbons, *Cambridge University Press*, 180pp (2005).

[3] Montreal Protocol, http://ozone.unep.org/en/treaties-and-decisions/montreal-protocol-substances-deplete-ozone-layer, accessed 01/04/2017.

[4] N. Nakićenović, J. Alcamo, G. Davis, B. de Vries, J. Fenhann, S. Gaffin, K. Gregory, A. Griibler, T. Yong Jung, T. Kram, E. Lebre La Rovere, L. Michaelis, S. Mori, T. Morita, W. Pepper, H. Pitcher, L. Price, K. Riahi, A. Roehrl, H.-H. Rogner, A. Sankovski, M. Schlesinger, P. Shukla, S. Smith, R. Swart, S. van Rooijen, N. Victor, and Z. Dadi, Special Report on Emissions Scenarios, *Cambridge University Press*, p.1-20 (2000).

[5] P. Forster, V. Ramaswamy, P. Artaxo, T. Berntsen, R. Betts, D.W. Fahey, J. Haywood, J. Lean, D.C. Lowe, G. Myhre, J. Nganga, R. Prinn, G. Raga, M. Schulz and R. Van Dorland, 2007: Changes in Atmospheric Constituents and in Radiative Forcing. In: Climate Change 2007: The Physical Science Basis. Contribution of Working Group I to the Fourth Assessment Report of the Intergovernmental Panel on Climate Change [Solomon, S., D. Qin, M. Manning, Z. Chen, M. Marquis, K.B. Averyt, M.Tignor and H.L. Miller (eds.)]. *Cambridge University Press*, p.131-234 (2007).

[6] G. Myhre, D. Shindell, F.-M. Bron, W. Collins, J. Fuglestvedt, J. Huang, D. Koch, J.-F. Lamarque, D. Lee, B. Mendoza, T. Nakajima, A. Robock, G. Stephens, T. Takemura and H. Zhang, 2013: Anthropogenic and Natural Radiative Forcing Supplementary Material. In: Climate Change 2013: The Physical Science Basis. Contribution of Working Group I to the Fifth Assessment Report of the Intergovernmental Panel on Climate Change [Stocker, T.F., D. Qin, G.-K. Plattner, M. Tignor, S.K. Allen, J. Boschung, A. Nauels, Y. Xia, V. Bex and P.M. Midgley (eds.)], p.659-740, Available from www.climatechange2013.org and www.ipcc.ch (2013).

[7] O. Hodnebrog, M. Etminan, J. S. Fuglestvedt, G. Marston, G. Myhre, C. J. Nielsen, K. P. Shine, and T. J. Wallington, Global warming potentials and radiative efficiencies of halocarbons and related compounds: A comprehensive review, *Rev. Geophys.*, **51**, 2, 300-378 doi:10.1002/rog.20013 (2013).

[8] I. Bravo, Y. Díaz-de-Mera, A. Aranda, E. Moreno, D. R. Nutt, and G. Marston, Radiative efficiencies for fluorinated esters: indirect global warming potentials of hydrofluoroethers, *Phys. Chem. Chem. Phys.*, **13**, 17185-17193 (2011).

[9] I. Bravo, A. Aranda, M. D. Hurley, G. Marston, D. R. Nutt, K. P. Shine, K. Smith, and T. J. Wallington, Infrared absorption spectra, radiative efficiencies, and global warming potentials of perfluorocarbons: Comparision between experiment and theory, *J. Geophys. Res.*, **115**, D24317, doi:10.1029/2010JD014771 (2010).

[10] P. Blowers, D. M. Moline, K. F. Tetrault, R. R. Wheeler, and S. L. Tuchawena, Prediction of radiative forcing values for hydrofluoroethers using density functional theory methods, *J. Geophys. Res. Atmos.*, **112**, D15108, doi:10.1029/2006JD008098 (2007).

[11] C. Boone, *ACE-FTS Retrievals and Processing*, ACE Science Team Meeting #28 (2013).

[12] J. U. White, Long Optical Paths of Large Aperture, *J. Opt. Soc. Am.*, **32**, 285-288 (1942).

[13] A. C. Hong, C. J. Young, M. D. Hurley, T. J. Wallington, and S. A. Mabury, Perfluorotributylamine: A novel long-lived greenhouse gas, *Geophys. Res. Lett.*, **40**, 1-6 (2013).

[14] R. Imasu, A. Suuga, and T. Matsuno, Radiative Effects and Halocarbon Global Warming Potentials of Replacement Compounds for Chlorofluorocarbons, *J. Meteorological Soc. Japan*, **73**, 6, 1123-1136 (1995).

[15] S. R. Sellevåg, B. D'Anna, and C. J. Nielsen, Infrared Absorption Cross-Sections and Estimated Global Warming Potentials of $CF_3CH_2CH_2OH$, $CHF_2CF_2CH_2OH$, $CF_3CF_2CH_2OH$, $CF_3CHFCF_2CH_2OH$, and $CF_3CF_2CF_2CH_2OH$, *Asian Chem. Lett.*, **11**, 1 and 2, 33-40 (2007).

[16] M. Antiñolo, S. González, B. Ballesteros, J. Albaladejo, and E. Jiménez, Laboratory Studies of $CHF_2CF_2CH_2OH$ and $CF_3CF_2CH_2OH$: UV and IR Absorption Cross Sections and OH Rate Coefficients between 263 and 358 K, *J. Phys. Chem. A*, **116**, 6041-6050, doi:10.1021/jp2111633 (2012).

[17] H. M. Badawi and W. Fömer, Solvent dependence of conformational stability and analysis of vibrational spectra of 2,2,3,3,3-pentafluoro-1-propanol, *Spectrochimica Acta*, **71A**, 388-397 (2008).

[18] A. J. Barns and J. Murto, Infra-red Cryogenic Studies Part 10 Conformational Isomerism of 1,1,1,3,3,3,-Hexafluoropropan-2-ol, *J. Chem. Soc. Faraday*, **2**, 68, 1642-1651 (1972).

[19] J. Murto, A. Kivinen, R. Viitala, and J. J. Hyämäki, Fluoroalcohols Part 20 Infrared and Raman spectra of hexafluoro-2-propanol and its deuterated analogues, *Spectrochimica Acta*, **29A**, 1121-1137 (1973).

[20] J. Murto, A. Kivinen, M. Näsäkkälä, R. Viitala, and J. Hyämäki, Fluoroalcohols Part 19 Infrared and Raman spectra of hexafluoro-2-propanol and its deuterated analogues in solution, *Suomen Kemistilehti B*, **46**, 76-83 (1973).

[21] J. R. Durig, R. A. Larsen, B. J. Van Der Veken, and F. O. Cox, Raman and far-infrared spectra of gaseous 1,1,1,3,3,3-hexafluoro-2-propanol, conformational stability and barriers to internal rotation, *J. Mol. Struc.*, **172**, 183-201 (1988).

[22] B. Czarnik-Matusewicz, S. Pilorz, D. Bienko, and D. Michalska, Molecular and electronic structures, infrared spectra, and vibrational assignment for *ap* and *sc* conformers of hexafluoro-iso-propanol, *Vib. Spec.*, **47**, 44-52 (2008).

[23] K. P. Shine, L. K. Gohar, M. D. Hurley, G. Marston, D. Martin, P. G. Simmonds, T. J. Wallington, M. Watkins, Perfluorodecalin: Global warming potential and first detection in the atmosphere, *Atmos. Environ.* **39**, 1759-1763 (2005).

[24] S. W. Sharpe, T. J. Johnson, R. L. Sams, P. M. Chu, G. C. Rhoderick, and P. A. Johnson, Gas-Phase Databases for Quantitative Infrared Spectroscopy, *Appl. Spectrosc.*, **58**, 12, 1452-1461 (2004).

[25] B. H. Bransden and C. J. Joachain, Physics of Atoms and Molecules, *Prentice Hall*, 477-548 (2003).

[26] M. Born and J. R. Oppenheimer, Zur Quantentheorie der Molekeln [On the Quantum Theory of Molecules], *Annalen der Physik*, **389**, 20: 457-484, doi:10.1002/andp.19273892002 (1927).

[27] J. M. Wallace and P. V. Hobbs, Atmospheric Science: An Introductory Survey, *Academic Press*, p.128-129 (2006).

[28] D. Lisak, J. T. Hodges, and R. Ciurylo, Comparison of semiclassical line-shape models to rovibrational H_2O spectra measured by frequency-stabilized cavity ring-down spectroscopy, *Phys. Rev. A*, **73**, 012507 (2006).

[29] L. Galatry, Simultaneous Effect of Doppler and Foreign Gas Broadening on Spectral Lines, *Phys. Rev.*, **122**, 1218-1223 (1961).

[30] M. Nelkin and A. Ghatak, Simple Binary Collision Model for Van Hove's $G_s(r,t)$, *Phys. Rev.*, **135**, A4 (1964).

[31] L. S. Rothman, I. E. Gordon, Y. Babikov, A. Barbe, D. C. Benner, P. F. Bernath, M. Birk, L. Bizzocchi, V.Boudon, L. R. Brown, A. Campargue, K. Chance, E. A. Cohen, L. H. Coudert, V. M. Devi, B. J. Drouin, A. Fayt, J.-M. Flaud, R. R. Gamache, J. J. Harrison, J.-M. Hartmann, C. Hill, J. T. Hodges, D. Jacquemart, A. Jolly, J. Lamouroux, R. J. Le Roy, G. Li, D. A. Long, O. M. Lyulin, C. J. Mackie, S. T. Massie, S. Mikhailenko, H. S. P. Mller, O. V. Naumenko, A. V. Nikitin, J. Orphal, V.Perevalov, A. Perrin, E. R. Polovtseva, C. Richard, M. A. H. Smith, E. Starikova, K. Sung, S. Tashkun, J. Tennyson, G. C. Toon, VI. G. Tyuterev, and G. Wagner, The HITRAN 2012 Molecular Spectroscopic Database, *J. Quant. Spectrosc. Rad. Transfer*, **130**, 4-50, https://doi.org/10.1016/j.jqsrt.2013.07.002 (2013).

[32] N. H. Ngo, D. Lisak, H. Tran, and J.-M. Hartmann, An isolated line-shape model to go beyond the Voigt profile in spectroscopic databases and radiative transfer codes, *J. Quant. Spectrosc. Rad. Transfer*, **129**, 89-100, doi:10.1016/j.jqsrt.2013.05.034 (2013).

[33] D. A. Long, K. Bielska, D. Lisak, D. K. Havey, M. Okumura, C. E. Miller, and J. T. Hodges, The air-broadened, near-infrared CO2 line shape in the spectrally isolated

regime: Evidence of simultaneous Dicke narrowing and speed dependence, *J. Chem. Phys.*, **135**, 064308, doi:10.1063/1.3624527 (2011).

[34] P. W. Rosenkranz, Shape of the 5 mm oxygen band in the atmosphere, *IEEE Trans. Antennas Propag.*, **23**, 498-506 (1975).

[35] R. J. Bell, Introductory Fourier Transform Spectroscopy, *Academic Press*, p.33-68 (1972).

[36] R. G. Parr and Y. Weitao, Density-Functional Theory of Atoms and Molecules, *Oxford University Press*, p.3-66 (1989).

[37] P. Atkins and R. Friedman, Molecular Quantum Mechanics 4th ed., *Oxford University Press*, p.287-339 (2005).

[38] S. Pinnock, M. D. Hurley, K. P. Shine, T. J. Wallington, and T. J. Smyth, Radiative forcing of climate by hydrochlorofluorocarbons and hydrofluorocarbons, *J. Geophys. Res.*, **100**(D11), 23227-23238 (1995).

[39] M. C. Abrams, G. C. Toon, and R. A. Schindler, Practical example of the correction of Fourier-transform spectra for detector nonlinearity, *Appl. Opt.*, **33**, 6307-6314, doi:10.1364/AO.33.006307 (1994).

[40] T. J. Johnson, R. L. Sams, T. A. Blake, S. W. Sharpe, and P. M. Chu, Removing aperture-induced artifacts from Fourier transform infrared intensity values, *Appl. Opt.*, **41**, 2831-2839, doi:10.1364/AO.41.002831 (2002).

[41] K. Le Bris and L. Graham, Quantitative comparisons of absorption cross-section spectra and integrated intensities of HFC-143a, *J. Quant. Spectrosc. Rad. Transfer*, **151**, 13-17 doi:10.1016/j.jqsrt.2014.09.005 (2015).

[42] K. Le Bris, K. Strong, S. M. L. Melo, and J. C. Ng, Structure and conformational analysis of CFC-113 by density functional theory calculations and FTIR spectroscopy, *J. Mol. Spec.*, **243**, 178-183 (2007).

[43] K. Le Bris and K. Strong, Temperature-dependent cross-section spectra of HCFC-142b, *J. Quant. Spectrosc. Rad. Transfer*, **111**, 364-371, doi:10.1016/j.jqsrt.2009.10.005 (2010).

[44] K. Le Bris, R. Pandharpurkar, and K. Strong, Mid-infrared absorption cross-sections and temperature dependence of CFC-113, *J. Quant. Spectrosc. Rad. Transfer*, **112**, 1280-1285 (2011).

[45] K. Le Bris, J. McDowell, and K. Strong, Measurements of the infrared absorption cross-sections of CH_3CFCl_2 (HCFC-141b), *J. Quant. Spectrosc. Rad. Transfer*, **113**, 1913-1919 (2012).

[46] P. Godin, A. Cabaj, S. Conway, A. C. Hong, K. Le Bris, S. A. Mabury, and K. Strong, Temperature-dependent absorption cross-sections of perfluorotributylamine, *J. Mol. Spec.*, **323**, 53-58, doi:10.1016/j.jms.2015.11.004 (2015).

[47] P. J. Godin, A. Cabaj, L.-H. Xu, K. Le Bris, and K. Strong. A study of the temperature dependence of the infrared absorption cross-sections of 2,2,3,3,3-pentafluoropropanol in the range of 298-362 K, *J. Quant. Spectrosc. Rad. Transfer*, **186**, 150-157, doi:10.1016/j.jqsrt.2016.05.031, (2016).

[48] K. E. Atkinson, An Introduction to Numerical Analysis (2nd ed.), *John Wiley and Sons*, ISBN 978-0-471-50023-0 (1989).

[49] M. G. Costello, R. M. Flynn, and J. G. Owens, Fluoroethers and Fluoroamines, *John Wiley and Sons, Inc.*, 877-888, doi:10.1002/0471238961.0612211506122514.a01.pub2 (2004).

[50] M. J. Frisch, G. W. Trucks, H. B. Schlegel, G. E. Scuseria, M. A. Robb, J. R. Cheeseman, J. A. Montgomery, Jr., T. Vreven, K. N. Kudin, J. C. Burant, J. M. Millam, S. S. Iyengar, J. Tomasi, V. Barone, B. Mennucci, M. Cossi, G. Scalmani, N. Rega, G. A. Petersson, H. Nakatsuji, M. Hada, M. Ehara, K. Toyota, R. Fukuda, J. Hasegawa, M. Ishida, T. Nakajima, Y. Honda, O. Kitao, H. Nakai, M. Klene, X. Li, J. E. Knox, H. P. Hratchian, J. B. Cross, V. Bakken, C. Adamo, J. Jaramillo, R. Gomperts, R. E. Stratmann, O. Yazyev, A. J. Austin, R. Cammi, C. Pomelli, J. W. Ochterski, P. Y. Ayala, K. Morokuma, G. A. Voth, P. Salvador, J. J. Dannenberg, V. G. Zakrzewski, S. Dapprich, A. D. Daniels, M. C. Strain, O. Farkas, D. K. Malick, A. D. Rabuck, K. Raghavachari, J. B. Foresman, J. V. Ortiz, Q. Cui, A. G. Baboul, S. Clifford, J. Cioslowski, B. B. Stefanov, G. Liu, A. Liashenko, P. Piskorz, I. Komaromi, R. L. Martin, D. J. Fox, T. Keith, M. A. Al-Laham, C. Y. Peng, A. Nanayakkara, M. Challacombe, P. M. W. Gill, B. Johnson, W. Chen, M. W. Wong, C. Gonzalez, and J. A. Pople, *Gaussian 03*, Revision C.02, Gaussian, Inc., Wallingford CT, 2004.

[51] Environmental Protection Agency Clean Air Act, http://www.epa.gov/ozone/snap/index.html, accessed 01/12/2016.

[52] S. Papasavva, S. Tai, K. H. Illinger, and J. E. Kenny, Infrared radiative forcing of CFC substitutes and their atmospheric reaction products, *J. Geophys. Res. Atmos.*, **102**, 13643-13650 (1997).

[53] P. J. Godin, K. Le Bris, and K. Strong, Conformational analysis and global warming potentials of 1,1,1,3,3,3-hexafluoro-2-propanol from absorption spectroscopy, *J. Quant. Spectrosc. Rad. Transfer*, doi:10.1016/j.jqsrt.2017.04.031 (2017).

[54] M. Fioroni, K. Burger, A. E. Mark, and D. Roccatano, Model of 1,1,1,3,3,3-Hexafluoro-propan-2-ol for Molecular Dynamics Simulations, *J. Phys. Chem. B*, **105**, 10967-10975 (2001).

[55] H. Schaal, T. Häber, and M. A. Suhm, Hydrogen Bonding in 2-Propanol. The Effect of Fluorination, *J. Phys. Chem. A*, **104**, 265-274 (2000).

[56] A. Berkessel, J. A. Adrio, D. Hüttenhain, and J. M. Neudörfl, Unveiling the "Booster Effect" of Fluorinated Alcohol Solvents: Aggregation-Induced Conformational Changes and Cooperatively Enhanced H-Bonding, *J. Am. Chem. Soc.*, **128**, 8421-8426 (2006).

[57] M. Quack, General Discussion, *Faraday Disscuss. Chem. Soc.*, **102**, 104-107 (1995).

[58] K. Le Bris, J. DeZeeuw, P. J. Godin, and K. Strong, *Cis*- and *trans*-perfluorodecalin: Infrared spectra, radiative efficiency and global warming potential, *J. Quant. Spectrosc. Rad. Transfer*, doi:10.1016/j.jqsrt.2017.01.011 (2017).

[59] K. Le Bris, J. DeZeeuw, P. J. Godin, and K. Strong, Infrared absorption cross-sections, radiative efficiency, and global warming potential of HFC-43-10mee, *J. Mol. Spec.*, doi:10.1016/j.jms.2017.06.004 (2017).

[60] S. Montzka, S. Reimann, A. Engel, K. Kruger, W. Sturges, D. Blake, M. Dorf, P. Fraser, L. Froidevaux, K. Jucks, et al., Scientific Assessment of Ozone Depletion: 2010, *Global Ozone Research and Monitoring Project-Report No. 51* (2011).

[61] P. Yan, White Cell System Report, Univ. of Toronto (2008).

[62] S. Hanst, Gemini Scientific Instruments, www.gascell.com (2015).

[63] M. Birk, D. Hausamann, G. Wagner, and J. W. Johns, Determination of line strengths by Fourier-transform spectroscopy, *Appl. Opt.*, **35**, 2971-2985, doi:10.1364/AO.35.002971 (1996).

[64] S. Robert, S. Chamberlain, A. Mahieux, I. Thomas, V. Wilquet, A. C. Vandaele, SOIR and NOMAD: Characterization of Planetary Atmospheres, *13th Biennial HITRAN Conference Proceedings* (2014).